7-6-2012

In Vivo characterization of Epileptic Tissue with Optical Spectroscopy

Nitin Yadav
Florida International University, nyada001@fiu.edu

Recommended Citation
Yadav, Nitin, "In Vivo characterization of Epileptic Tissue with Optical Spectroscopy" (2012). *FIU Electronic Theses and Dissertations.* Paper 728.
http://digitalcommons.fiu.edu/etd/728

FLORIDA INTERNATIONAL UNIVERSITY

Miami, Florida

IN VIVO CHARACTERIZATION OF EPILEPTIC TISSUE WITH OPTICAL SPECTROSCOPY

A dissertation submitted in partial fulfillment of the
requirements for the degree of
DOCTOR OF PHILOSOPHY
in
BIOMEDICAL ENGINEERING
by
Nitin Yadav

2012

To: Dean Amir Mirmiran
College of Engineering and Computing

This dissertation, written by Nitin Yadav, and entitled In vivo characterization of epileptic tissue with optical spectroscopy, having been approved in respect to style and intellectual content, is referred to you for judgment.

We have read this dissertation and recommend that it be approved.

Malek Adjouadi

Armando Barreto

Chenzhong Li

Richard Bone

Wei-Chiang Lin, Major Professor

Date of Defense: July 06, 2012

The dissertation of Nitin Yadav is approved.

Dean Amir Mirmiran
College of Engineering and Computing

Dean Lakshmi N. Reddi
University Graduate School

Florida International University, 2012

ACKNOWLEDGMENTS

I surely wouldn’t leave this opportunity of acknowledging everyone associated with my thesis. First and foremost, I am wholeheartedly indebted to Dr. Wei-Chiang Lin for his untiring assistance and who not only has been a constant source of inspiration for me but also for his concern and believing in me.

I will like to be thankful to Dr. Malek Adjouadi, Dr. Armando Barreto, Dr. Chenzhong Li and Dr. Richard Bone for serving on my dissertation committee. I would like to thank my previous and current lab members, Dr. Po-Ching Chen, Dr. Sanghoon Oh, Brad Fernald, Yinchen Song and Jared Leichner for their help in research. I will like to thank financial support by the Department of Biomedical Engineering and University Graduate School for Research Assistantship and Dissertation Year Fellowship respectively.

I will also like to thank my mother for her untiring support and my wife Anita for her constant and unconditional support and finally, I will like to dedicate this dissertation to the loving memories of my dad.

ABSTRACT OF THE DISSERTATION

IN VIVO CHARACTERIZATION OF EPILEPTIC TISSUE WITH OPTICAL SPECTROSCOPY

by

Nitin Yadav

Florida International University, 2012

Miami, Florida

Professor Wei-Chiang Lin, Major Professor

For children with intractable seizures, surgical removal of epileptic foci, if identifiable and feasible, can be an effective way to reduce or eliminate seizures. The success of this type of surgery strongly hinges upon the ability to identify and demarcate those epileptic foci. The ultimate goal of this research project is to develop an effective technology for detection of unique *in vivo* pathophysiological characteristics of epileptic cortex and, subsequently, to use this technology to guide epilepsy surgery intraoperatively. In this PhD dissertation the feasibility of using optical spectroscopy to identify unique *in vivo* pathophysiological characteristics of epileptic cortex was evaluated and proven using the data collected from children undergoing epilepsy surgery.

In this first *in vivo* human study, static diffuse reflectance and fluorescence spectra were measured from the epileptic cortex, defined by intraoperative ECoG, and its surrounding tissue from pediatric patients undergoing epilepsy surgery. When feasible, biopsy samples were taken from the investigated sites for the subsequent histological analysis. Using the histological data as the gold standard, spectral data was analyzed with statistical tools. The results of the analysis show that static diffuse reflectance

spectroscopy and its combination with static fluorescence spectroscopy can be used to effectively differentiate between epileptic cortex with histopathological abnormalities and normal cortex *in vivo* with a high degree of accuracy.

To maximize the efficiency of optical spectroscopy in detecting and localizing epileptic cortex intraoperatively, the static system was upgraded to investigate histopathological abnormalities deep within the epileptic cortex, as well as to detect unique temporal pathophysiological characteristics of epileptic cortex. Detection of deep abnormalities within the epileptic cortex prompted a redesign of the fiberoptic probe. A mechanical probe holder was also designed and constructed to maintain the probe contact pressure and contact point during the time dependent measurements. The dynamic diffuse reflectance spectroscopy system was used to characterize *in vivo* pediatric epileptic cortex. The results of the study show that some unique wavelength dependent temporal characteristics (e.g., multiple horizontal bands in the correlation coefficient map $\gamma(\lambda_{ref} = 800\text{ nm}, \lambda_{comp}, t)$) can be found in the time dependent recordings of diffuse reflectance spectra from epileptic cortex defined by ECoG.

TABLE OF CONTENTS

CHAPTER PAGE

LIST OF FIGURES

LIST OF TABLES

1. Background

1.1. Pediatric Epilepsy and Management

It is estimated by the Epilepsy Foundation that about 45,000 children under the age of 15 may develop epilepsy each year [1]. One common symptom of epilepsy is seizures, and repeated seizures are damaging to children because they can cause irreversible injuries to the brain as well as interfere with the normal brain development [2]. Epilepsy is not a name of a disease; it is rather a set of common symptoms that arise from different disorders of the brain. According to the International League Against Epilepsy (ILAE), epilepsy is defined as a chronic condition of the brain characterized by an enduring propensity to generate epileptic seizures, and by the neurobiological, cognitive, psychological, and social consequences of this condition. Thus, epilepsy can be interpreted as a disorder of brain which exists even when there is no seizure. Epilepsy is a discontinuous process, and it may spontaneously occur at anytime.

Seizures are the most common observable symptom of epilepsy. Seizures can be classified as:

1. Partial seizures: They are also called focal or localized seizures. They originate in more specific locations of the brain and mostly are developed from external injuries.
2. Generalized seizures: They typically occur in both sides of the brain and mostly are genetic.

Partial seizures are more common than generalized seizures. The cause of a seizure is determined in about 28% of partial epilepsy patients. In the rest, however, epilepsy is deemed idiopathic, which means that the cause is unknown [3]. A seizure's effect depends on the location in the brain. A person can seem to be confused after a seizure or can feel a spasm or, in the extreme case, may become unconscious.

While not completely proven, studies have identified various potential causes for epilepsy including chemical-malfunctioning of ion channels for sodium, potassium and calcium in neurons and astrocytes [4-7], abnormalities in neurotransmitters like GABA, serotonin and acetylcholine [5,8-10], or genetic or physical causes like fever, vaccinations, head injuries, viral infections and brain tumors [11, 12].

1.1.1. Pharmaceutical Therapies

Epilepsy is first treated with antiepileptic medications. Selection of medications is usually determined by the types of seizures and epilepsy syndromes, since certain medications are more effective against specific seizure types and syndromes than others. Achieving good control of seizures with drug treatment generally depends on choosing the right drug, minimizing the number of drugs prescribed, and educating the patient and family to encourage daily use as prescribed. Other factors that can affect the choice of drug include potential side effects, the dosing regimen -- whether it is simple or difficult to follow -- the age of the patient, childbearing potential, use of other medications, lifestyle, and, in some cases, cost. Whenever possible, using one drug is preferred. This drug may be prescribed in increasing doses until seizures are controlled or a side effect occurs. If the drug is not effective or if side effects are hard to live with, this drug will probably be gradually stopped while another one is slowly introduced.

In general, antiepileptic drugs eliminate seizures for about half of all patients with epilepsy; for another 20-30%, the intensity and number of seizures is reduced to the point where the person can live and work normally. The seizures in the remaining 20% of people with epilepsy do not respond well to current medications, and their condition is termed “refractory to treatment.” For those patients, other treatment options, such as surgery, vagus nerve stimulation, or the ketogenic diet, may be explored.

1.1.2. Dietary Therapy

The diet is based on the observation that starvation, which burns fat for energy and produces ketones, has an antiepileptic effect. The goal of the diet is to make the body get its energy from fat and become ketotic. It is primarily done by administering a ketogenic diet to the epilepsy patients. The ketogenic diet is a high-fat, adequate protein, very low carbohydrate diet that is both calorie and fluid restricted and initiated in hospital because of risks of severe metabolic abnormalities during and after the initial fasting period to create and maintain ketosis. Generally, medications are not discontinued along with ketogenic diet. How ketogenic diet reduces seizures remains somewhat unclear and is probably multifactorial, but many studies have clearly demonstrated it effective in >50% reduction of seizures in 38% children [13].

There are also adverse effects associated with ketogenic diet, including sluggishness during the initial treatment. Staying on ketogenic diet for a long period of time could lead to kidney stones, high cholesterol, dehydration, constipation, slowed growth or weight gain, and bone fractures [14]. It should also be noted that certain particular epilepsy syndromes may respond better to ketogenic diet than others [15].

1.1.3. Vagus nerve stimulation

Vagus nerve stimulation (VNS) is a relatively new procedure in pediatric epilepsy management. It involves implanting an electronic device in the upper chest that delivers electrical stimulation to the vagus nerve in the neck to control seizure frequency, severity, and duration. VNS is used in adjunct treatment with antiepileptic drugs. It has been approved by the US Food and Drug Administration for use in treating partial seizures in adults and adolescents over age 12 after medical therapy has failed to control the seizures.

The VNS therapy system consists of the implantable pulse generator and bipolar VNS therapy lead, a programming wand with software, a tunneling tool, and a handheld magnet. Once implanted, the device delivers a regular pattern of stimulation. Patients can turn the device on if they feel a seizure coming on by using a special magnet, which in some cases may prevent the seizures. Medical studies of the device suggest that some patients will gain some benefit from the VNS device although complete seizure control is rare. Approximately one-third of patients receiving VNS therapy experience at least a 50% reduction in seizure frequency with no adverse cognitive or systemic effects [16]. Moreover, clinical findings indicate that the effectiveness of VNS therapy continues to improve over time, independent of changes in AEDs or stimulation parameters [16]. Tolerance does not appear to be a factor with VNS therapy, even after extended periods of time. Most people continue to take antiepileptic drugs while receiving the VNS therapy. The most commonly reported side effects are hoarseness, coughing and breathlessness [17].

1.2. Epilepsy Surgery

Epilepsy is regarded as refractive if it has been continuously active for 3 years in spite of adequate trials of therapy with three or more main-line antiepileptic drugs, and if seizures are frequent (more than one per month). The best way to combat refractive epilepsy is to remove the epileptic focus and its surroundings.

1.2.1. One Stage Surgery

In one stage surgery, electrocorticography (ECoG) is heavily relied on in the operating room just before the resection. Here interictal activities of epileptic cortex is captured by ECoG and then used to define the area of resection. The epileptic cortex defined by ECoG may have consistent focality in interictal spiking, rhythmic features, trains of focal fast beta activity, or focal attenuation of background [18-21]. One stage epilepsy surgery has advantages over the two-stage one (see below) in terms of cost and less risk of infection. Awake intraoperative ECoG can also be used to map eloquent cortex [22-24].

1.2.2. Two Stage Surgery

In a two-stage epilepsy surgery, the initial operation aims to place subdural electrodes for seizure monitoring [16-19]. Ictal zone is then demarcated by seizures occurrence. Sometimes functional mapping may be performed during the seizure monitoring stage. The information collected during the monitoring stage will be used to define the zone of resection for the second operation taking place about one week after the first operation [25]. In planning the resection, a clear relationship between eloquent cortex and epileptic area needs to be defined [26, 27]. Typically, a margin of at least 0.5-1 cm is required to spare function. Language cortex can be mapped in children as young as 2.5 years of age [26, 27]. Two-stage epilepsy surgery is used when the epileptic zone is discrete, no lesions are present in the imaging study, or the planned resection is adjacent to eloquent cortex [28]. The main disadvantages of a two-stage surgery are higher costs and risks of infection [29, 30].

1.3. Technologies Used in the Planning of Epilepsy Surgery

Current technologies used in diagnosis of epilepsy and demarcations of epileptic tissue are:

1.3.1. Electroencephalogram (EEG)

EEG is used to detect abnormal electrical activities in the brain associated with epileptic seizures. In an EEG study, multiple electrodes are placed on scalp, and the brain wave patterns are recorded and studied. Through the study, the abnormal patterns that indicate seizures can be identified. Ideally, EEG should be performed within 24 hours of a seizure. The duration of EEG recordings vary from an hour to a few days in case of intractable epilepsy.

An EEG study performed with simultaneous video recording is called a video EEG study [31, 32]. It provides the doctors insights into the seizure type and the possible brain area where the epileptic activities originate. Simultaneous video recordings can also provide information to the determination of paroxysmal event frequency and aid in the diagnosis of nonepileptic seizures, as well as help with seizure and epilepsy classification [33].

1.3.2. Computerized Tomography (CT) Scans

CT scans take x ray images of the brain from many different angles to determine its crosssectional configuration with the aid of a computerized reconstruction algorithm. In the planning procedure of an epilepsy surgery, CT scans may be performed to detect the structural abnormalities in the brain associated with epileptic seizures [34]. An iodine based dye may be injected into a patient before taking a CT scan in order to enhance image contrast in certain anatomical structures such as blood vessels. The amount of radiation used in a CT scanning procedure is quite low, so it is safe to perform CT scans repeatedly.

1.3.3. Magnetic Resonance Imaging (MRI)

MRI is an imaging modality that uses a magnetic field to change the spin of the atomic particles in the body and hence perform three-dimensional imaging. The MRI images can be used to identify abnormal areas in the brain, small brain tumors, blood vessel abnormalities, and changes in white matter. In the planning stage of an epilepsy surgery, MRI is used to detect the structural abnormalities in the brain associated with epileptic seizures [35, 36]. MRI is recommended for children after their first seizure and seizures that are associated with any unexplained significant mental or motor problems.

1.3.4. Other Advanced Imaging Techniques

Another popular imaging technology used in the planning stage of an epilepsy surgery is Positron Emission Tomography (PET). It measures regional metabolic activities in the brain, based on which brain functions and/or disorders are detected. During a seizure, the area responsible for the seizure will show up as an area of increased glucose use in the PET images [37]. Between the seizures, the epileptic focus shows a characteristic pattern of reduced need for glucose in the PET images [38]. PET has proven to be an important diagnostic tool in selecting patients with partial epilepsy, in particular with foci in the temporal lobe, for resective surgery [39]. Single-photon emission computer tomography (SPECT) is another useful technology to plan an epilepsy surgery. It identifies patterns of change in cerebral blood flow during seizures in children [40]. It could be useful in clarifying the poorly understood interplay of the interictal and ictal states in human focal epilepsy [41]. SPECT and PET are generally helpful if MRI is not much useful for deciding on surgery [42].

Diffusion Tensor Imaging or DTI is used for tracing subtle changes in directionality and magnitude of water diffusion due to diseases. It enables visualization and characterization of white matter fascicli in two and three dimensions. It is used to noninvasively assess the molecular and biochemical environment of cerebral tissue [40, 43]. Diffusion weighted images can provide information on the molecular movements in the microstructure. DTI can aid in characterizing and measuring the diffusive transport of water molecules by means of an effective diffusion tensor, D. The symmetric tensor measurements contains useful information about the tissue microstructure and architecture [44].

1.3.5. ECoG

Electrocorticography (ECoG) was first used in 1940 to exactly find the location and extent of the epileptic brain tissue prior to epileptic surgery. It is now considered as a golden standard for demarcation of epileptic cortex. ECoG is an invasive procedure which involves placing the electrodes to monitor electrical activity from cerebral cortex on an exposed brain surface. It can identify the areas which are epileptic in nature. The recording equipment used for ECoG is same as that for scalp EEG; a two-dimensional electrode array provides simultaneous recording from multiple locations. The recording electrodes must make a light contact with the exposed cortex to generate signals with high signal to noise ratio. Signal filters are set at 0.3–70 Hz and the sensitivity at 50–75 μV/mm in an ECoG study, otherwise clipping of spikes (often 1–3 mV) and excessive amplification of other activity could impair data analysis and interpretation. ECoG provides more valuable information than EEG because it has a high spatial and frequency resolution and is immune from the eye and muscle artifacts.

Preoperative studies like EEG, CT Scans, and MRI are essential to identify epileptic activities within the brain that are accessible to resection. Lateralization and at least a rough localization of the epileptic focus is absolutely necessary to allow correct placement of recording electrodes. Therefore, the intraoperative ECoG does not replace presurgical evaluation. Furthermore, it is impossible to use ECoG to distinguish primary epileptiform discharges from secondary propagated discharges arising at a distant epileptic site [45, 46].

1.4. Optical Technologies for Intraoperative Surgical Guidance

1.4.1. Biomedical Optics

Light traveling in a biological tissue is governed by two tissue optical properties, namely absorption coefficient $\mu_a(\lambda)$ [1/cm] and scattering coefficient $\mu_s(\lambda)$ [1/cm]. In the visible wavelength region (i.e., 400 to 700 nm), the absorption in a biological tissue is caused primarily by hemoglobin. Therefore, the absorption coefficient of a biological tissue in the visible wavelength region may be expressed as

$$\mu_a(\lambda) = 2.303 \times [Hb] \times (SATO_2 \times \epsilon_{HbO2} + (1 - SATO_2) \times \epsilon_{Hb}) \text{ [1/cm]} \qquad (1.1)$$

where [Hb] is the hemoglobin concentration in mole, $SatO_2$ is hemoglobin oxygenation, ϵ_{HbO2} is the molar extinction coefficient of oxy-hemoglobin [1/cmM], and ϵ_{Hb} is the molar extinction coefficient of hemoglobin [1/cmM]. Because the molar extinction coefficient of hemoglobin varies significantly in accordance with its oxygenation (see Figure 1.1), it is possible to obtain the two critical hemodynamic parameters (i.e., [Hb] and $SatO_2$) through the study of $\mu_a(\lambda)$ of the biological tissue.

Light scattering inside a biological tissue is a result of spatial variation in tissue refractive index. Various intra- and extra-cellular components contribute to the light scattering, and their contributions, in general, are size and density dependent [48, 49]. $\mu_s(\lambda)$ is defined in the way that the probability of a scattering event over a short distance s will be $\mu_s(\lambda) \times s$. $\mu_s(\lambda)$ may be correlated with the size/density of scatterers in a biological tissue using Mie theory. That is

$$\mu_s'(\lambda) = \mu_s(\lambda) \times (1 - g) = a \times m^{-b} \text{ [1/cm]}, \qquad (1.2)$$

where g is unisotropic factor and $m = \lambda \times 10^3$. It has been shown that the morphological and structural characteristics of a biological tissue may be assessed through its $\mu_s(\lambda)$ [50].

1.4.2. Optical Spectroscopy

Optical spectroscopy is a technology developed to study the intrinsic properties of a material through its interaction with light. Over the past two decades, researchers in the field of biomedicine have been utilizing optical spectroscopy to perform minimally-invasive, nondestructive detections of tissue diseases and injuries in various organs like cervix, brain, skin, pancreas, colon, breast and esophagus [51-61]. The types of optical spectroscopy frequently used to perform optical diagnosis include diffuse reflectance spectroscopy and fluorescence spectroscopy. Diffuse reflectance spectroscopy is used primarily to detect tissue hemodynamics as well as the compositional and structural information [62]. It has the advantage of being affordable and portable and producing diagnostic results in real time.

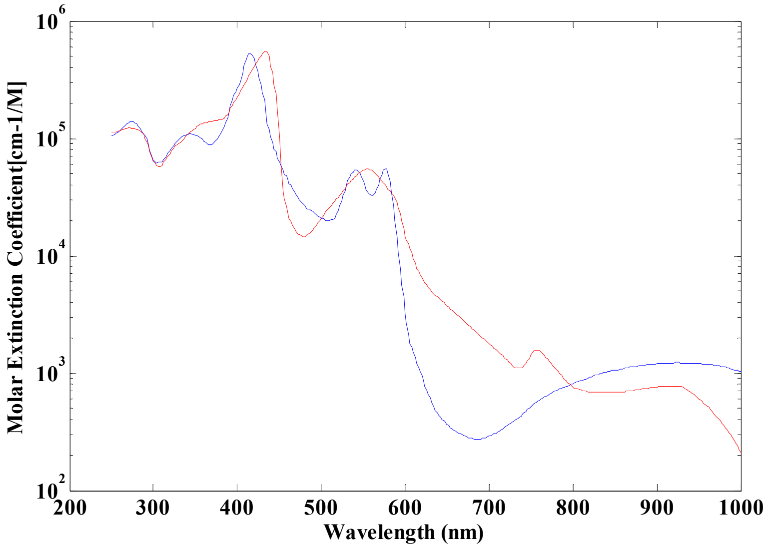

Figure 1.1: *Molar Extinction Coefficients of oxy-hemoglobin (blue) and deoxy hemoglobin (red) as a function of wavelength [47].*

Fluorescence spectroscopy is used to detect and quantify molecules that can absorb a high energy photon and yield a low energy fluorescence photon (i.e., fluorophores). In biological tissues, the endogenous molecules possessing such a capability include: NADH, FAD^{2+}, Tryptophan and its derivatives (e.g. serotonin, and dopamine) and collagen [63]. In the research field of optical diagnosis, fluorescence spectroscopy is often used to gauge the redox state of NADH and hence the metabolic activities of *in vivo* organs [64]. Accurate interpretations of fluorescence spectra from *in vivo* tissue can be very challenging because the propagation of both excitation and emission (fluorescence) photons is strongly influenced by the optical properties of tissue [65].

1.4.3. Intraoperative Demarcation of Neoplastic and Epileptic Lesions Using Optical Spectroscopy

The feasibility of using optical spectroscopy to intraoperatively guide cancer surgery has been evaluated in various cancer types [54, 66, 67]. Several studies have shown that combined fluorescence and diffuse reflectance spectroscopy can accurately detect brain tumor *in vivo* and hence may be used to guide brain tumor resection [51, 68]. A recent study also demonstrates the potential of using diffuse reflectance spectroscopy alone to detect pediatric brain tumors *in vivo* [69]. The concept of using optical spectroscopy to aid epilepsy surgery is very new, and it has only been explored in a few studies to date [70, 71]. However, a diffuse reflectance imaging modality (i.e., intrinsic optical imaging) has been used to study the hemodynamic characteristics of human epileptic cortex *in vivo* [72, 73]. It should be noted that the intrinsic optical imaging modality only acquires the diffusely reflected light from the cortex at a few selected wavelengths. The accuracy of using optical modalities, including fluorescence and diffuse reflectance spectroscopy, to demarcate epileptic cortex intraoperatively, nevertheless, has not been proved yet.

2. Statement of Purpose

2.1. Hypothesis

As discussed in the background section, epilepsy leads to drastic changes in the hemodynamic, metabolic, and compositional characteristics of the brain tissue, which are tapped by existing techniques like MRI for seizure localization. Because of the unique advantages provided by optical spectroscopy, it can potentially play a significant role in the future management of pediatric patients who have intractable epilepsy and are good candidates for epilepsy surgery. More specifically, optical spectroscopy may be used to detect unique pathophysiological characteristics of epileptic cortex in a nondestructive manner *in vivo*, which, in turn, can assist surgeons to accurately differentiate an epileptic cortex from a nonepileptic brain during an epilepsy surgery. The primary objective of this dissertation is to prove this concept, and its central hypothesis is: *fluorescence and diffuse reflectance spectroscopy can detect interictal pathophysiological characteristics associated with pediatric epileptic cortex in an intraoperative fashion*. To validate this hypothesis, the following specific aims were proposed and carried out.

2.2. Specific Aims

Aim 1: To identify static fluorescence and diffuse reflectance spectral features that differentiate between normal and epileptic pediatric cortex defined by pathology. The study outcomes related to this specific aim are presented in chapter 3 of this dissertation.

Aim 2: Develop a portable fiberoptic spectroscopic system with capability to capture dynamic diffuse reflectance spectra from *in vivo* brain in an intraoperative environment. The study outcomes of this specific aim are reported in chapters 4 and 5 of this dissertation.

Aim 3: Identify dynamic diffuse reflectance spectral features associated with pediatric epileptic cortex defined by ECoG and pathology. The study outcomes related to this specific aim are presented in chapter 6 of this dissertation.

3. In Vivo Characterization of Epileptic Cortex using Static Fluorescence and Diffuse Reflectance Spectroscopy

3.1. Introduction

According to the Epilepsy Foundation, of the 200,000 new cases of epilepsy diagnosed each year in the United States, 45,000 are children under the age of 15 [1]. Epilepsy is considered a severe neurological disorder in children, because its primary symptom, seizure, can severely damage normal brain development. When the pharmaceutical and/or dietary therapies fail to achieve seizure freedom, epilepsy is defined as refractory [78, 79]. For pediatric patients with refractive epilepsy, surgical intervention, when applicable, becomes necessary. Since the success of epilepsy surgery is determined by the amount of seizure-inducing cortex (i.e., epileptic cortex) removed, there arises a need to develop some systematic methodology that accurately detect and demarcates the epileptic cortex pre- and intra-operatively.

Non-invasive diagnostic technologies commonly used in the pre-surgical planning of epilepsy surgery include electroencephalography (EEG), Video EEG, and several noninvasive imaging modalities like computed tomography (CT), single-photon emission computed tomography (SPECT), magnetic resonance imaging (MRI), positron emission tomography (PET), and diffusion tensor imaging (DTI) [80-84]. Advancements in noninvasive imaging modalities over the past two decades have greatly improved their ability to identify epileptic cortex or lesions and, hence, surgical outcomes [80, 83, 84]. However, the above mentioned diagnostic technologies, when used individually, cannot provide definitive information upon which surgery can be based; they, at best, provide approximate locations of seizure origins due to their limited sensitivity and spatial resolution [80, 83, 45]. In addition, these technologies may be difficult to use on pediatric patients who may not be able to remain motionless for extended periods of time [85]. Finally, spatial coordinates of the epileptic cortex defined in these studies may lose their value because of brain shift/deformation during the craniotomy procedure [86-89].

When EEG/imaging studies are inconclusive, electrocorticography (ECoG) may be used to perform invasive mapping of the ictal onset zone [45, 90]. In addition, ECoG is used in the operating room to directly detect interictal epileptiform discharges from the abnormal brain region, which are used to define the resection margins for the surgeon. However, ECoG may detect interictal discharges in normal brain as well, as a result of electrical spreading, and epileptic focus localization using interictal discharges is subject to a certain amount of uncertainty in anesthetized brain [90]. Histological evaluation of epileptic cortex has uncovered many unique pathological features such as balloon cells and cortical dislamination [91]. This information usually is acquired through post-operational histopathological analysis of the resected brain specimens and is not immediately available in the operating room. While histopathological features of the lesion may not correlate with surgical outcomes [83, 19], it is not yet clear if their presence can be used as an objective indicator with which to demarcate the area of epileptic brain. The technological shortcomings and limitations described above frequently lead to incomplete removal of epileptic lesions, which adversely affects surgical outcomes. This is especially true for cases of extra-temporal epilepsy, which is common in children [80, 84, 85, 19]. For these reasons, new technologies for intraoperative identification and demarcation of the epileptic brain area are needed to enhance the prognosis of epilepsy surgery for patients with intractable non-lesional extra-temporal epilepsy. These new technologies, ideally, should be developed in accordance with the intrinsic characteristics of epileptic brain during the interictal period.

Because the intrinsic compositional and structural characteristics of tissue strongly affect its absorption and scattering properties, it is feasible to use the interaction between light and biological tissue to estimate these qualities and, hence, detect whatever alterations that result from disease development [51, 56, 74, 92-99]. Such an optic-based diagnostic technology often is termed *optical diagnosis*; its advantages include its low cost, portability, and real-time application. Among the existing optical diagnostic methodologies, many are based on fluorescence and diffuse reflectance spectroscopy. This is because several intrinsic biological chromophores (e.g., hemoglobin) and fluorophores (NADH) can be used to assess critical intrinsic physiological characteristics of biological tissue, including its hemodynamics and metabolism [98, 99 64, 100, 101]. The feasibility of using optical spectroscopy to intra-operatively guide cancer surgery has been evaluated for various cancer types. Several studies have shown that combined fluorescence and/or diffuse reflectance spectroscopy can accurately detect brain tumors *in vivo* and, hence, may be used to guide brain tumor resection [51, 69]. However, applying optical spectroscopy to the detection of epileptic cortex has only been explored in a limited fashion to date [70-72, 101, 102].

In this chapter, combined fluorescence and diffuse reflectance spectroscopy was used to detect unique pathophysiological and morphological characteristics of epileptic cortex in an *in vivo* human study. Static diffuse reflectance and fluorescence spectra were acquired from *in vivo* epileptic and normal cortex of pediatric patients undergoing epilepsy surgery. Spectral data were analyzed using various statistical tools, and unique spectral features associated with epileptic brain tissue defined by histology and ECoG were identified. The physiological underlying mechanisms responsible for these spectral alterations were extrapolated.

3.2. Materials and Methods

3.2.1. Instrumentation

For this study, a portable spectroscopy system was used for acquiring fluorescence and diffuse reflectance spectra from the brain. The system consisted of two light sources: a pulsed nitrogen laser (VSL-337; Spectra Physics) for fluorescence spectroscopy and a portable halogen lamp (LS-1; Ocean Optics) for diffuse reflectance spectroscopy. Since data collection was performed in a sterile field, a sterilizable fiberoptic probe was used in conjunction with the spectroscopy system. The probe consisted of seven 300-micron core optical fibers, out of which two were used to conduct excitation light and the remaining fibers for reflected light collection. Based on the arrangement of the optical fibers in the probe, its volume of investigation was estimated at roughly 1 mm^3. The collection fibers of the optical probe were connected to a spectrometer (USB 2000-FL Spectrometer; Ocean Optics) with a spectral range of approximately 300-900 nm. The spectrometer was connected to a computer via a universal serial interface. A computer program was developed using LabView from National Instruments to control the entire spectral acquisition procedure.

3.2.2. Study Procedure

Static fluorescence and diffuse reflectance spectra were acquired from normal and epileptic brain areas, as defined via pre-operative imaging and ECoG studies, in pediatric patients undergoing epilepsy surgery. From each single patient, five or more measurement sites were selected at the exposed brain surface by the surgeon. These sites usually were equally distributed within and outside the resection zone. Prior to the spectral acquisition procedure, the investigated site was cleansed using saline to remove any residual blood on its surface. The optical probe was placed in direct contact with the cortical surface without deforming the brain surface, and three spectra (i.e., baseline, fluorescence, and diffuse reflectance spectra) were acquired sequentially. Spectral acquisition was repeated three times, with the total time required to complete the above-mentioned procedure less than 15 seconds. The locations of the optically-investigated sites and their spatial correlation with the ECoG electrode grids were documented using a digital camera. Biopsies were taken from the investigated sites within the zone of resection and stored in a 10% buffered formalin solution for subsequent histological analysis.

3.2.3. Histological Evaluation

All specimens collected in this study were processed in a histology lab. They were *embedded in paraffin* wax and then sectioned. From each specimen, three to four 4-micron thick sections were cut and stained using the conventional hematoxylin and eosin staining method. The prepared section was evaluated by a neuropathologist at the University of California, Los Angeles (Dr. Rupal Mehta). These tissue sections were assessed for architectural laminar disorder, cytomegaly, dysmorphism, and balloon cell change. These findings were graded from 0-3 (0-none, 1-mild, 2-moderate and 3-severe). The presence of binucleated cells and calcification was also noted separately. These morphological characteristics then were used to categorize spectral data as either normal or histologically abnormal.

3.2.4. Data Processing

All spectral data acquired from the *in vivo* study were preprocessed to remove any artifacts induced by instrumentation. Mainly, baseline subtraction and calibration applications were performed to all acquired fluorescence spectra $F(\lambda)$ and diffuse reflectance spectra $Rd(\lambda)$ [68]. Furthermore, to speed up the data analysis procedure, spectral range and resolution were further reduced. Specifically, diffuse reflectance data between 400 nm and 850 nm and fluorescence data between 380 nm and 750 nm were preserved; spectral resolution was reduced to 5 nm. In addition to the individual spectral types, a combined spectrum was created for the data analysis process, specifically the ratio of the fluorescence and diffuse reflectance spectra (i.e., $F(\lambda)/Rd(\lambda)$). The wavelength range of the combined spectra was 400 to 750 nm, and their resolution was 5 nm. Several normalization techniques were applied to the preprocessed spectra, including local maximum normalization, area under the curve normalization, global mean normalization, and arbitrary reference normalization (See Figure 3.1). For local maximum normalization, each spectrum is normalized to its maximum value. That is $S_{\max}(\lambda) = S(\lambda)/MAX(S(\lambda))$, where $S(\lambda)$ represents either $F(\lambda)$, $Rd(\lambda)$, or $F(\lambda)/Rd(\lambda)$, and MAX is the maximum operation. For area-under-the-curve normalization, the new spectrum $S_{AREA}(\lambda)$ is calculated by $S_{AREA}(\lambda) = S(\lambda)/\int_{\lambda} S(\lambda)$. For global mean normalization, each spectrum is normalized to the mean of the total spectral data set. That is $S_{MEAN}(\lambda) = S(\lambda)/[\sum_n S(\lambda)/n]$, where n represents the number of spectra in a single spectral dataset. Finally, arbitrary reference normalization produces a new spectrum using $S_{POINT}(\lambda) = S(\lambda)/S(\lambda_{ref})$, where λ_{ref} is an arbitrary reference wavelength.

3.2.5. Data Analysis and Classification Algorithm Development

The main objective of this analysis was to determine if *in vivo* fluorescence and diffuse reflectance spectroscopy can detect histopathological and/or pathophysiological characteristics that are unique to epileptic brain tissue. To achieve this goal, the spectral data collected were classified using the results of histological analysis: the normal brain data containing spectral data measured from brain tissue outside the zone of resection, and the epileptic brain data containing spectral data from epileptic brain tissue confirmed by both histology and ECoG. To identify spectral regions and unique spectral features distinguishing epileptic brain tissue from normal cortex, mean comparisons of the processed spectra from the two types of brain tissue (normal vs. epileptic) was performed for all wavelengths. Depending on the distribution and variance characteristics of the data, either parametric (i.e., Student's t-test) or non-parametric tests (Wilcoxon Rank Sum test) were employed for mean comparisons. Next, tissue classification algorithms were developed based on linear discrimination analysis (LDA), for the purpose of determining the accuracy of using optical spectroscopy to differentiate between normal and epileptic brain tissue. LDA inputs were the spectral data from normal and epileptic brain.

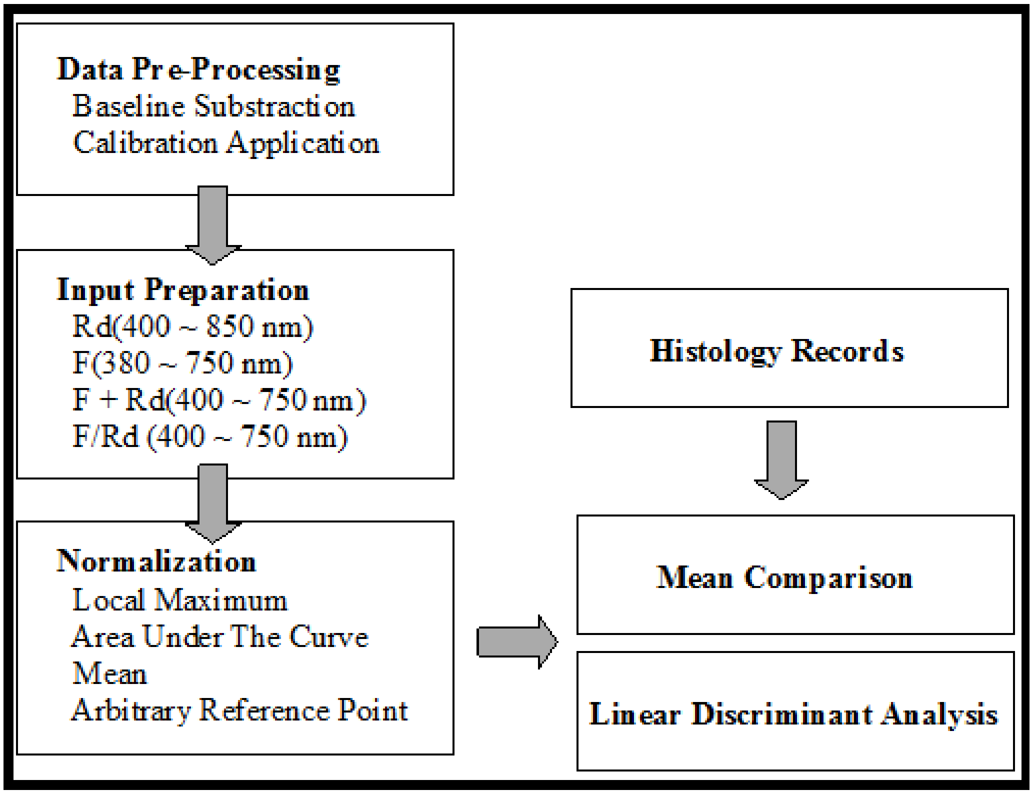

Figure 3.1: *The flow chart of the data processing procedure employed in the study.*

Spectral data at all wavelengths were used in this process to create a model of discrimination, and standardized canonical coefficients used to assess the importance of spectral data region in determining tissue type. It was important to ensure that the discrimination model was statistically significant in terms of distinguishing normal brain from epileptic brain;

therefore, only models associated with chi-square p values less than 0.05 were considered. Furthermore, only models with sensitivity and specificity greater than 75% were considered 'successful' and reported here. Finally, tissue type classification was validated using the cross validation method (i.e., building the model based on all data but one variable, and predicting the one excluded variable).

3.3. Results

In this study, a total of 16 patients were enrolled, for whom demographic information is summarized in Table 3.1. The total number of useful investigated sites from these patients was 84, among which 28 sites were located outside the resection zone defined by ECoG (i.e., normal brain) and 56 sites within the zone of resection (ZOR). The 56 sites within the ZOR were further divide into two subcategories in accordance with the results of histological evaluation: 30 sites exhibited histological features associated with epilepsy (epileptic brain), while the remaining 26 sites did not. The distribution of sites is shown in Table 3.2.

Spectral data analysis revealed that only those spectral differences identified within four spectral types (i.e., original $Rd(\lambda)$, $Rd_{MEAN}(\lambda)$, $Rd_{POINT}(\lambda)$, and $F/Rd_{MEAN}(\lambda)$) could produce discrimination algorithms with sensitivity and specificity greater than 75%. Analytical results for each spectral type follow.

3.3.1. Original $Rd(\lambda)$

Comparing the original $Rd(\lambda)$ from normal and epileptic brain revealed significantly different mean $Rd(\lambda)$ intensity between 400 and 600 nm ($p < 0.05$, see Figure 3.2). Inputting the Rd signals from this spectral band, the best classification result based on LDA was 82.1% sensitivity, 76.7% specificity, and 79.3% total accuracy.

3.3.2. $Rd_{MEAN}(\lambda)$

Similar to original $Rd(\lambda)$, $Rd_{MEAN}(\lambda)$ between 400 and 600 nm also was statistically different between normal and epileptic brain ($p < 0.05$, see Figure 3.3). Entering the signals from this spectral band, the best classification result based on LDA was 75.0% sensitivity, 83.3% specificity, and 79.3% overall accuracy, which is comparable to using the original $Rd(\lambda)$.

Patient Number	Patient Age/Gender
1	3/M
2	4/F
3	4/M
4	6/M
5	2/F
6	14/F
7	8/F
8	21/F
9	2/M
10	20/F
11	17/F
12	5/M
13	3/F
14	16/F
15	10/M
16	3/M

Table 3.1: *Demographic information of the patients studied.*

ECoG	Pathology	Site #
-	NA	28
+	-	26
+	+	30

Table 3.2: *Distribution of the investigated sites.*

3.3.3. $Rd(\lambda)/Rd(\lambda_{ref})$

Analyzing $Rd(\lambda)/Rd(\lambda_{ref})$, as shown in Figures 3.4 and 3.5, revealed several spectral features that could effectively differentiate normal from epileptic brain. Most of these spectral features were evident between λ_{ref} = 400 and λ_{ref} = 600 nm. Entering these identified spectral features, classification results based on LDA were ~75% sensitivity and ~80% specificity (Table 3.2). Discrimination was optimized when λ_{ref} was 505 nm, where the overall accuracy of the discrimination algorithm was 86.2%.

3.3.4. $[F(\lambda)/Rd(\lambda)]/[F(\lambda_{ref})/Rd(\lambda_{ref})]$

Analysis of $[F(\lambda)/Rd(\lambda)]/[F(\lambda_{ref})/Rd(\lambda_{ref})]$, as shown in Figures 3.6 and 3.7, also revealed several spectral features from the combined spectrum that could effectively distinguish normal from epileptic cortex. Again, the majority of these spectral features were located between λ_{ref} = 400 and $\lambda_{ref} = 600$ nm. Entering the identified spectral features, classification results based on LDA yielded sensitivity above 75% and specificity above 80% (Table 3.3). Discrimination was optimized when λ_{ref} was 485 nm, where the overall accuracy of the discrimination algorithm was 96.6%.

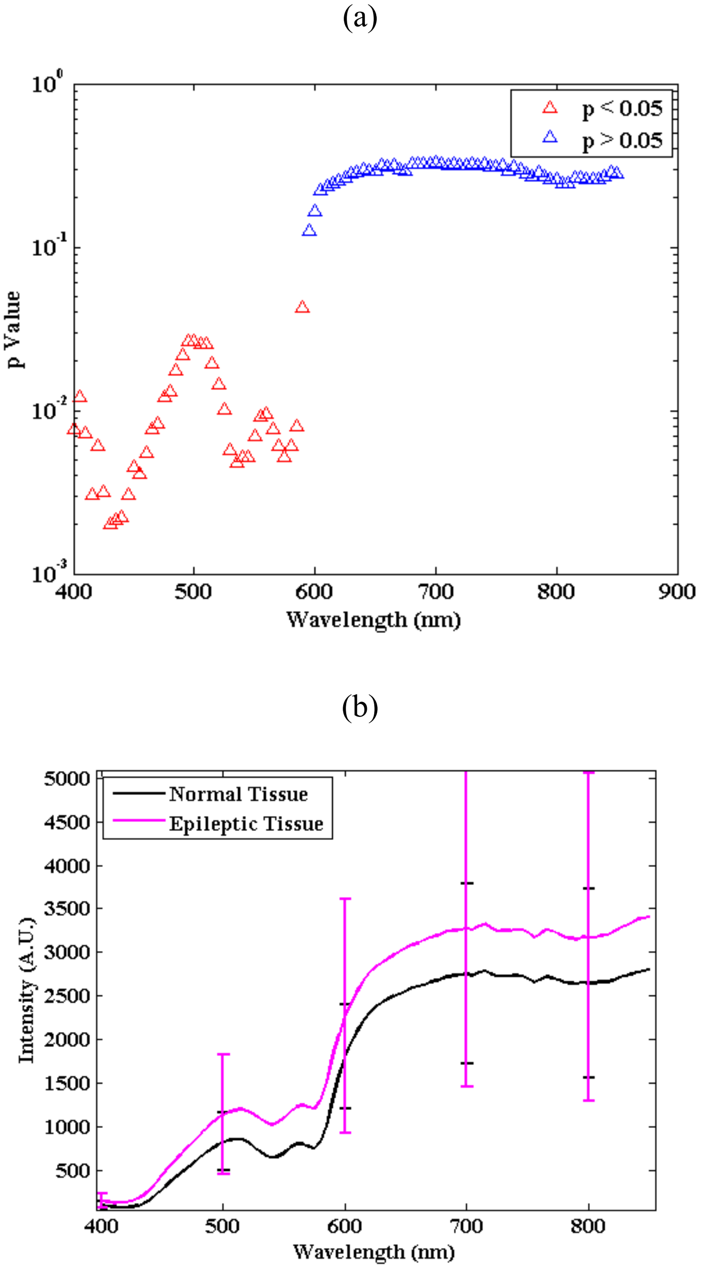

(c)
Sensitivity: 82.1%
Specificity: 76.7%
Total Correct Classification: 79.3%

Figure 3.2*: (a) The black solid line represents the mean original Rd(λ) from the normal brain group, and the solid pink line the epileptic brain group. The error bars represent one standard deviation of the mean. p value is below 0.05 between 400 and 600 nm. (b) Statistical mean-comparison of original Rd(λ) between normal and epileptic brain. (c) The optimal performance of the classification based on LDA, using original Rd(λ) as the inputs, was sensitivity = 82.1%, specificity = 76.7%, and total correct classification = 79.3%.*

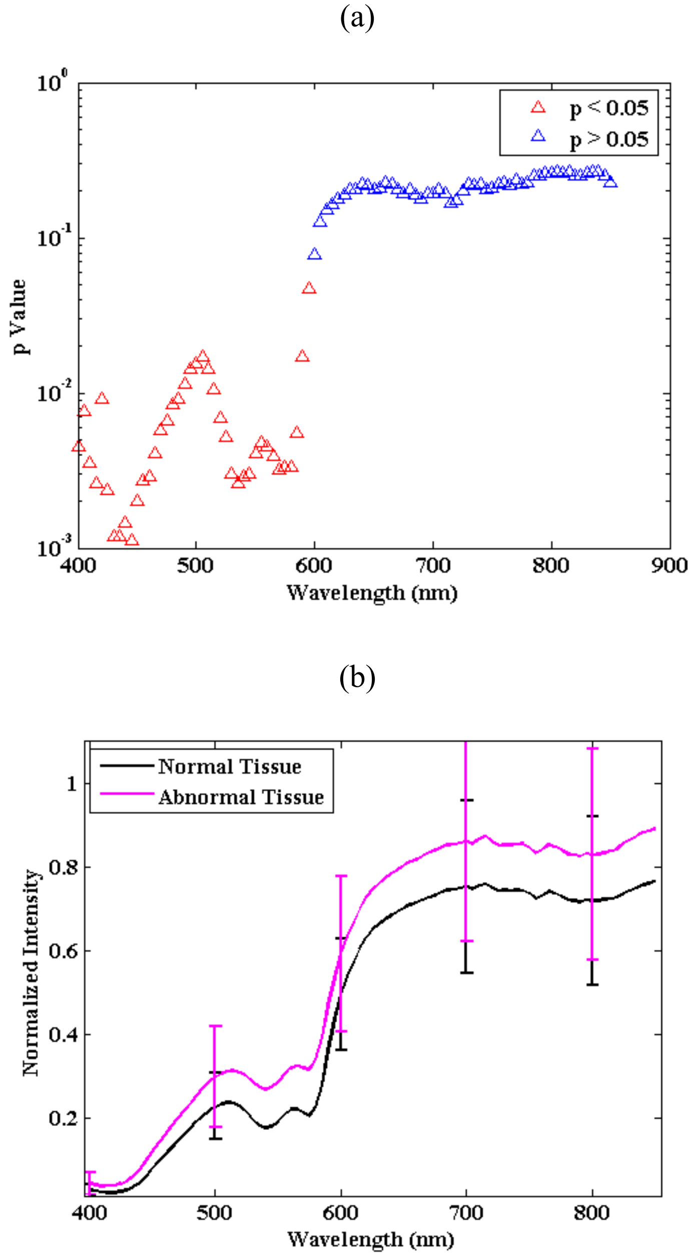

(c)
Sensitivity: 75%
Specificity: 83.3%
Total Correct
Classification: 79.3%

Figure 3.3*: (a) The black solid line represents the mean $Rd_{MEAN}(\lambda)$ from the normal brain group, and the solid pink line the epileptic brain group. The error bars represent one standard deviation of the mean. p value is below 0.05 between 400 and 600 nm. (b) Statistical mean-comparison of $Rd_{MEAN}(\lambda)$ between normal and epileptic brain. (c) The optimal performance of the classification based on LDA, using $Rd_{MEAN}(\lambda)$ as the inputs was sensitivity = 75%, specificity = 83.3%, and total correct classification = 79.3%.*

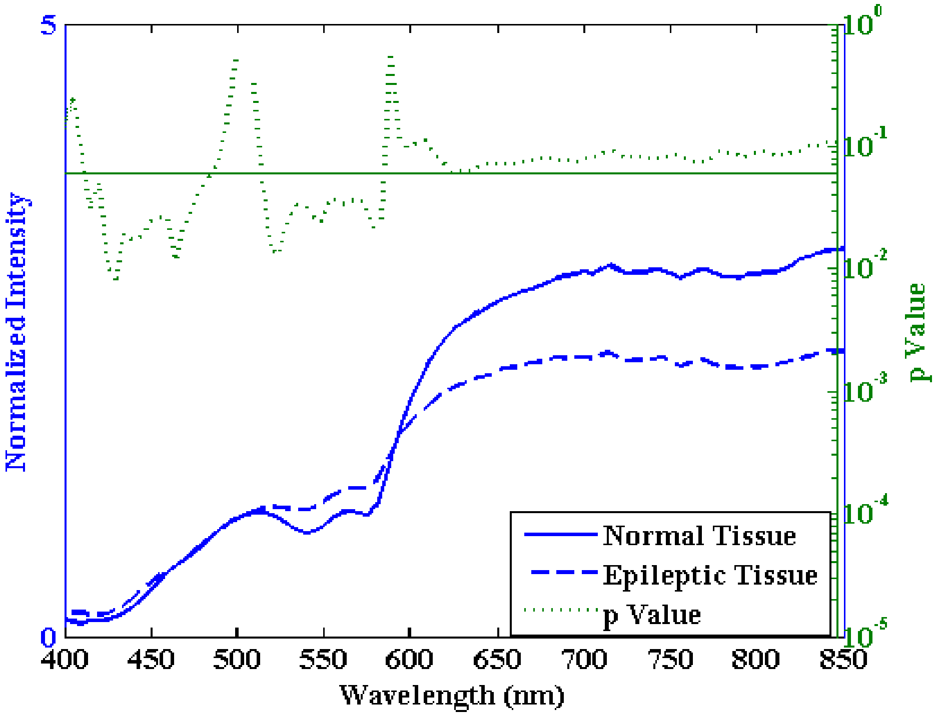

Figure 3.4: *(a) Surface plot of the p_values from the mean-comparison of Rd(λ)/Rd(λ$_{ref}$) between normal and epileptic brain. (b) Representative test results with reference wavelength λ$_{ref}$ = 505 nm. The blue solid line represents the mean Rd(λ)/Rd(λ$_{ref}$) of the normal brain group, and the blue dash line the epileptic brain group. Statistically significant differences ($p < 0.05$) are found between 425 nm and 460 nm and 535 nm and 575 nm in this case.*

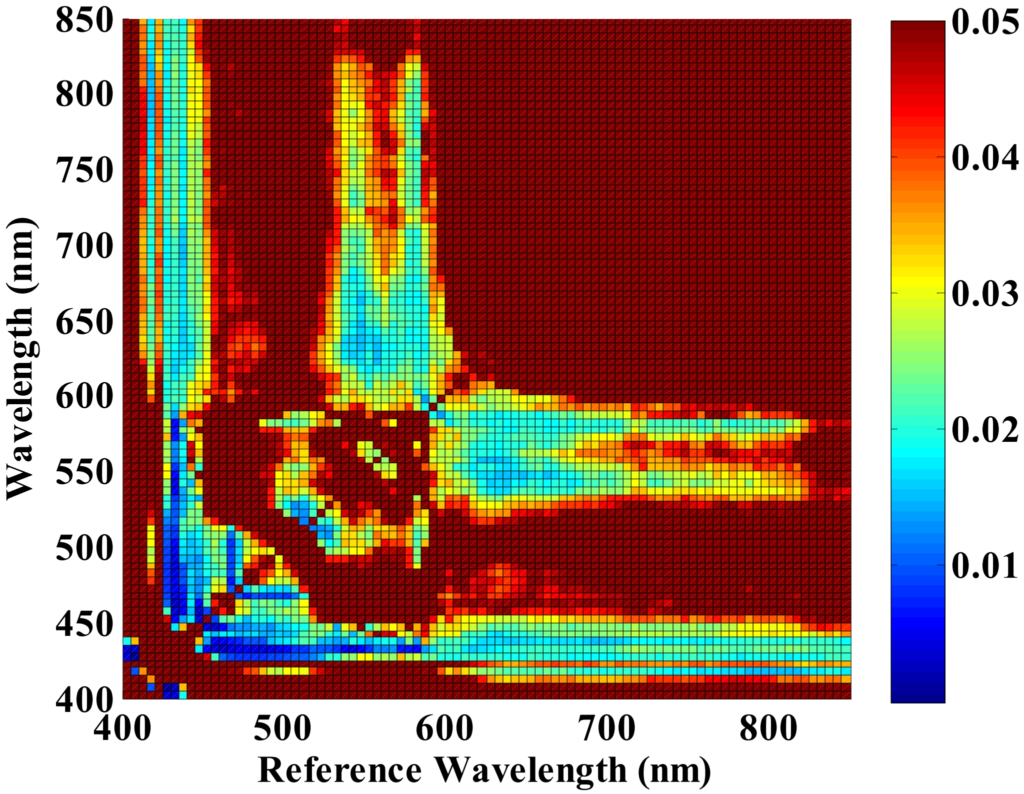

Figure 3.5*: Surface plot of the p-values from the mean comparison of Rd(λ)/Rd(*λ_{ref}*) from the normal and the epileptic cortex group. Each data column in this surface plot represents the line-plot shown in Figure 3.4.*

λ_{ref} (nm)	Sensitivity (%)	Specificity (%)	Total Correct Classification (%)
445	75	86.7	81
455	75	80	77.6
460	75	83.3	79.3
500	78.6	90	84.5
505	82.2	90	86.2
535	78.6	86.7	82.8
550	78.6	86.7	82.8
605	78.6	86.7	82.8

Table 3.3*: Classification results of the discrimination algorithms based on LDA using Rd(λ)/Rd(*λ_{ref}*) as the inputs.*

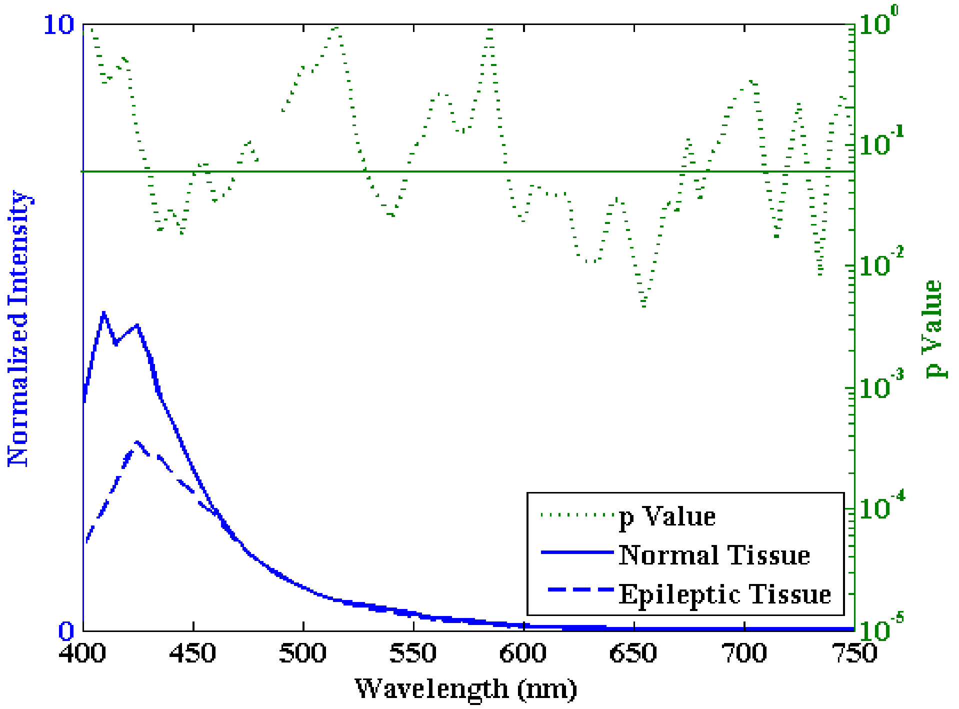

Figure 3.6: *Representative statistical mean comparison of [F(λ)/Rd(λ)]/[F(λ$_{ref}$)/Rd(λ$_{ref}$)] from the normal and epileptic groups. Here λ$_{ref}$ is 485 nm. The blue solid line represents the mean spectrum of the normal group, and the blue dash line the epileptic group. The statistically significant differences (p < 0.05) are found between 430 nm - 450 nm as well as 625 nm - 660 nm.*

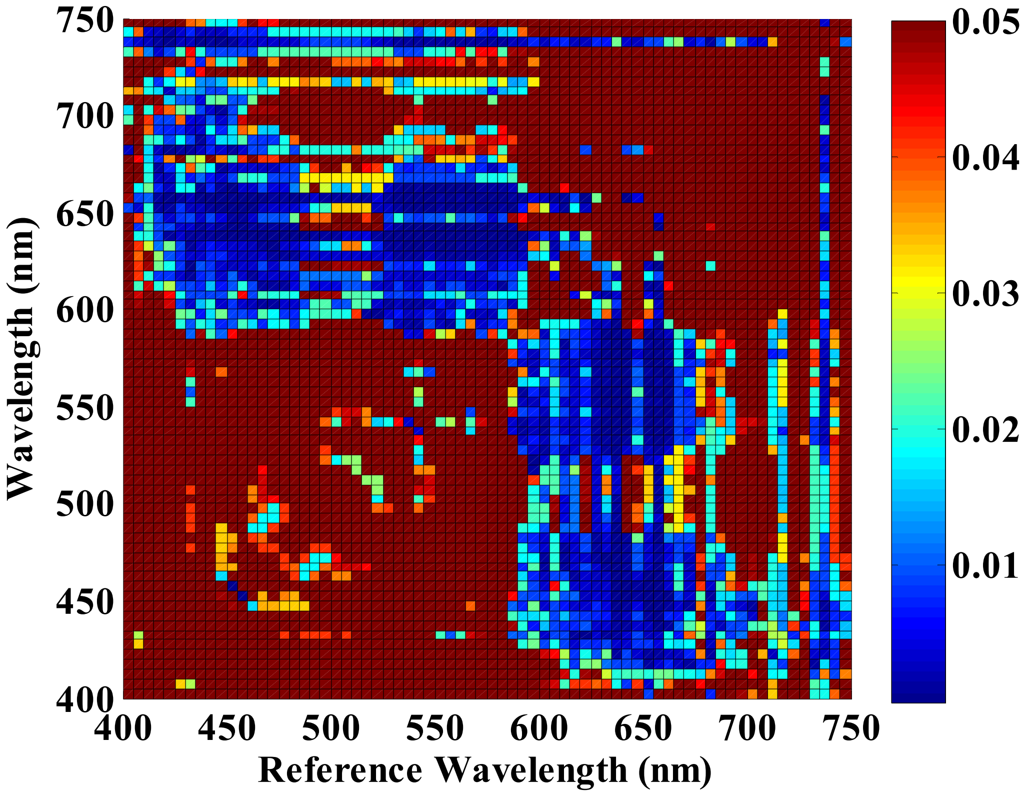

Figure 3.7: *Surface plot of p values from the mean comparison of [F(λ)/Rd(λ)]/[F(*λ_{ref}*)/Rd(*λ_{ref}*)] from normal cortex and epileptic cortex. Each data column in this surface plot represents the line-plot shown in Figure 3.6.*

λ_{ref} (nm)	Sensitivity (%)	Specificity (%)	Total Correct Classification (%)
400	75.0	83.3	79.3
420	75.0	86.7	81.0
455	89.3	86.7	87.9
485	92.9	100.0	96.6
500	85.7	90.0	87.9
505	89.3	90.0	89.7
510	89.3	90.0	89.7
520	92.9	90.0	91.4

Table 3.4: *Classification results of the discrimination algorithms based on LDA, using [F(λ)/Rd(λ)]/[F(*λ_{ref}*)/Rd(*λ_{ref}*)] as the inputs.*

3.4. Discussion

The *in vivo* study results reported in this chapter demonstrate that *in vivo* static diffuse reflectance spectroscopy, as well as its combination with static fluorescence spectroscopy, can be used to effectively differentiate epileptic brain (as defined by ECoG and histology) from normal brain with a high degree of accuracy. The most effective discrimination algorithm is derived using the spectral features from $[F(\lambda)/Rd(\lambda)]/[F(485nm/Rd(485nm)]$, where discrimination accuracy reaches 96.6%. This supports the concept of developing a new intraoperative guidance system based on optical spectroscopy, to detect histopathological abnormalities associated with epileptic brain in the operating room and, thereby, provide additional information to aid in the demarcation of epileptic foci.

Using parametric and non-parametric statistical comparison methods, original $Rd(\lambda)$, $Rd_{MEAN}(\lambda)$, and $Rd(\lambda)/Rd(\lambda_{ref})$ between 400 and 600 nm were found to be significantly different in epileptic versus normal brain. Since diffuse reflectance spectra in this region are heavily influenced by hemoglobin absorption, this finding implies that certain static hemodynamic characteristics of epileptic cortex, in particular hemoglobin concentration and hemoglobin oxygenation, are very different from that of normal cortex. Previous studies have shown that hypometabolism and hypoperfusion are frequently observed in the area of an epileptic focus and its immediate surroundings in the brain of patients with partial seizures [104-109]. In addition, Stefanovic *et al* pointed out that normal interictal neurovascular coupling is progressively compromised by sustained seizure attacks [109]; Schwartz suggested that epileptic cortex generally receives inadequate cerebral blood flow [75]. However, alterations in resting state hemodynamics may not exist in all types of refractive epilepsy. It has been shown that average resting metabolism and blood flow are largely unremarkable in patients with idiopathic generalized epilepsy [110-112]. Because of significant differences in the discharge characteristics of ictal versus interictal states, it has been suggested that the cerebral blood flow and cerebral metabolic rate of oxygen changes induced by interictal discharges may be far less noticeable than their ictal counterpart [104, 111, 113]. This implies that the changes in diffuse reflectance signals reported here are not necessarily associated with the presence of interictal discharges. The results of this study further suggest that histological abnormalities may be linked to changes in regional resting state hemodynamics. It is possible that histological abnormalities like cortical dysplasia modify the characteristics of astrocytic Ca^{2+} oscillations, which, in turn, alter astrocytic function regulating cerebral blood vessel diameters and, hence, regional hemodynamics [114-118]. More studies, however, will have to be conducted to verify such conjectures.

When illuminated by an excitation light at 337 nm, the intrinsic fluorescence signal collected from brain tissue between 450 nm and 500 nm emission is believed to originate primarily from NAD(P)H. This assumption is based upon two factors: (1) NAD(P)H has a relatively high quantum yield relative to other biological fluorophores at the same excitation wavelength; and (2) the concentration of NAD(P)H is very high in the brain, due to brain's high metabolism. Several studies have shown that the metabolic activities of any *in vivo* biological tissue, including brain, may be monitored through NAD(P)H fluorescence [74, 99]. Since epileptic cortex is hypo-metabolic [104-109], it has been hypothesized that fluorescence spectroscopy may be used to detect this characteristic of epileptic brain. However, the study results reported here do not support this hypothesis; the intrinsic fluorescence spectra (337 nm excitation) from epileptic brain were not significantly different from those of normal brain. One possible explanation for this inefficiency is that fluorescence signals measured from *in vivo* brain are heavily modulated by its absorption (i.e., hemoglobin concentration and hemoglobin oxygenation) as well as scattering properties. In order to truly verify the usefulness of NADH fluorescence at detecting epileptic cortex, intrinsic fluorescence quantity must be retrieved using complex spectral processing techniques [76].

The results of the current study are promising, but only preliminary in nature. Several obstacles must be overcome before the clinical value of optical spectroscopy, namely fluorescence and diffuse reflectance spectroscopy, is clarified for demarcating epileptic foci and, hence, aiding epilepsy surgery. The most important challenge is the lack of a gold standard for defining epileptic brain. While optical spectroscopy can indirectly detect histological abnormalities of epileptic brain, it is not yet proven that these histological features provide better demarcation than ECoG. Furthermore, this study also revealed considerable discrepancies between the results of ECoG and those of histological study. On many occasions, the brain area classified as abnormal by ECoG was interpreted as histologically normal by our neuropathologist. This may be attributed to the fact that the optical probe we used in this study has a limited depth of investigation (less than 1 mm). Therefore, optical investigation was performed only on the superficial layer of the cortical surface; histopathological abnormalities present in the deeper layers of the cortex could be missed by either optical spectroscopy or biopsy. Another possible explanation is that conventional histological methods cannot detect molecular alterations underlying the abnormal electrical activities of epileptic cortex. Also, it is possible that the origin of interictal spikes may not be the same as that defined by ECoG due to electrical spreading. Finally, it will be challenging to establish a universal normal baseline for the diffuse reflectance and fluorescence spectra of normal pediatric cortex, because the brain undergoes development and increases in size and weight significantly throughout childhood. To address the challenges mentioned above, a new probe should be engineered to investigate various layers of cortex for abnormalities associated with epilepsy. Moreover, a dynamic spectroscopy system that is capable of continuously recording fluorescence and diffuse reflectance spectra from the *in vivo* brain at a high rate (> 15 Hz) should be developed and used. Such a system will allow us to gain insights into the dynamic natures of epileptic cortex during the interictal state, which could yield a better spectral discriminant. These new developments will be reported in the following chapters.

3.5. Conclusions

The feasibility of using diffuse reflectance and fluorescence spectroscopy to aid epilepsy surgery in children was investigated. Static diffuse reflectance and fluorescence data were collected from abnormal cortex, as defined by pathology and ECoG. Tissue discrimination algorithms with high sensitivity and specificity were produced using various spectral features. The success of this study warrants a future large-scale study to verify the potential role of optical spectroscopy in pediatric epilepsy surgery.

4. Design and Develop a Portable Dynamic Spectroscopy System for *In Vivo* Epileptic Brain Study

4.1. Introduction

Fiberoptic spectroscopy systems are commonly used in optical diagnostic studies [119, 120]. However, they often are used to capture the static natures of *in vivo* tissue. Since the brain is a dynamic organ and the epileptic brain processes several unique temporal physiological characteristics, it is important to improve the optical spectroscopy system described in chapter 3 to capture these unique features and hence, maximize the efficiency of optical spectroscopy in detecting epileptic cortex intraoperatively. In this chapter, details about the design and development of a new dynamic spectroscopic system for *in vivo* study of the epileptic brain are presented.

4.2. Optical Probe Design and Development

One major task of the instrumentation update was to optimize the design of the optical probe. The arrangement of the optical fibers within an optical probe influences the collection efficiency of reflected light (i.e., signal to noise ratio) and, more importantly, the volume and the depth of investigation. As mentioned before, histopathological studies of epileptic cortex have shown that structural abnormalities associated with epilepsy may exist in the deeper layers (2 to 4 mm) of the cortex. Therefore, it is critically important to understand the design parameters of the fiber optical probe, mainly the distance between the source fiber and the collection fiber (i.e., source-detector separation), influence the depth of investigation and signal to noise ratio. To gain this insight, a computer simulation model for photon migration, Monte Carlo simulation, was developed and used.

4.2.1. Materials & Methods

Monte Carlo simulation for photon migration is a popular tool to study light propagation and distribution in biological tissues (i.e., scattering-absorbing media). The mathematical algorithms of the MC simulation can be found elsewhere [121]. To speed up the development process, the new simulation code was developed using a MC simulation model previously developed by Dr. Wei-Chiang Lin (WCLMC). WCLMC was derived from the source codes written by Dr. Andy Dunn, University of Texas at Austin, as well as those written by Dr. Steve Jacques and Lihong Wang at MD Anderson Cancer Center. WCLMC simulates the steady state photon distribution within and outside a multilayered tissue slab (i.e., diffuse reflectance, fluence rate, and diffuse transmittance), illuminated by a light source at an arbitrary incident angle.

In order to adapt WCLMC for the needs of the probe design study, the following modifications were performed.

(I) The location and the diameter of the detection fiber can be specified by the user. When a photon package is launched by the source fiber (centered at the origin), its trajectory within the simulated tissue will be recorded and preserved, if its exit location is within the area of detection determined by the detection fiber.

(II) The collection of reemitted photons is exit angle dependent. This modification takes the finite numerical aperture of an optical fiber into consideration. Also, it provides the capability of designing an optical probe with tilted optical fibers, which can control the depth of investigation in an optical diagnosis application [122, 123].

(III) The weight deposition (i.e., energy absorption) by a photon package, while it is traveling within the simulated tissue, is registered (see Figure 4.1). In this simulation model, weighted photon (i.e., photon package) is used and its initial weight is 1.

(IV) The weight deposition is registered 3-dimensionally. The tissue slab was divided into an array of voxels whose dimensions (i.e., dx, dy, and dz) are defined by the user. This setup facilitated layer wise summation of photon weight deposition, which, in turn, provides knowledge about the contributions of individual layers to the detected signal (see Figure 4.2).

The modified WCLMC was called ProbeMC, and its flow chart is depicted in Figure 4.3. Since brain cortex has a layer wise structure [124, 125], ProbeMC was designed to handle such a characteristic. Specifically, the simulated tissue in ProbeMC may have an arbitrary number of layers; each layer is homogenous and has a unique thickness and optical properties. The width of the simulated tissue is infinite in general. Optical properties of each layer used in the simulations for the probe design study were those from human gray and white matter (see Table 4.1) [126-129]. An example input file of ProbeMC is provided in Table 4.2. Finally the number of photons used in each simulation was sufficiently large (e.g., 10 million) to smooth out the statistical noises associated with the MC simulation. ProbeMC was computationally intensive; therefore, several multi-core personal computers were used to complete the simulation work needed to complete the probe design study. The simulation results were displayed in 3D using Voxler software from Scientific Software Group. The accuracy of ProbeMC was confirmed by comparing its results with those produced by WCLMC using identical input parameters.

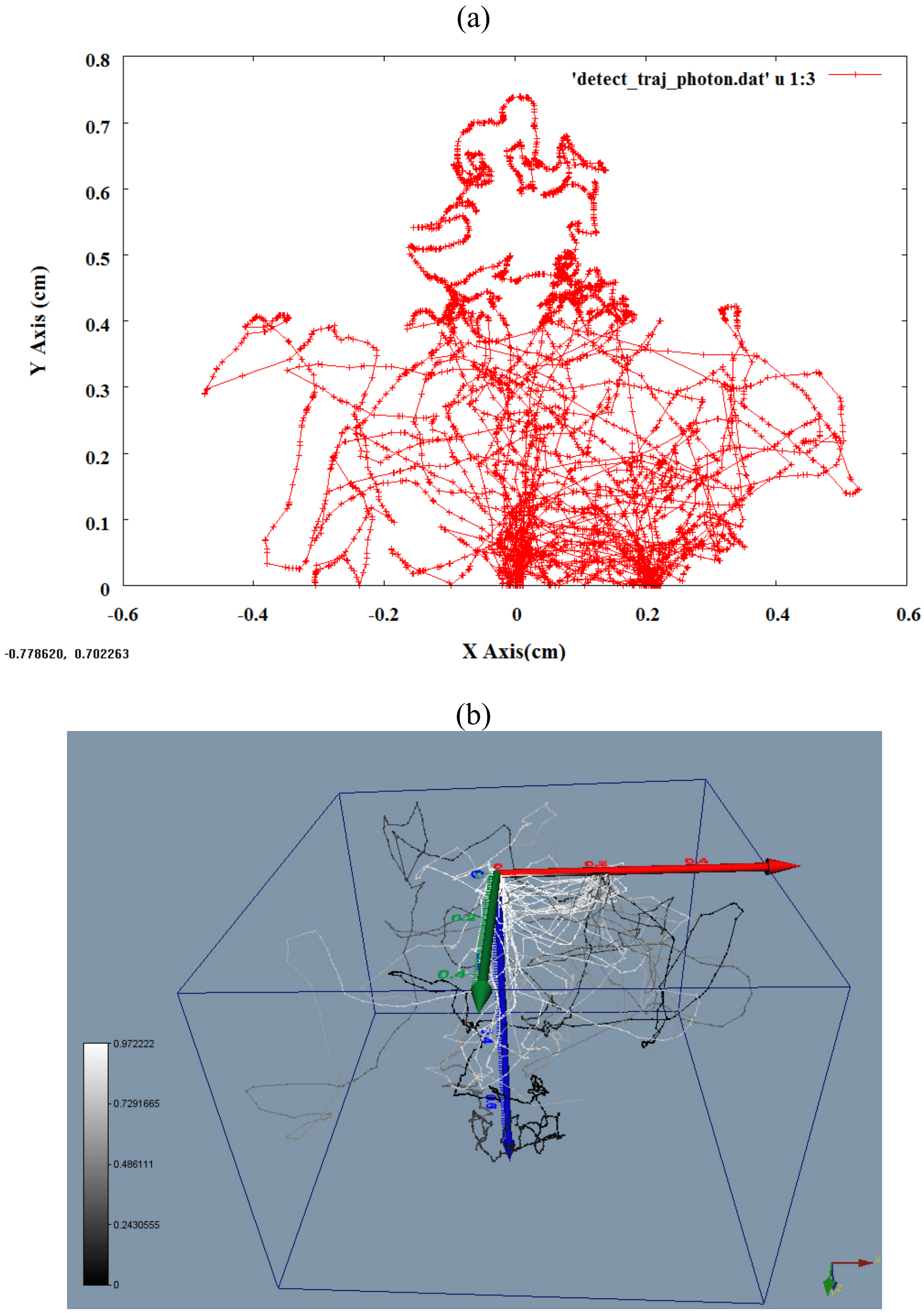

Figure 4.1: *(a) A 2-D illustration of multiple photon trajectories within the simulated tissue. The symbols represent the locations of photon energy deposition. (b) Weightwise display of a photon package migrating from the source fiber to the detector fiber. Here white color denotes the weight of the photon package is 1; black is 0.*

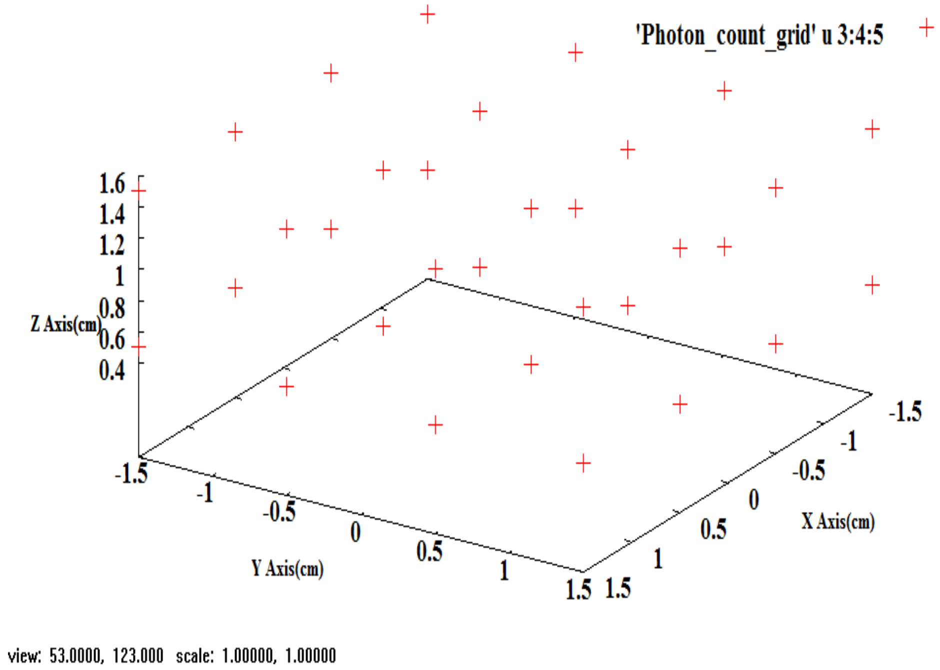

Figure 4.2: *Illustration of an example grid cell (voxel) centres used to record photon weight deposition in ProbeMC.*

850 nm	**Thickness (cm)**	**mua (cm^{-1})**	**mus (cm^{-1})**	**g**
Layer 1	0.4	0.47	67	0.9
Layer 2	1.6	1	342	0.88
450 nm	**Thickness (cm)**	**mua (cm^{-1})**	**mus (cm^{-1})**	**g**
Layer 1	0.4	0.7	117	0.88
Layer 2	1.6	1.4	420	0.78

Table 4.1: *Optical properties of the simulated brain tissue at 450 nm and 850 nm. Here Layer 1 represents the cortex and Layer 2 the white matter.*

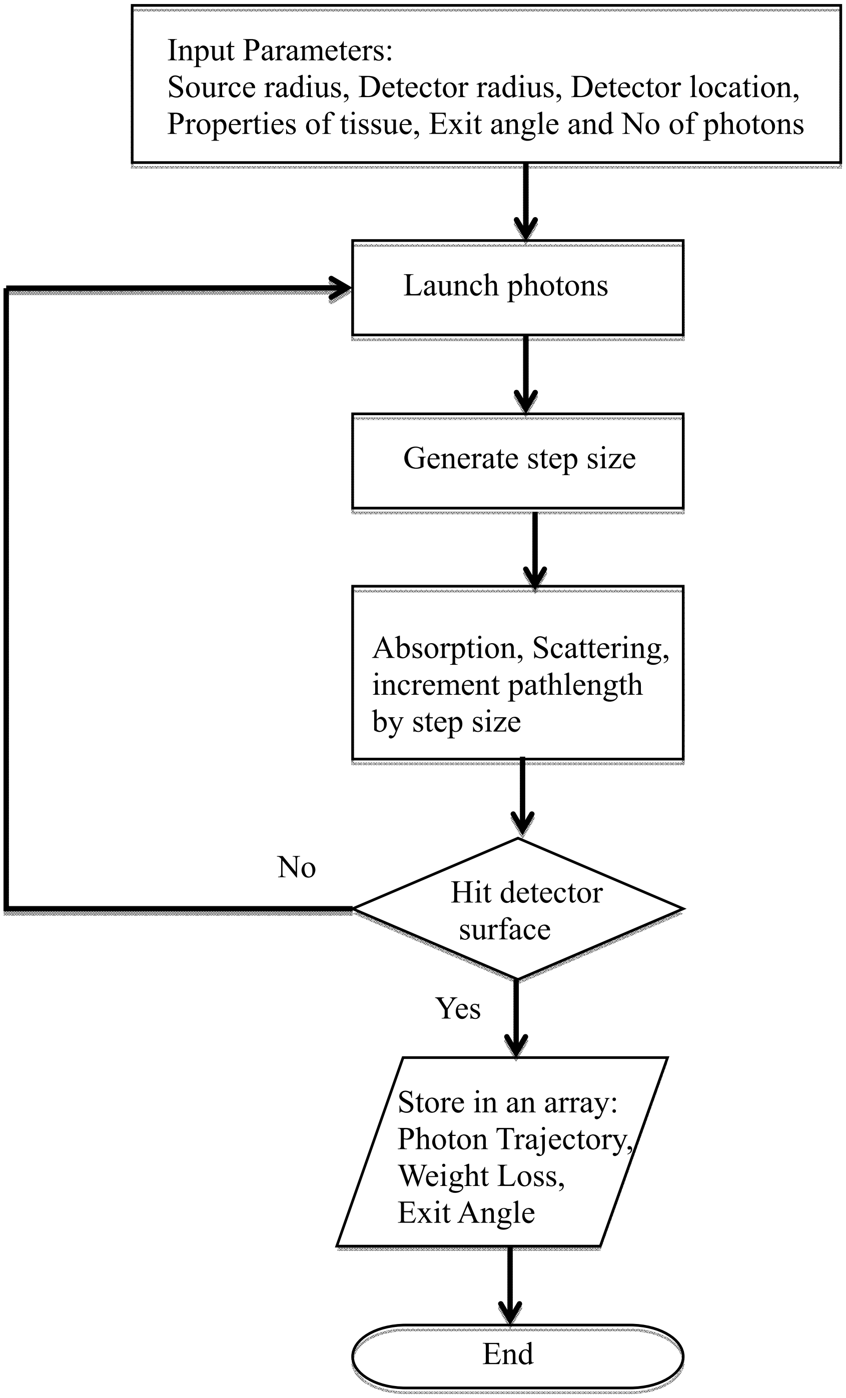

Figure 4.3*: Flowchart of ProbeMC developed in house for the probe design study.*

Number of Layer	2	
Refractive index of the incident medium	1	
	Layer 1	**Layer 2**
mus	See Table 4.1	
mua		
g		
Thickness	0.4	1.6
Refractive index	1.4	1.4
Refractive index of the back medium	1	
Number of photons	10,000000	
Number of x grids	1	
dx	4	
Number of y grids	1	
dy	4	
Number of z grids	20	
dz	0.1	
beam radius (cm)	0.015	
X coordinate of detector	0.090	
Y coordinate of detector	0	
Detector Radius	0.015	

Table 4.2*: Representative input file for ProbeMC.*

4.2.2. Results

4.2.2.1. Signal Strength vs. Source Detector Separation

Figure 4.4 shows the simulated relationship between the diffuse reflectance intensity and the source detector separation (S-D), using the brain model depicted in Table 4.1. Clearly diffuse reflectance decreases quickly when S-D increases; the rate of decrease with S-D < 1 mm is much greater than that with S-D > 1 mm. Comparing the relationships at 450 nm and 850 nm, it was noticed that the rate of decrease in diffuse reflectance intensity is slower at 850 nm than that at 450 nm. This indicates that the S/N ratio of the diffuse reflectance signal at 450 nm will suffer more significantly than that at 850 nm when S-D increases.

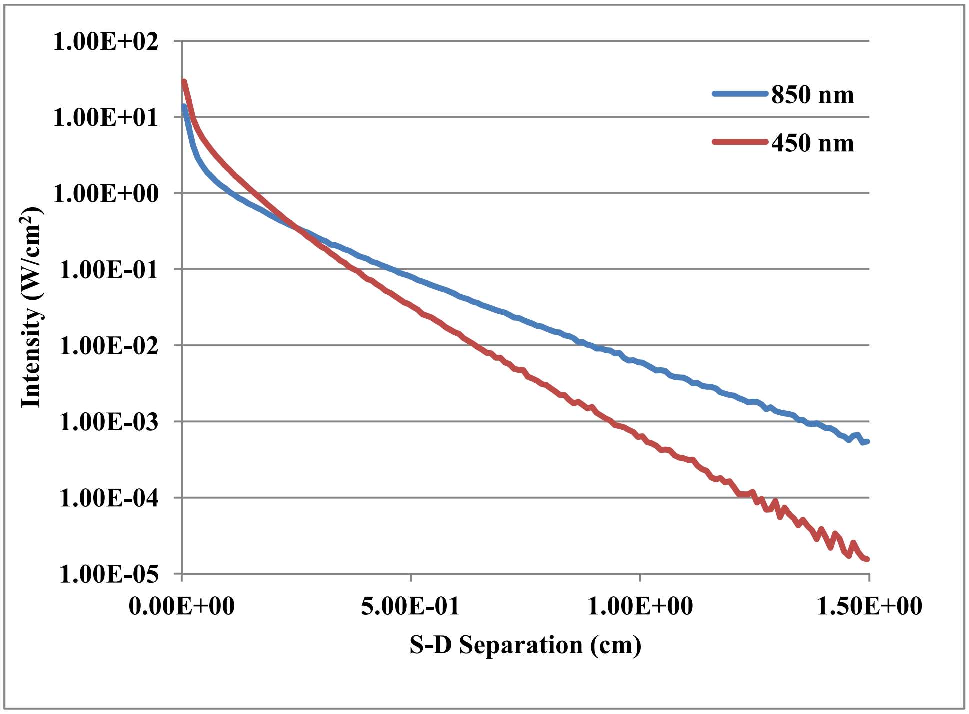

Figure 4.4: *Diffuse reflectance intensity (W/cm^2) at 450 nm and 850 nm as a function of source-detector separation (S-D).*

4.2.2.2. Weight Deposition vs. Source Detector Separation

Figure 4.5 depicts the relationship between the layerwise photon weight deposition and source detector distance at 450 nm. Here, the majority of the photon weight deposition takes place within the first layer (i.e., 0 to 0.1 cm). In other words, the first 0.1 cm of the simulated tissue sample dictates the magnitude of the diffuse reflectance signal at 450 nm. As the source detector separation increases, the percentage weight deposition in layer 2 increases steadily (i.e., making a stronger influence to the signal detected). However, the effect of SD on the weight deposition in layers 3 and beyond is minimal. Therefore, diffuse reflectance signals at 450 nm will not be sensitive to the optical characteristics of the cortex beyond 2 mm below the surface.

Figure 4.6 depicts the relationship between the layerwise photon weight deposition and S-D at 850 nm. The majority of the photon weight deposition takes place within the first five layers (i.e., 0 to 0.5 cm) of the simulated tissue. In other words, the first 5 mm of the tissue sample strongly dictates the magnitude of the diffuse reflectance signal at 850 nm. As S-D increases, the relative weight deposition in layers 2 to 5 increases steadily (i.e., making a stronger influence to the signal detected).

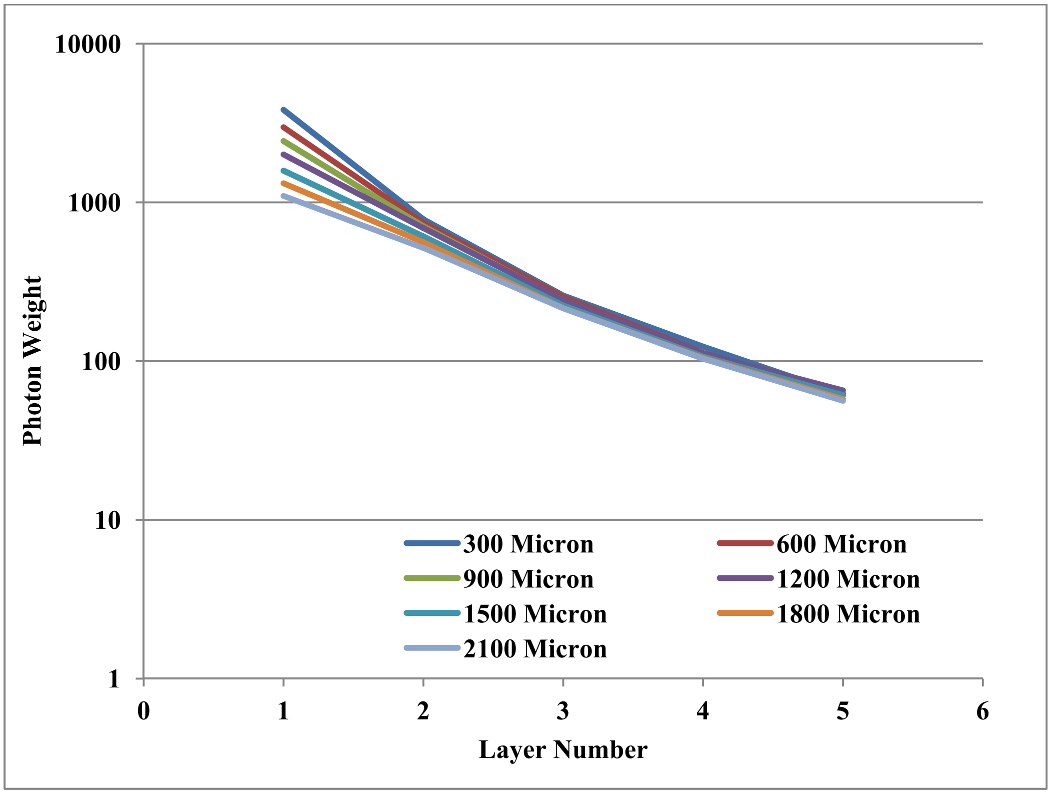

Figure 4.5a: *Photon weight deposited in the individual layer as a function of S-D. Each line represents a unique S-D (specified in the legend). Optical properties at 450 nm were used in this set of simulations.*

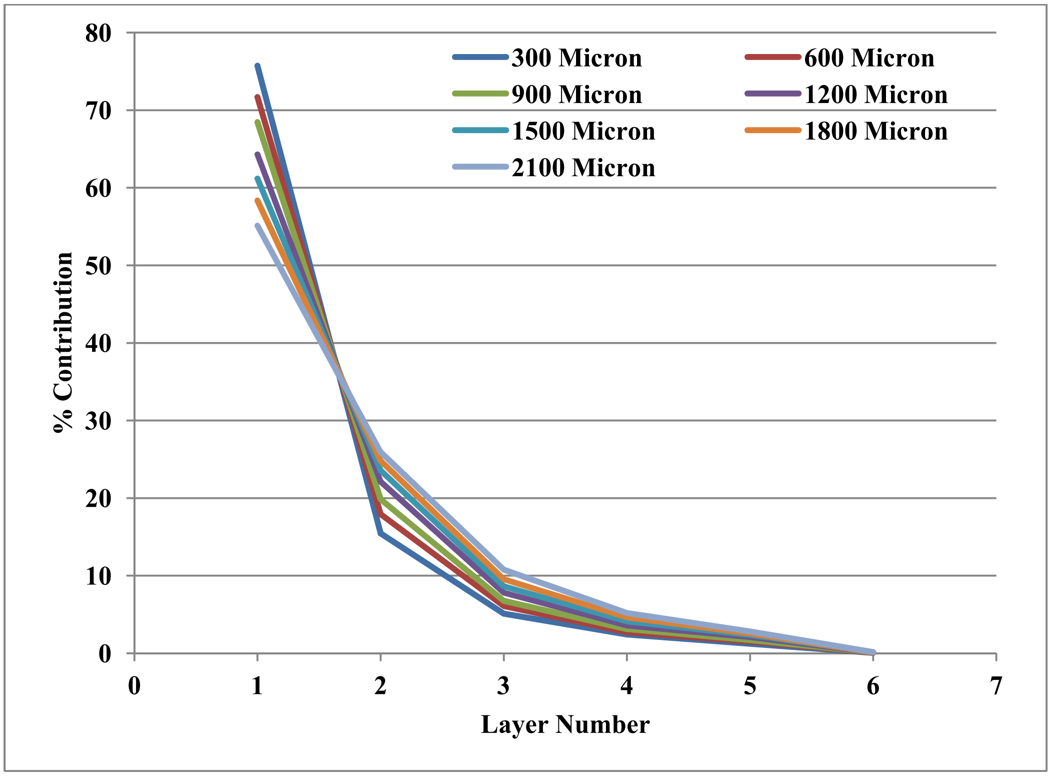

Figure 4.5b: *Percentage contribution of individual layer to the overall weight deposition (i.e., the reduction in the detected diffuse reflectance signal) as a function of S-D. Each line represents a unique S-D (specified in the legend). Optical properties at 450 nm were used in this set of simulations.*

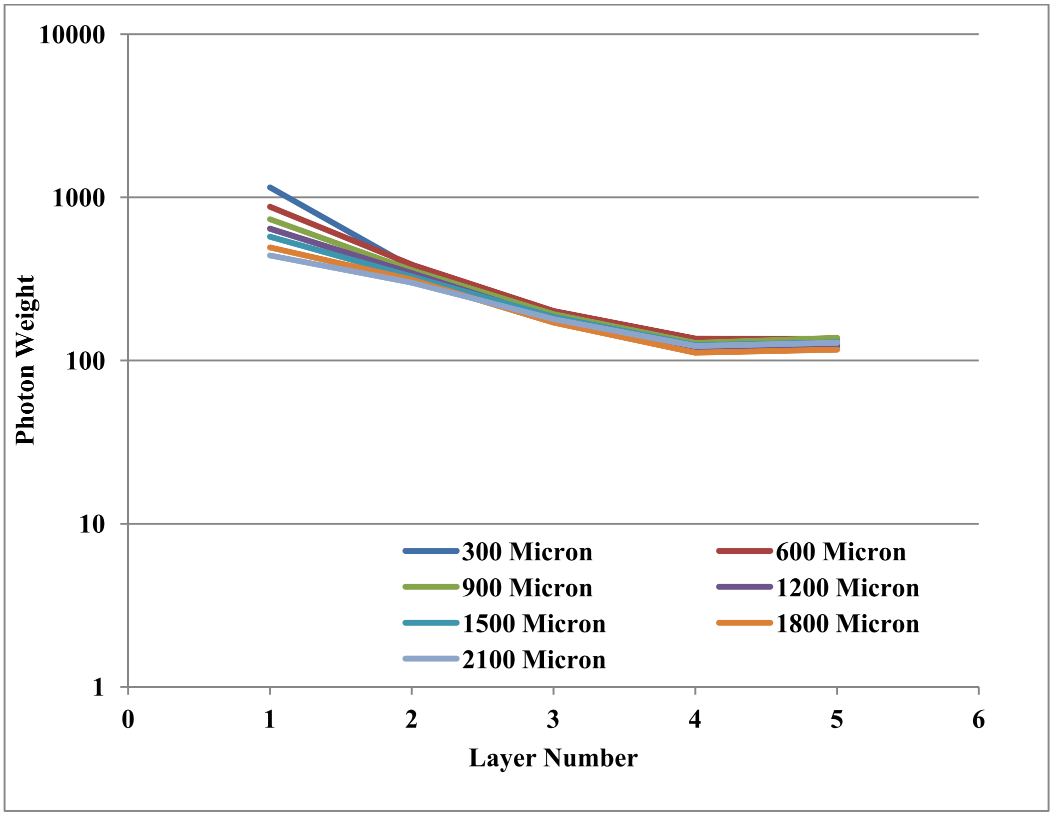

Figure 4.6a*: Photon weight deposited in the individual layer as a function of S-D. Each line represents a unique S-D (specified in the legend). Optical properties at 850 nm were used in this set of simulations.*

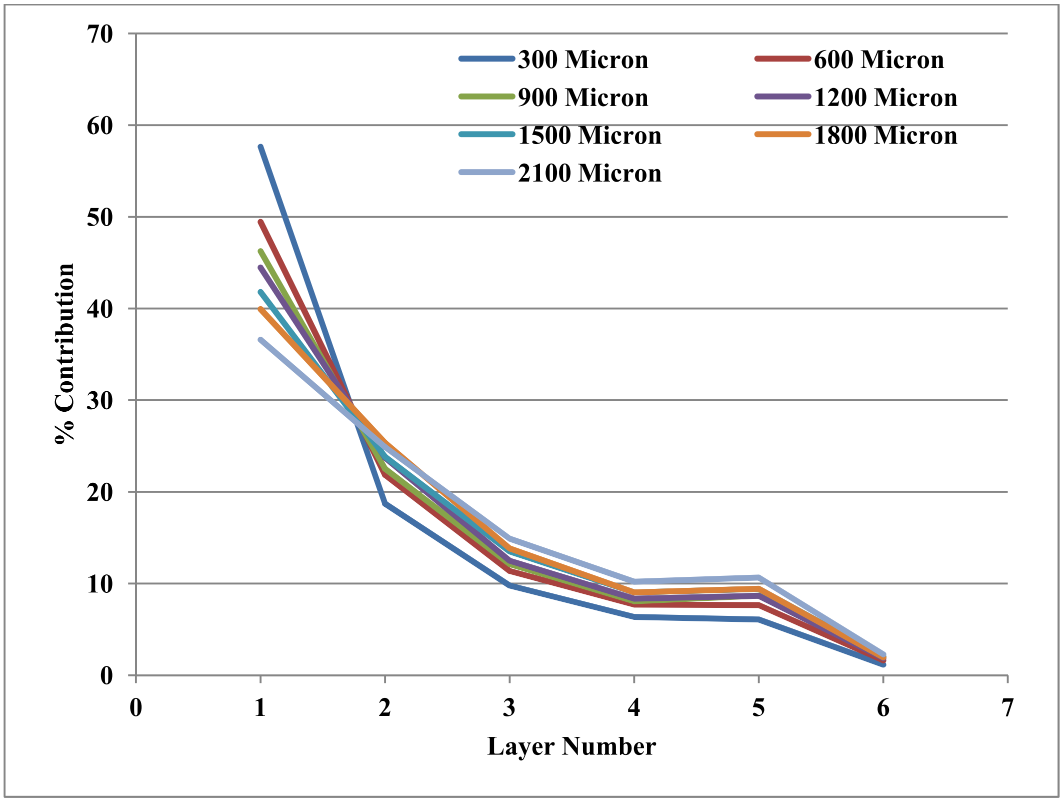

Figure 4.6b*: Percentage contribution of individual layer to the overall weight deposition (i.e., the reduction in the detected diffuse reflectance signal) as a function of S-D. Each line represents a unique S-D (specified in the legend). Optical properties at 850 nm were used in this set of simulations.*

4.2.3. Conclusions

As mentioned earlier, the histopathological features of epileptic cortex could be present at all layers of the cortex. Therefore, it is important to design an optical probe that can investigate the abnormality 4 mm beyond the cortical surface. According to the simulation results presented in the previous section, the depth of the investigation can be easily controlled by modifying the source-detector separation. Because of the highly absorbing and scattering nature of the cortex in the shorter wavelength region (i.e., < 600 nm), it is difficult to investigate deep tissue abnormality using diffuse reflectance signals in this wavelength band, regardless of what the source-detector separation is. In this longer wavelength region (i.e., > 600 nm), the efficiency of using diffuse reflectance signal to investigate the deep cortical abnormalities increases as the source detector separation increases. However the trade-off of increasing the source detector separation is the signal to noise level (S/N) is going to decrease significantly (see Figure 4.4). To meet the needs of high S/N as well as deep tissue investigation, it is important to keep the source-detector separation greater than 600 μm but smaller than 1000 μm, and the illumination should be beyond 600 nm.

4.3. Dynamic Spectroscopy System Design and Development

4.3.1. Introduction

The spectroscopic system used in the *in vivo* brain studies (see Chapter 3) was designed to capture the static nature of the investigated tissue. The existing knowledge about pediatric epileptic cortex leads one to believe that a wealth of diagnostic information about epileptic cortex may be found in the temporal variations of their intrinsic characteristics such as metabolism and hemodynamics. Therefore, it was the goal of this study to convert the existing static spectroscopy system (i.e., F(λ) and Rd(λ)) into a dynamic one (i.e., F(λ,t) and Rd(λ,t)). In order to perform time dependent measurements, it was instrumental to have a stable light source that provides stable excitation light. Due to its pulsed nature and limited repetition rate (i.e., 20 Hz), the nitrogen laser was deemed not suitable for the time dependent fluorescence spectroscopy study. The ideal replacement for the nitrogen laser would be CW UV lasers, but they are priced beyond the budget of the project. Therefore, the upgrade of the system only focused on the diffuse reflectance spectroscopy part. To achieve this goal, the following upgrades were planned:

(1) A sensitive spectrometer should be used to reduce the time required to acquire a single spectrum (i.e., integration time). Here the target integration time was 30 ms, which would yield a 33 Hz spectral acquisition rate matching with the frequency band of alpha waves.

(2) A powerful broadband light source with a high temporal stability should be used. The output power of the light source should be high enough to maintain the S/N of the acquired spectra above 20 and, at the same time, low enough not to induce thermal damage to the tissue.

(3) A fast controller with a larger memory capacity (i.e., more RAM) should be used to reduce the time required to write the spectral data to the hard drive during an acquisition procedure. The memory should be sufficiently large in order to allow continuous spectral acquisition for at least 12 seconds (i.e., 400 spectra) per investigation.

4.3.2. Materials and Methods

In order to perform the continuous diffuse reflectance spectral acquisition, the controller software was modified first. The modification allowed users to specify (1) the spectral acquisition rate (# of spectra per second), (2) the recording duration (total # of spectra acquired), and (3) the integration time for each spectral acquisition. To reduce the overhead resulting from directly writing the spectral data to the hard drive of the controller, the acquired spectra were stored in the RAM (4 GB) first and then saved to the hard drive upon completion of a single investigation.

To determine the applicability of the existing components in the static spectroscopy system for the time dependent spectroscopy measurements, the following studies were designed and carried out.

1. Quantify the noise level and characterize the noise characteristics ns(λ,t) of the existing spectrometer (USB2000, OceanOptics). The main purpose of this sub-study was to determine the magnitude and the frequency spectral composition of the spectrometer noise. The static spectroscopy system was used to acquire diffuse reflectance spectra from a non-biological subject (e.g., a piece of printer paper) without using the excitation light. The integration time was set at 30 ms, 100 ms, and 500 nm and the total number of the spectra acquired were 400. This experiment procedure was repeated twice: one without using the built-in boxcar smoothing function and the other with. The acquired spectra were preprocessed to reduce their spectral

resolution to 5 nm. The time history of the diffuse reflectance signal at a given wavelength (Rd(λ_a,t)) was retrieved from the data set. To analyze the temporal variation Rd(λ_a,t) during the recording period, the standard deviation of Rd(λ_a,t) was calculated. Furthermore, the distribution characteristics of Rd(λ_a,t) were reviewed using histogram analysis. Finally the frequency spectral composition of Rd(λ_a,t) was analyzed using Fourier transformation.

2. Quantify the noise level and the stability from the light source. The main purpose of this sub-study was to determine the noise originating from the excitation light source as well as its output stability. The spectroscopy system was used to acquire diffuse reflectance spectra from a non-biological sample (e.g., a piece of printer paper) with the excitation light turned on. The integration time of the spectroscopy system was set at 30 ms and the total number of spectra acquired was 400. The spectral acquisition was carried out after a fixed amount of the heating time of the white light source. The heating time used in this study was 0 second, 30 seconds, 40 seconds, 1 minute, 2 minutes, 3 minutes, 4 minutes, and 5 minutes. The boxcar smoothing function was used in this study. The acquired spectra were preprocessed to reduce their spectral resolution to 5 nm. The time history of the diffuse reflectance signal at a given wavelength (Rd(λ_a,t)) was retrieved from the data set. To analyze the effects of the heating time on the temporal variation Rd(λ_a,t), the standard deviation of Rd(λ_a,t) was calculated and plotted as a function of the heating time. Furthermore, the distribution characteristics of Rd(λ_a,t) was reviewed as a function of heating time using the histogram analysis. Finally the frequency spectral composition of Rd(λ_a,t) was analyzed as a function of the heating time using Fourier transformation.

Using the data from the light source stability evaluation, the S/N of the diffuse reflectance spectra at various signal strength levels was also evaluated. Here the mean value of

$Rd(\lambda_a,t)$ was calculated ($Rd_{mean}(\lambda_a)$) and subtracted from $Rd(\lambda_a,t)$ to yield the noise component of $Rd(\lambda_a,t)$ ($Rd_{noise}(\lambda_a,t)$). Finally, the $S/N(\lambda_a)$ was calculated by $Rd_{mean}(\lambda_a)/STD(Rd_{noise}(\lambda_a,t))$, where STD is the calculation of standard deviation. The $S/N(\lambda_a)$ was evaluated between 400 and 850 nm, where the main diffuse reflectance spectral band was, and its relationship with the magnitude of the signal was determined.

4.3.3. Results

4.3.3.1. Spectrometer Noise Analysis

A typical $Rd(\lambda_a,t)$ recorded without excitation light is shown in Figure 4.7, and its corresponding frequency spectrum is shown in Figure 4.8. Since the excitation light and the ambient light were off, $Rd(\lambda_a,t)$ recorded under such a condition represents the spectral signal (i.e., noise spectrum $NS(\lambda_a,t)$) originating from the spectrometer itself. It is noted that there are two components in the $NS(\lambda_a,t)$ of the spectrometer: a DC component and an AC component. The DC component is believed to be originated from the dark current of the detector of the spectrometer and is wavelength and time independent. Therefore, it can be easily estimated by calculating the mean of $NS(\lambda_a,t)$. The AC component of $NS(\lambda_a,t)$ is a random fluctuation; its frequency spectrum suggests that it strongly resembles white noise (i.e., the power spectral density is relative uniform over the entire frequency spectral range). The histograms of the AC component (Figure 4.9) suggest that the magnitude of this random fluctuation has normal distribution characteristics. The maximum and minimal magnitudes of the AC component are about + 9 and – 9, respectively, and they are wavelength and integration time independent (Figure 4.10). The standard deviation of the AC component is about 3, which is also wavelength and integration time independent (Figure 4.11). Since the maximal spectral intensity of the existing spectrometer is 4096 au; the maximum signal to noise ratio of the diffuse reflectance spectra recorded would be S/N = 4096 au/18 au = 227. In order to maintain the signal to noise level above 20, the true signal in Rd(λ_a,t) has to be greater than 360 au.

The application of the real-time boxcar smoothing significantly reduces the AC components in NS(λ_a,t), as shown in Figures 4.12 and 4.13, as well as the magnitude of its frequency components. According the mean and standard deviation calculation of smoothed NS(λ_a,t) shown in Figures 4.8 and 4.9, the smooth function effectively provides a 10-fold reduction of the spectrometer noise. More importantly, the boxcar smoothing can be performed in real time and hence does not affect the goal of continuously acquiring diffuse reflectance spectra at 33 Hz. It also allows detection of weak fluctuations in diffuse reflectance signals resulting from the regional alterations in physiological characteristics of the investigated tissue.

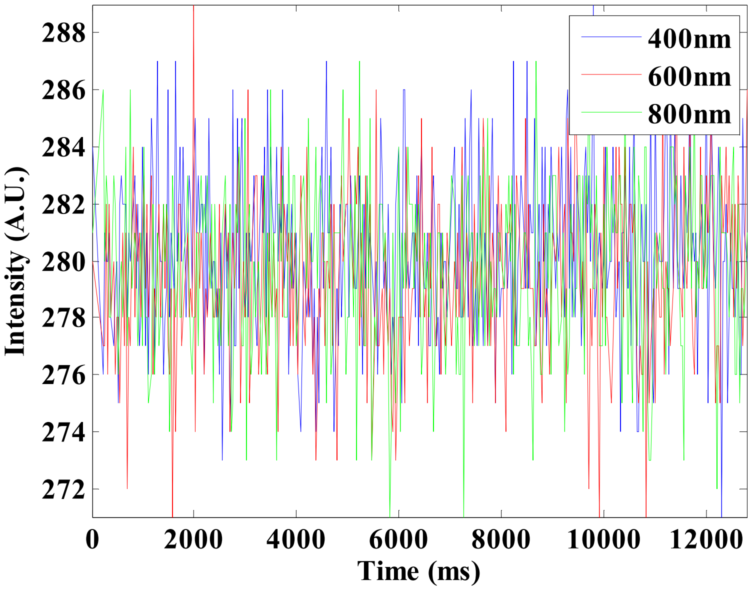

Figure 4.7: *Rd(λ_a,t) at λ_a = 400, 600, and 800 nm. The integration time is 30 ms, and the total number of spectra acquired (i.e., the number of data points along the time axis) is 400.*

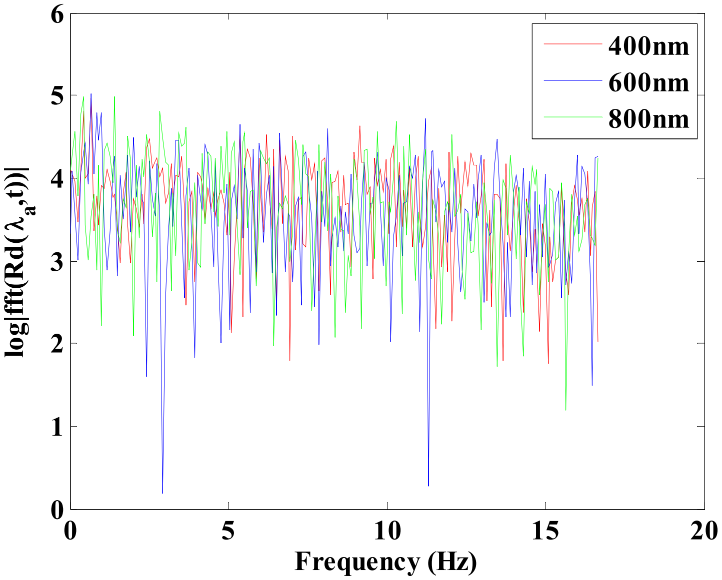

Figure 4.8: *Frequency spectra of Rd(λ_a,t) at λ_a = 400, 600, and 800 nm. The integration time is 30 ms.*

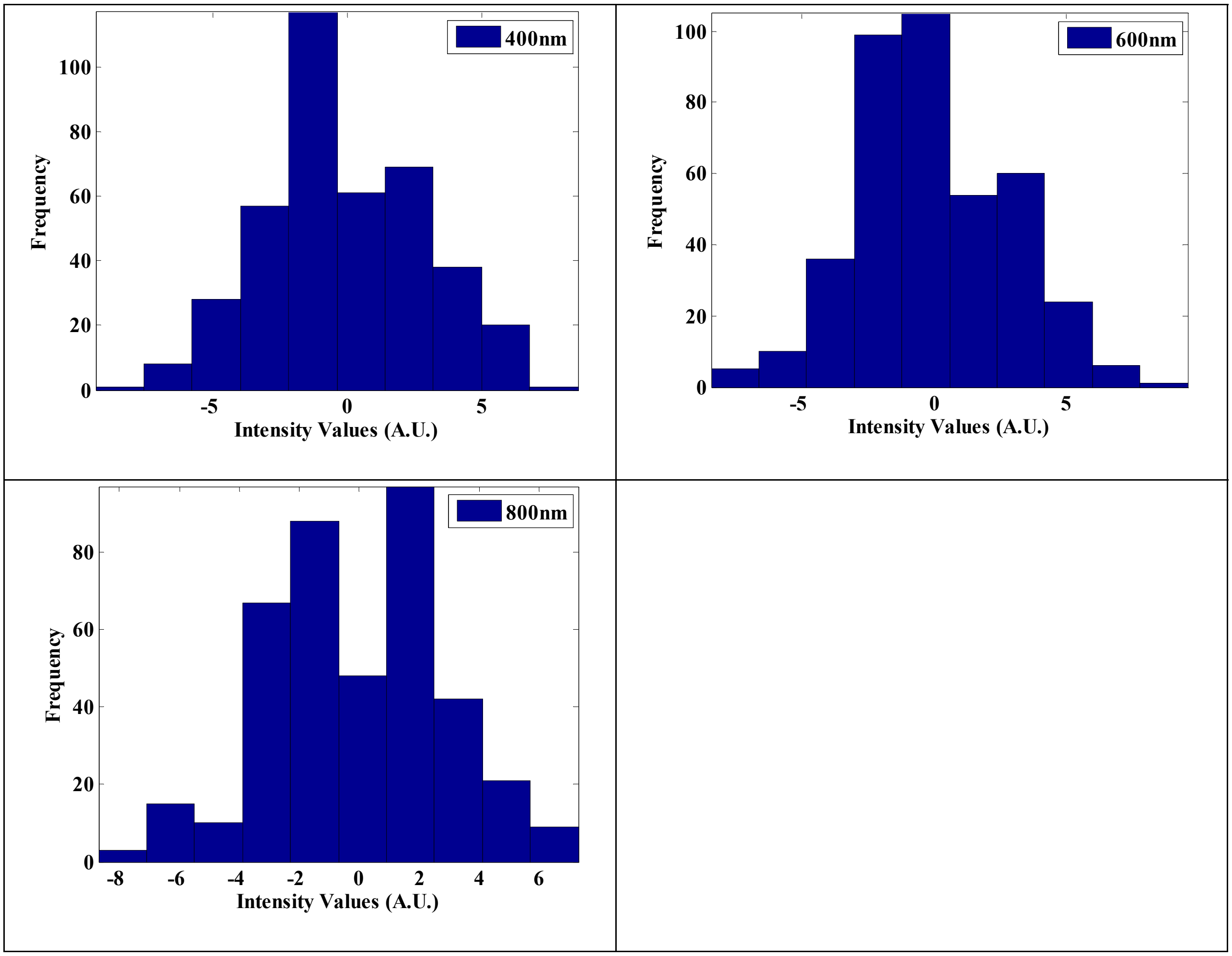

Figure 4.9: *The histograms of the AC component of NS*(λ_a,*t*) *at* λ_a = *400, 600, and 800 nm.*

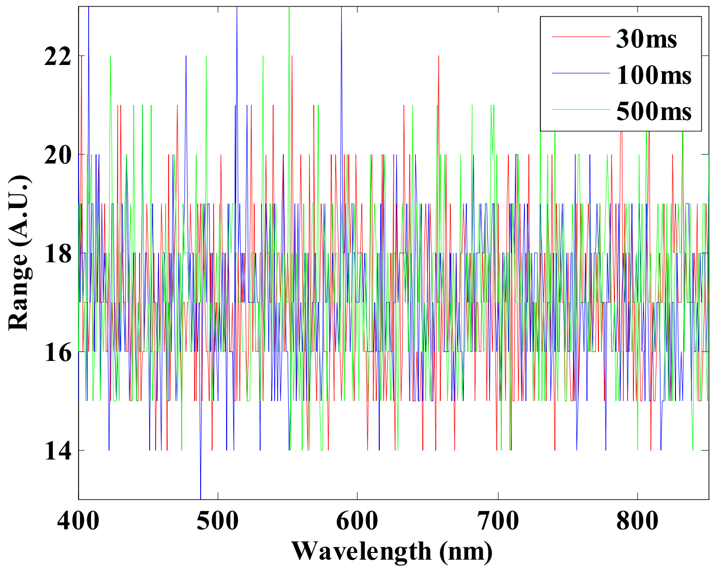

Figure 4.10*: The difference between Max and Min of NS(λ_a,t) (i.e., Max(NS)-Min(NS)) within a single recording period between 400 and 850 nm. The legend indicates the integration time used.*

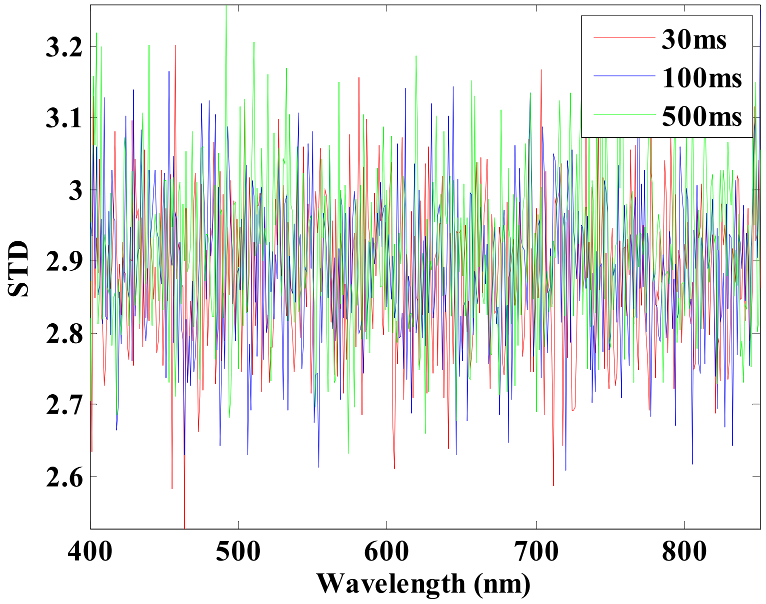

Figure 4.11*: The standard deviation of NS(λ_a,t) within a single recording period as a function of wavelength. The legend indicates the integration time used.*

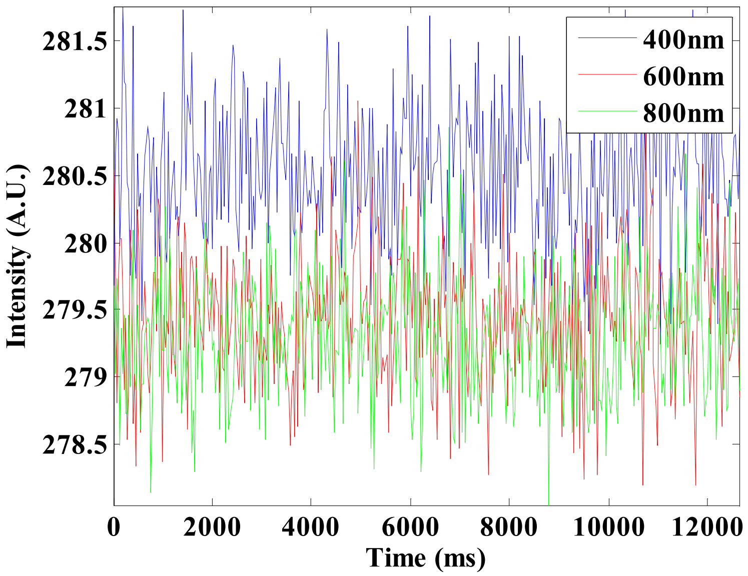

Figure 4.12: *Smoothed Rd(λ_a,t) at λ_a = 400, 600, and 800 nm. The integration time is 30 ms, and the total number of spectra acquired is 400. Here boxcar smoothing with a window size of 20 was used to smooth the individual spectrum (i.e., Rd(λ)). The smoothing was performed in real-time during the spectral acquisition.*

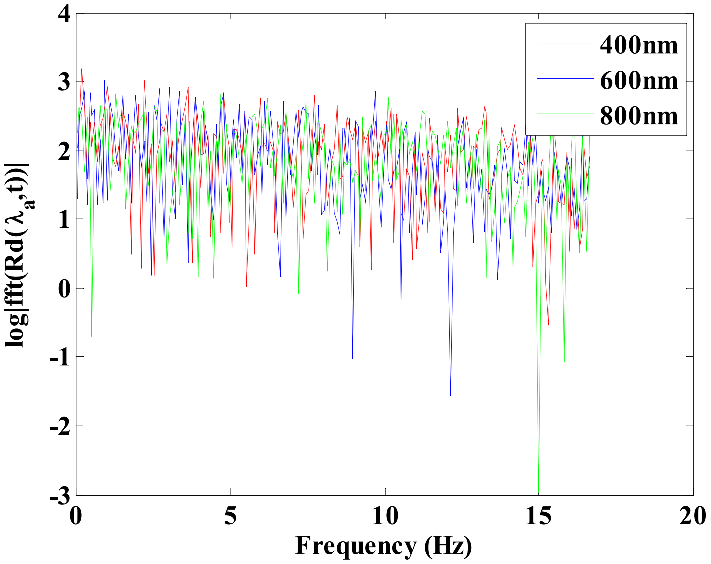

Figure 4.13: *Frequency spectra of smoothed Rd(λ_a,t) at λ_a = 400, 600, and 800 nm. The integration time is 30 ms, and the total number of spectra acquired is 400. Here boxcar smoothing with a window size of 20 was used to smooth the individual spectrum (i.e., Rd(λ)). The smoothing was performed in real-time during the spectral acquisition.*

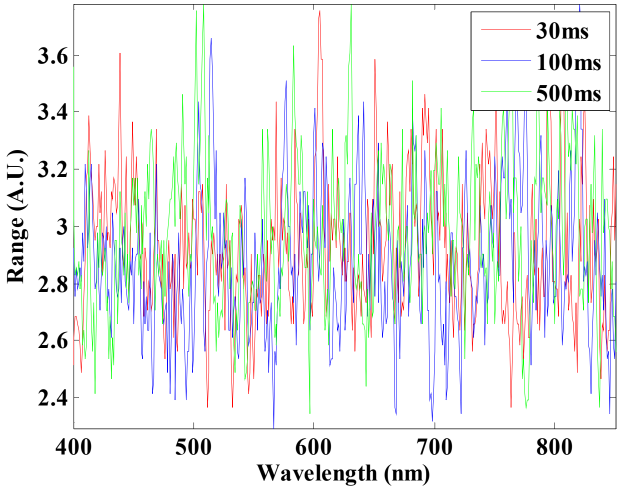

Figure 4.14: *The difference between Max and Min of the smoothed NS(λ_a,t) (i.e., Max(NS)-Min(NS)) within a single recording period between 400 and 850 nm. The legend indicates the integration time used.*

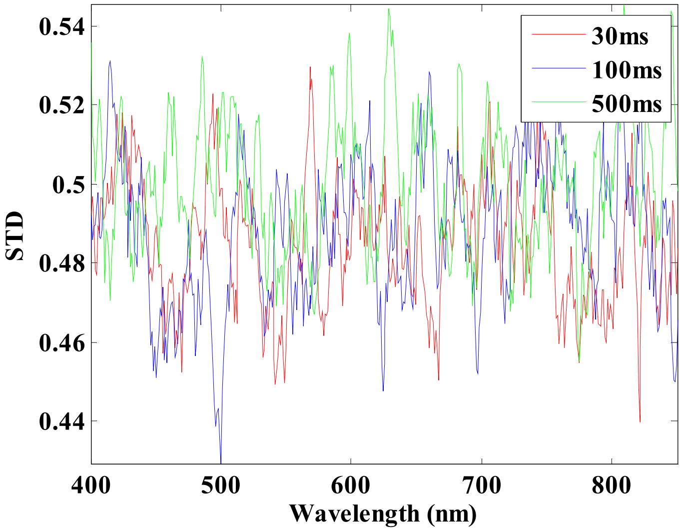

Figure 4.15: *The standard deviation of the smoothed NS(λ_a,t) within a single recording period as a function of wavelength. The legend indicates the integration time used.*

4.3.3.2. Light Source Characteristics

Since the new spectroscopy system aims to investigate temporal variations in the physiological characteristics of the brain, it is instrumental that the light source does not introduce additional noise to the recorded spectra. The light source used in the new spectroscopic system is a CW tungsten light source; therefore, the main source of the noise would be the drifting of the output power of the light source. As shown in Figures 4.16 and 4.17, the output power of the light source is dependent of the heating time allowed. Immediately after the white light source is turned on, it is noticed that Rd(λ_a,t) steadily decreases as a function of time and this decline trend is wavelength independent. This indicates that the overall output power of the light source decreases gradually during the initial operation. The existence of this declining trend significantly increases the low frequency component of Rd(λ_a,t), which could overwhelm slow-varying physiological signals such as low frequency hemodynamic oscillation. Thirty seconds after the light source was turned up, it is noticed that the drifting of Rd(λ_a,t) became much less significant and the output power of the light source reached a steady state. When the light source is allowed to heat up for at least 30 seconds, the noise characteristics of Rd(λ_a,t), which is the AC component of Rd(λ_a,t), is comparable to that of the spectrometer in terms of magnitude, magnitude distribution, and frequency composition.

<table>
<tr>
<td>a</td>
<td>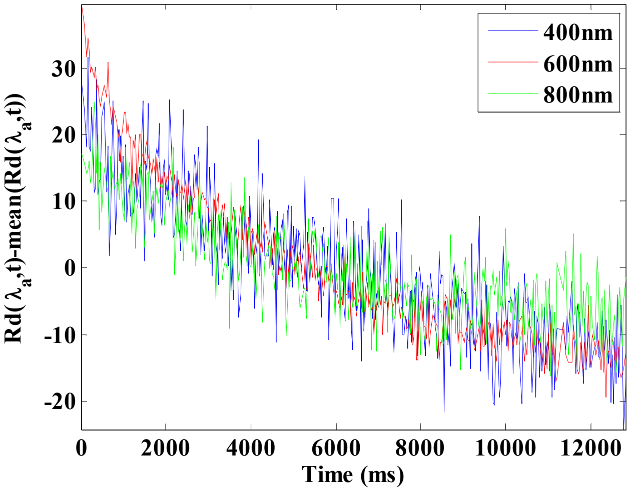
400nm
600nm
800nm
Rd(λa,t)-mean(Rd(λa,t))
30
20
10
0
-10
-20
0
2000
4000
6000
8000
10000
12000
Time (ms)</td>
</tr>
<tr>
<td>b</td>
<td>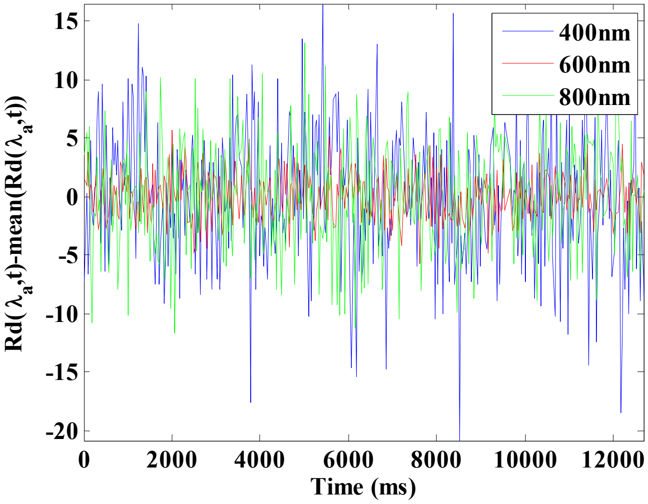
400nm
600nm
800nm
Rd(λa,t)-mean(Rd(λa,t))
15
10
5
0
-5
-10
-15
-20
0
2000
4000
6000
8000
10000
12000
Time (ms)</td>
</tr>
</table>

c	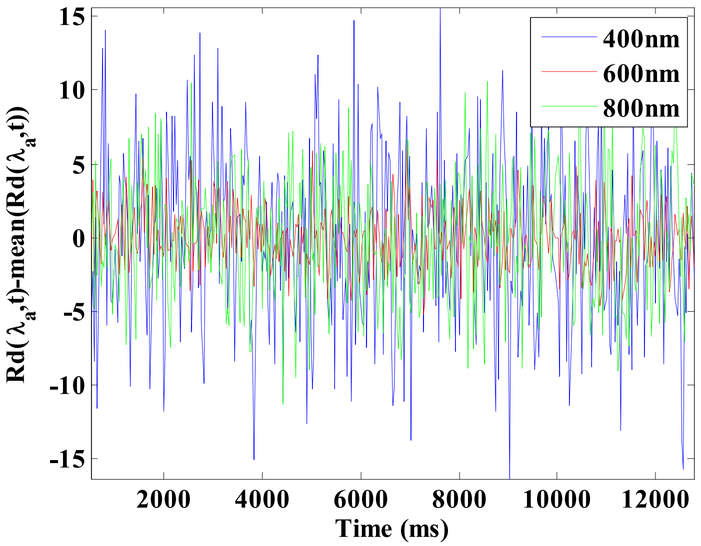
d	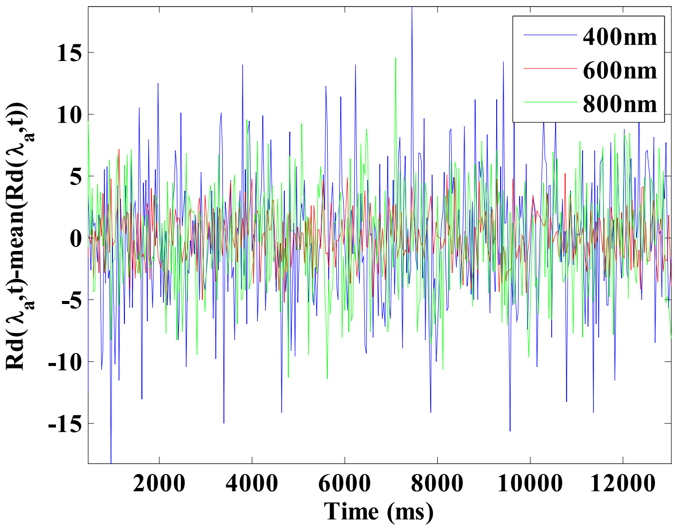

Figure 4.16: *Time history of Rd(*λ_a*,t) at* λ_a *= 400, 600, and 800 nm. Heating time is (a) 0 second, (b) 30 seconds, (c) 1 minutes, and (d) 5 minutes. Note the mean value of Rd(*λ_a*,t) within one recording period was subtracted from Rd(*λ_a*,t) in these plots.*

<table>
<tr>
<td>a</td>
<td>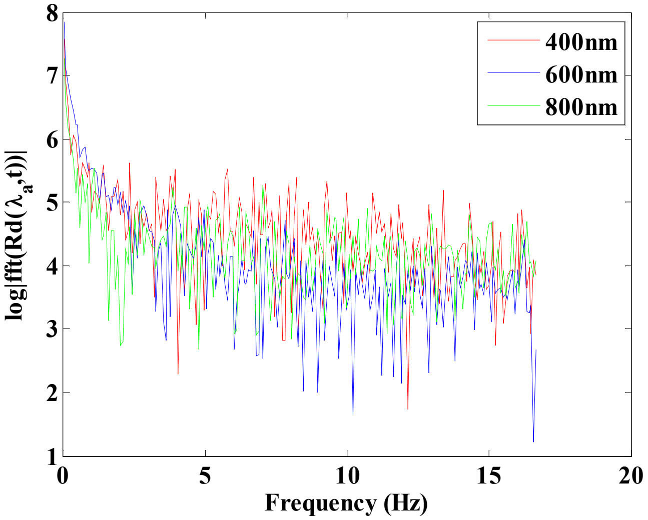

400nm
600nm
800nm
log|fft(Rd(λ_a,t))|
8
7
6
5
4
3
2
1
0
5
10
15
20
Frequency (Hz)
</td>
</tr>
<tr>
<td>b</td>
<td>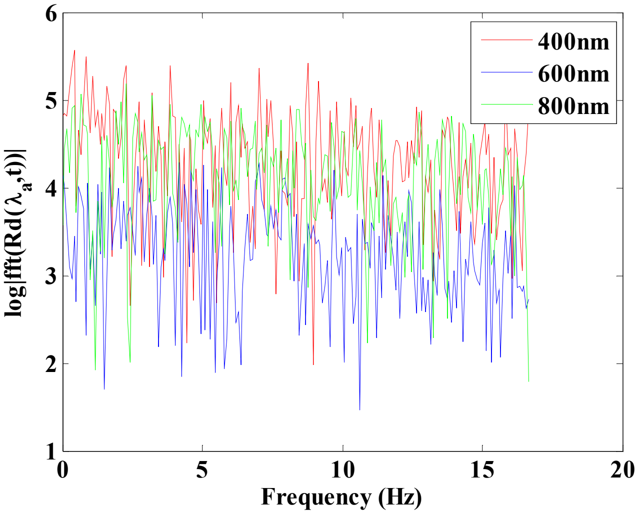

400nm
600nm
800nm
log|fft(Rd(λ_a,t))|
6
5
4
3
2
1
0
5
10
15
20
Frequency (Hz)
</td>
</tr>
</table>

c	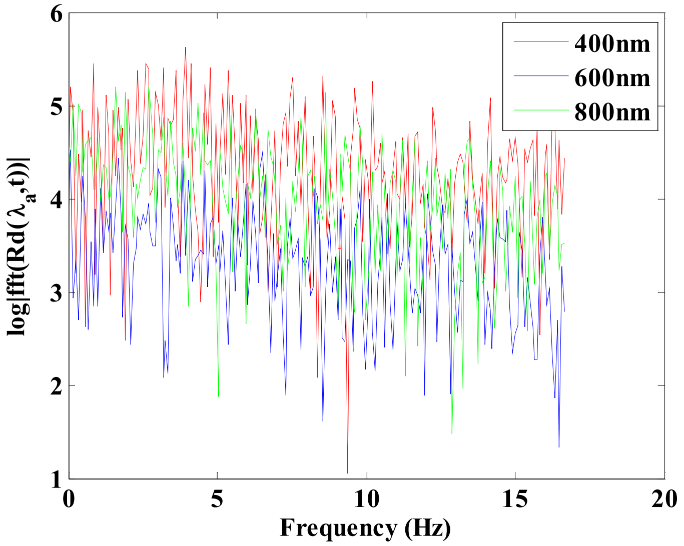
d	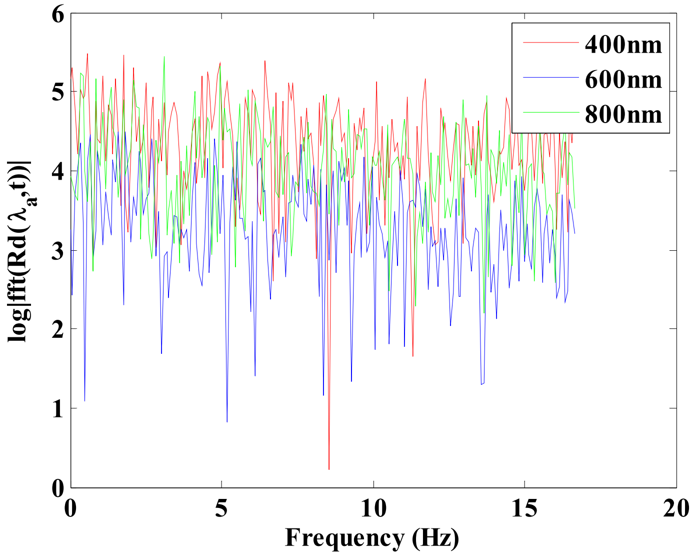

Figure 4.17*: Frequency spectra of Rd(λ_a,t) at λ_a = 400, 600, and 800 nm. Heating time is (a) 0 second, (b) 30 seconds, (c) 1 minutes, and (d) 5 minutes.*

4.4. Discussion and Conclusions

The probe design analysis shows that the source detector separation in a fiberoptic probe designs strongly influences the sensitivity of the measured diffuse reflectance signals to the variations at different depth of the cortex. While increasing the source detector separation allows detection of deep abnormality within the cortex, the trade-off is low S/N, which is especially severe in the wavelength region where the scattering and absorption properties are high. Furthermore, this trade-off would significantly impact the capability of performing high speed time dependent diffuse reflectance spectral acquisition from the cortex. It is found that the optical probe designed for the static spectroscopy system provides an investigation depth of ~ 1 mm, which encompasses the second and the third layers of the cortex. Since the dynamic measurement aims to probe the hemodynamics of the cortex and the vascular density in layer two and three of the cortex is large, it is possible to use the existing optical probe to investigate the hemodynamic characteristics of the epileptic cortex as a function of time.

The noise analysis of the spectrometer and the light source reveals distinct noises characteristics for each device. The spectrometer contributes two types of noises: a DC one originating from the dark current of the detector and an AC one similar to the white noise. The DC noise of the spectrometer is wavelength and integration time independent, and can be easily removed by subtracting the mean from the recorded signal. The AC component is random and has a broad frequency spectral band (i.e., white noise) and cannot be removed using the conventional filtering techniques. Nevertheless, the results of the noise study show that smoothing the diffuse reflectance spectra using a boxcar filter significant reduces the magnitude of the AC component of the spectrometer noise. Therefore it is possible to utilize this filter in real time to reduce the noise introduced by the spectrometer in the recorded data. The noise from the light source, on the other hand, is a low frequency one: the output power of the light source decreases gradually during the first 30 seconds of the operation and then reaches a steady state. In order to avoid the interference of output instability of the light source to the time dependent diffuse reflectance signal records, it is recommended that the light source should be turned on at least 30 seconds prior to a single spectral acquisition process. In conclusion, the analysis performed in this chapter provides valuable insights into the construction of a time dependent diffuse reflectance spectroscopy system for *in vivo* epileptic cortex study. More importantly, it suggests that the static spectroscopy system (the diffuse reflectance part) could be used to investigate the hemodynamic characteristics of the human cortex with some modifications to the data acquisition software and hardware designs of the controller and the system. These modifications were carried out and the dynamic system was used in another *in vivo* human study. Details about this study can be found in the next chapter.

5. Improving the quality of time-dependent, diffuse reflectance spectroscopic signals measured from *in vivo* brain during craniotomy by reducing motion artifacts

5.1. Introduction

Spectroscopy-based optical diagnostic technologies have been investigated and evaluated widely over the past two decades; they are primarily used to detect pre-cancer in various tissue organs [93, 130-134] and guide tumor resection intraoperatively [51, 69, 135, 136]. These technologies are built upon the principle of light-tissue interactions: light absorption and scattering inside a biological tissue are governed by the tissue's structural and compositional characteristics and these intrinsic characteristics are altered by disease and/or injury [133, 137-141]. These technologies hold several advantages over existing diagnostic technologies, in that they are relatively inexpensive, highly portable, and can be used real-time. To make these technologies applicable within an *in vivo* or intraoperative environment, a sterilized contact probe often is employed to achieve remote sensing from *in vivo* tissue. The probe typically is held by the hand of an operator. One common problem with such a practice is motion artifacts in the acquired data. Unintentional hand movements or tremors alter the pressure of the probe against the target tissue or shift the site of investigation. Ultimately, these movements are incorporated into the data as noise or artifacts. A couple of earlier reports have suggested that probe pressure does not significantly affect fluorescence intensity of the cervix [143, 144]. A similar finding was noted in a study in which Raman spectroscopy was used to detect pre-cancerous lesions within the gastrointestinal tract [145]. However, several other studies have shown that excessive probe contact pressure, resulting from hand movements, can lead to strong alterations in the hemodynamic and metabolic characteristics of local tissue [146-151]. In addition, the effect of varying probe contact pressure on acquired optical spectral data is tissue type dependent: the softer the tissue, the greater the effect [142]. Despite this recognition, the intrinsic characteristics of the spectral artifacts induced by hand motions have not yet been thoroughly investigated, and no systematic approach to combat this obstacle has been proposed.

In this paper, we report the results of an *in vivo* study of the brains of pediatric patients undergoing epilepsy surgery, so as to quantify the spectral and temporal artifacts induced by hand motions. Specifically, time-dependent diffuse reflectance spectra were acquired from the normal cortex of patients during epilepsy surgery using a fiber-optic spectroscopy system. Two distinct methods of spectral data acquisition were compared: one with the fiber-optic probe held by the surgeon's hand during data acquisition, and the other with the probe held by a mechanical probe holder. The probe holder was devised to eliminate hand-motion artifacts in the recording and to counteract any spontaneous movements of the *in vivo* brain. Recordings from the two data-acquisition methods were compared in the time, frequency, and wavelength domains, using both descriptive and inferential statistics. From these results, the characteristics of spectral artifacts induced by hand movements were determined and characterized.

5.2. Materials and Methods

5.2.1. Instrumentation

The instrumentation for *in vivo* diffuse reflectance spectral acquisition consisted of a fiber-optical probe and a portable spectroscopic system. It was calibrated using a calibrated tungsten halogen light source (LS-1-CAL, Ocean Optics, Dunedin, FL) in order to remove any spectral alterations induced by the instrument. Details of this system can be found in a previous publication by our group [69].

5.2.2. Design of the Probe Holder

A mechanical probe holder was designed and engineered to eliminate the need for a surgeon to hold the optical probe throughout a single data acquisition procedure. The introduction of this holder enabled us to identify and, hence, quantify the spectral alterations induced by hand movements. The three critical design criteria of the probe holder were: (1) it had to be able to withstand the ethylene oxide gas sterilization procedure; (2) it had to maintain a stable investigation location of the probe; and (3) it should maintain constant probe-contact pressure, if feasible, against the *in vivo* brain tissue. The final design of the probe holder is depicted in Figure 5.1. To meet the sterilization criterion, medical grade Stainless Steel 361 was used to construct the entire holder. To meet the stability criterion, the probe holder was designed to be used in conjunction with the Greenberg self-retaining retractor system. This approach reduced the susceptibility of the probe holder to movements of the patient during data acquisition, as the Greenberg system [152] was attached directly to the Mayfield head clamp (Integra LifeSciences Corp. Cincinnati OH, USA) which was attached to the surgical bed. The center of the probe holder is a stainless-steel tube with an inner diameter slightly larger than the diameter of the optical probe. The optical probe is inserted through the tube and secured using a side screw. To enable movement of the optical probe along its primary axis, the center tube was attached to the frame of the holder via a two-bar track system (Figure 5.1). To further facilitate axial movements of the optical probe, four springs were used in the track system to suspend the probe. The combined spring constant of this suspension system is 250 N/m. Since the free weight of the probe is about 26 g, the displacement of the springs was about 1 mm when the probe was loaded to the probe holder. Using the flat punch indentation model of viscoelastic solids derived by Harding and Sneddon [153] as well as the shear modulus of the brain reported by Green *et al*

[154], it was found that the addition of the damping springs in the probe holder would also reduce the variation in probe contact pressure, resulting from the spontaneous brain movements, by about 20% (Table 5.1). This type of variation in probe contact pressure may be further minimized by reducing the overall spring constant. The trade-off of such an approach, however, would be a significant increase in the loading displacement of the springs, and hence the size of the probe holder.

Brain Movement (mm)	Contact Force (N)		
	k = 0	k = 245 N/m	k = 50 N/m
0.1	0.00635	0.00508	0.001905
0.5	0.03175	0.0254	0.009525
1	0.0635	0.0508	0.01905
Reduction (%)		20%	80%

Table 5.1: *The effects of the damping springs on the probe contact force. The calculations were conducted using the shear modulus of the brain = 5K Pa. Here k is the total spring constant of the probe holder, and k = 0 represents the probe holder without damping mechanism.*

5.2.3. Data Acquisition and Preprocessing

In this study, *in vivo* time-dependent diffuse reflectance spectra *Rd(λ,t)* were acquired from the *in vivo* brains in the operating room from pediatric patients who were undergoing epilepsy surgery. A total of 18 patients were enrolled in the study. From each patient, data was collected from one normal site. There was a patient from whom the data was collected from other normal sites as well. Hence, the total number of sites was 20. The study was approved by the IRBs at Miami Children's Hospital and Florida International University. Informed written consent was obtained from the parents or guardians of each participant. The patients were divided evenly into two groups. In one group, data acquisition was performed with the probe holder (*Holder Group*). In the other group, the probe holder was not used (*Hand Group*).

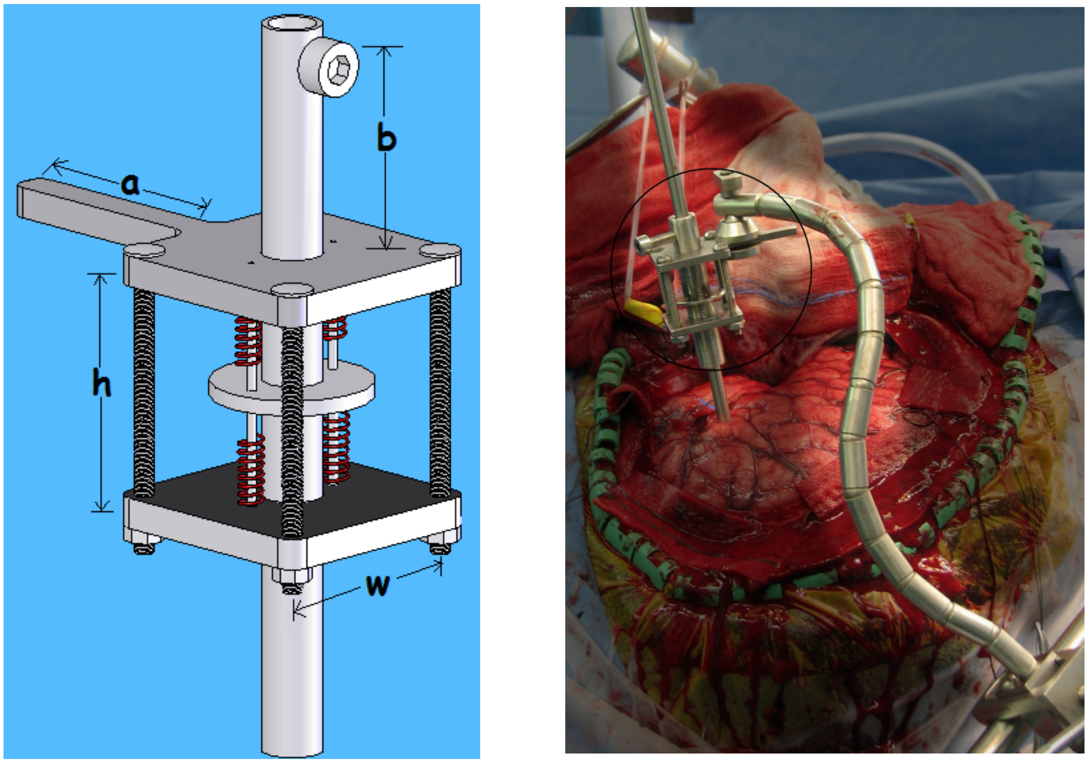

(a) *(b)*

Figure 5.1*: (a) Schematic of the mechanical holder for the fiber optic probe. Here h = w = 1 inch and a = b = 1 inch. (b) The probe holder is attached to a Greenberg retractor system during in vivo data acquisition.*

In this trial, spectral data were acquired only from normal cortex, as defined by intraoperative electrocorticography and pre-operative imaging. Prior to data acquisition, each investigated site was rinsed with saline to remove surface blood, and the surgeon gently placed the optical probe in direct contact with the target tissue. In addition, the broadband white light source was pre-heated for at least 30 seconds to stabilize its output. Sequentially, 400 $Rd(\lambda,t)$ were acquired from the investigated site at a rate of 30 spectra per second (i.e., 30 ms integration time). Upon completion of spectral acquisition, the white light was turned off and a baseline spectrum was acquired to document the influence of ambient light. Every stage of the study protocol was carried out under the careful supervision of the surgeons, such that patient care was not compromised.

A standard data pre-processing routine was applied to all acquired $Rd(\lambda,t)$, so as to eliminate spectral variations induced by the instrumentation and ambient light [69]. During the spectral pre-processing procedure, the range of $Rd(\lambda,t)$ was reduced to 400-850 nm with a wavelength interval of 5 nm. These pre-processing procedures yielded a set of calibrated diffuse reflectance spectra $Rd_{cal}(\lambda_i,t)$.

5.2.4. Data Analysis

$Rd_{cal}(\lambda_i,t)$ was analyzed in time, frequency and temporal correlation domains to identify the characteristics of spectral alterations induced by hand movements. Furthermore, the degree of improvement in the quality of $Rd_{cal}(\lambda_i,t)$ attributable to the probe holder was assessed quantitatively.

To characterize the temporal alterations induced by hand movements, $Rd_{cal}(\lambda_i,t)$ from the Holder and the Hand groups were compared empirically by an experienced spectral analyzer (WCL). Time variations in $Rd_{cal}(\lambda_i,t)$ at a given wavelength were quantified further using its percentage standard deviation, which is calculated as

$$\%STD\_Rd_{cal}(\lambda_i) = STD(Rd_{cal}(\lambda_i,t))/MEAN(Rd_{cal}(\lambda_i,t)), \tag{5.1}$$

where STD is the standard deviation calculation along the time axis, MEAN is the overall average calculation along the time axis, and λ_i = 400 nm to 850 nm at 50 nm intervals. Finally, statistical comparisons were performed of $\%STD\_Rd_{cal}(\lambda_i)$ from the Holder and Hand groups to estimate the degree of improvement which can be attributed to the probe holder on the quality of acquired data.

To investigate wavelength-dependency of the temporal spectral alterations in $Rd_{cal}(\lambda_i,t)$ induced by hand movements, temporal correlation analysis of $Rd_{cal}(\lambda_i,t)$ was conducted. Here, two signals within a single recording set, $Rd_{cal}(\lambda_i,t)$ and $Rd_{cal}(\lambda_{ref},t)$, were used to calculate correlation coefficients $r(\lambda_i,\lambda_{ref},t)$ for a fixed time window (Δt), expressed as

$$r(\lambda_i,\lambda_{ref},t)=\frac{COV[Rd(\lambda_i,t:t+\Delta t),Rd(\lambda_{ref},t:t+\Delta t)]_i}{STD[Rd(\lambda_i,t:t+\Delta t)]*STD[Rd(\lambda_{ref},t:t+\Delta t)]} \tag{5.2}$$

where COV is the calculated covariance. In this analysis, λ_{ref}= 800 nm was used as it is in the spectral region where hemoglobin absorption is not prominent, and the window size used was 25 samples (i.e., Δt = 750 ms). Again, $r(\lambda_i,\lambda_{ref},t)$ from the Holder and Hand groups were empirically evaluated to identify wavelength-dependency of spectral alterations in $Rd_{cal}(\lambda_i,t)$ induced by hand movements. Furthermore, the mean of $r(\lambda_i,\lambda_{ref},t)$ over the entire recording duration, denoted as $MEAN(r(\lambda_i, \lambda_{ref}, t))$, was calculated. Here, the range of λ_i was 400 to 850 nm at 50 nm intervals. Finally, statistical comparisons were performed of $MEAN(r(\lambda_i, \lambda_{ref}, t))$ from the Holder and Hand groups to estimate the extent of improvement which can be attributed to the probe holder on the quality of acquired data.

The frequency composition of $Rd_{cal}(\lambda_i,t)$ was analyzed to determine the frequency characteristics of the spectral alterations induced by hand motions. To eliminate the contribution of the DC component to the analysis, the mean intensity over the entire recording period was removed from $Rd_{cal}(\lambda_i,t)$. That is

$$Rd_{cal\_ac}(\lambda_i) = Rd_{cal}(\lambda_i, t) - MEAN(Rd_{cal}(\lambda_i,t) \tag{5.3}$$

Fourier transformation then was applied to $Rd_{cal\_ac}(\lambda_i)$, which produced a frequency spectrum $FT\_\ \lambda_i(f)$. The absolute value of $FT\_\ \lambda_i(f)$ was computed to yield $FT_{abs}\_\lambda_i(f)$, which shows the magnitudes of the frequency components. From $FT_{abs}\_\lambda_i(f)$, locations of the prominent frequency components were identified and their correlations with the physiological characteristics of the brain were explored. The power spectral energy of $FT_{abs}\_\lambda_i(f)$, $P(\lambda_i)$,was calculated by integrating $[FT_{abs}\_\lambda_i(f)]^2$ over the entire frequency range, for λ_i = 400 to 850 nm in 50 nm intervals. Finally, statistical comparisons were performed with $P(\lambda_i)$ from the Holder and Hand groups to estimate improvement in the quality of the acquired data caused by the probe holder.

5.3. Results

5.3.1 Temporal Variations in $Rd_{cal}(\lambda_i, t)$

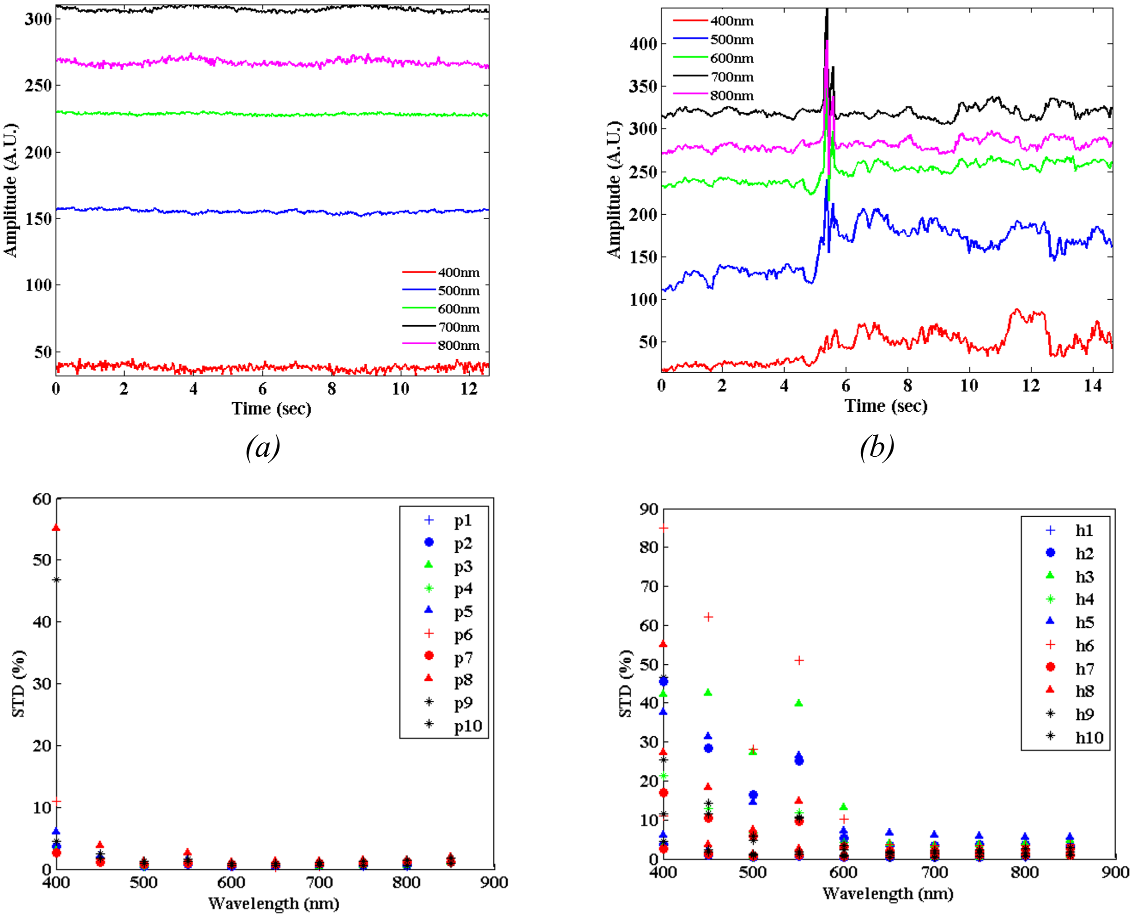

(a) *(b)*

(c) *(d)*

Figure 5.2: *(a) and (b) are the representative* $Rd_{cal}(\lambda,t)$ *from the Holder and Hand groups, respectively. (c) and (d) are* $\%STD\_Rd_{cal}(\lambda_i)$ *calculated using* $Rd_{cal}(\lambda,t)$ *from the Holder and Hand groups, respectively. Figure legends p1 to p10 are sites from Probe Holder group and h1 to h10 are sites from Hand Held group.*

Temporal variations in $Rd_{cal}(\lambda,t)$ from the Holder group were insignificant (Figure 5.2a) at all wavelengths as shown in Table 5.2. In contrast, strong variations often were observed in $Rd_{cal}(\lambda,t)$ from the Hand group. These variations did not possess any predictable nature (e.g., cycling) and often occurred at all wavelengths. Results from the quantitative analysis of $Rd_{cal}(\lambda,t)$ in the time domain suggest that time variations in $Rd_{cal}(\lambda,t)$ from the Holder group, in general, were much less than those from the Hand group (Figures 5.3c and d). Two sample t-tests (for normal data) and the Kolmogorov-Smirnov test (for non-normal data) of *%STD_*$Rd_{cal}(\lambda_i)$ further confirmed that the decrease in temporal variations in $Rd_{cal}(\lambda,t)$, resulting from the employment of the probe holder, was statistically significant (Table 5.2). In the Hand group, it also is noted that *%STD_*$Rd_{cal}(\lambda_i)$ between 400 and 600 nm was stronger than that beyond 600 nm, which suggests that $Rd_{cal}(\lambda,t)$ between 400 and 600 nm was more susceptible to hand movements.

5.3.2 Temporal Correlation in Rd(λ,t)

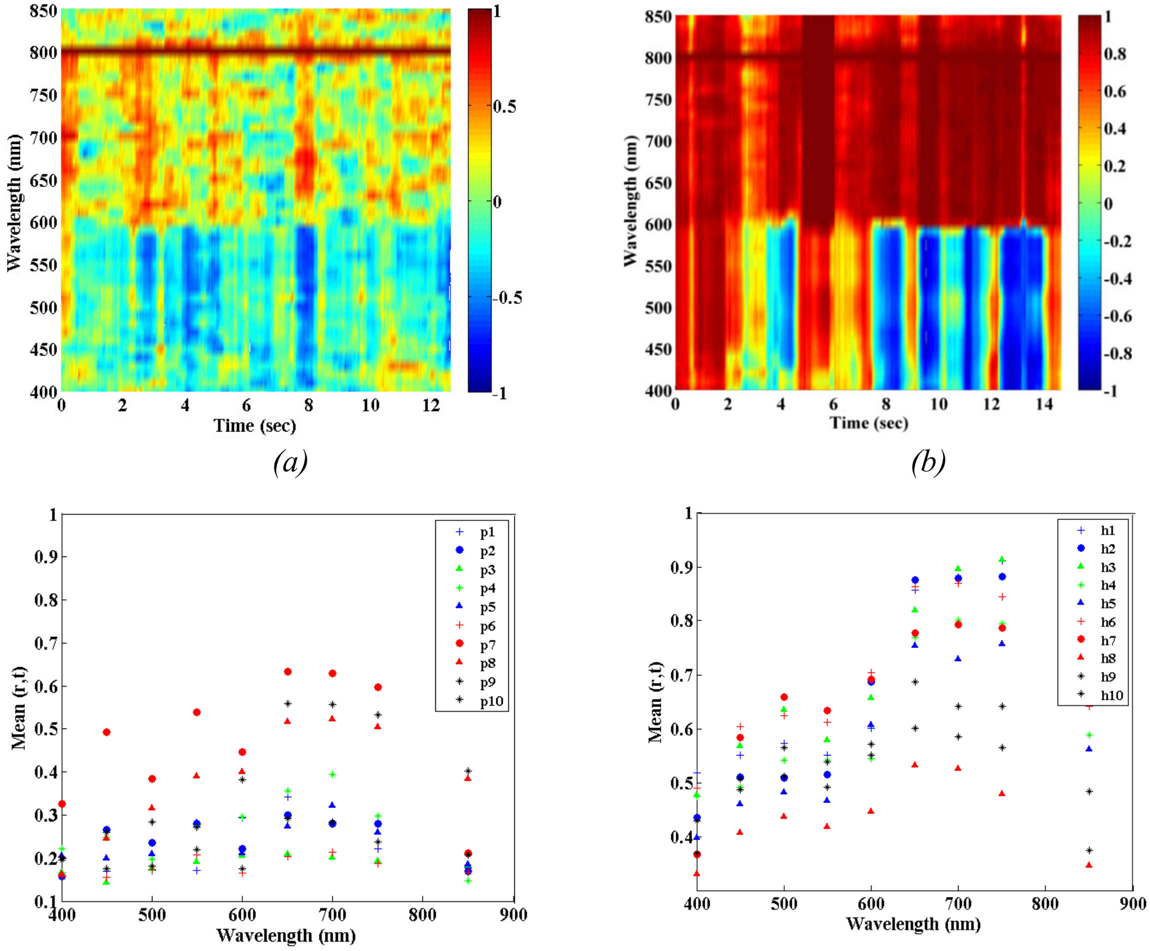

(a) *(b)*

(c) *(d)*

Figure 5.3*: (a) and (b) are the representative correlation coefficient maps,* $r(\lambda_i,\lambda_{ref},t)$*, from the Holder and Hand groups, respectively. (c) and (d) are MEAN(*$r(\lambda_i, \lambda_{ref}, t)$*) calculated using* $Rd_{cal}(\lambda,t)$ *from the Holder and Hand groups, respectively. Figure legends p1 to p10 are sites from Probe Holder group and h1 to h10 are sites from Hand Held group.*

The correlation coefficient maps, $r(\lambda_i,\lambda_{ref},t)$, from the Holder group were featureless, as shown in Figure 5.3a; $r(\lambda_i,\lambda_{ref},t)$ fluctuated randomly between -0.5 and 0.5 along the time axis as well as the wavelength axis. In contrast, $r(\lambda_i,\lambda_{ref},t)$ from the Hand group often possessed vertical bands, where high temporal correlations ($|r| > 0.8$) were found among the majority of wavelength bands. The temporal durations of these vertical bands varied. Moreover, this vertical band may be divided into two segments along the wavelength axis; $r(\lambda_i,\lambda_{ref},t)$ above 600 nm was greater than 0.8 and $r(\lambda_i,\lambda_{ref},t)$ below 600 nm was less than -0.8. Because of these vertical bands, $MEAN(r(\lambda_i, \lambda_{ref}, t))$ from the Hand group was generally higher than that from the Holder group. This difference, according to a two sample t-test and Kolmogorov-Smirnov test (wherever applicable), was statistically significant (Table 5.2). Also, it is noted that the difference in $MEAN(r(\lambda_i, \lambda_{ref}, t))$ between the two data groups was more pronounced between 400 and 600 nm than over the remaining wavelengths.

5.3.3 Frequency Composition

Low temporal variations in $Rd_{cal}(\lambda,t)$ from the Holder group were clearly reflected in their corresponding frequency spectra (Figure 5.4a); they were very similar to the frequency spectrum of spectrometer noise (no light). However, $FT_{abs}\_\lambda_i(f)$ from the Holder group often processed a prominent frequency component between 1 and 2 Hz, which was related to the heart rate of the studied subject. As expected, strong temporal variations in $Rd_{cal}(\lambda,t)$ from the Hand group led to more frequency components in their corresponding $FT_{abs}\_\lambda_i(f)$. These random frequency components, however, were not related to physiological characteristics of the brain (i.e., heart rate and breathing rate). Statistically, $P(\lambda_i)$ from the Holder group was significantly smaller than $P(\lambda_i)$ between 400 and 850 nm (Table 5.2).

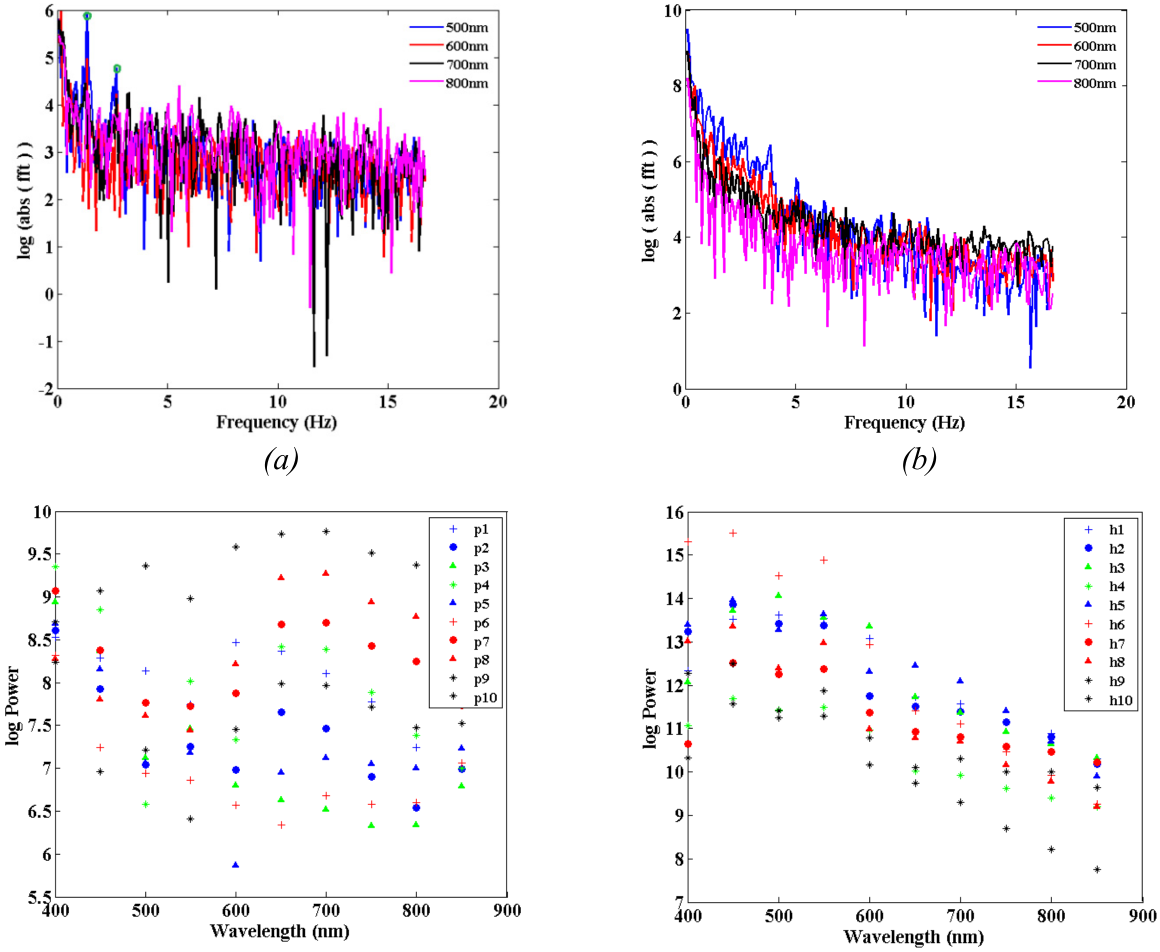

(a) *(b)*

(c) *(d)*

Figure 5.4: *(a) and (b) are the representative $FT_{abs}\_\lambda_i(f)$ from the Holder and Hand groups, respectively The green dots on peaks represent the respiration and heartbeat respectively. (c) and (d) are $P(\lambda_i)$ calculated using $FT_{abs}\_\lambda_i(f)$ from the Holder and Hand groups, respectively. Figure legends p1 to p10 are sites from Probe Holder group and h1 to h10 are sites from Hand Held group.*

Domain	400 nm	450 nm	500 nm	550 nm	600 nm	650 nm	700 nm	750 nm	800 nm	850 nm
$\%STD\_Rd_{cal}(\lambda_i)$	0.003 *	0.001	0.001	0.001	0.001	0.001	0.000 *	0.001	0.000	0.001 *
$MEAN(r(\lambda_i, \lambda_{ref}, t))$	0.000	0.001 *	0.000	0.001 *	0.000	0.000	0.000	0.003 *	-	0.003 *
$P(\lambda_i)$	0.000	0.000	0.000	0.000	0.000	0.000	0.000	0.000	0.000	0.000

Table 5.2: *Results of statistical comparisons (p values) * indicates that a non-parametric test (Kolmogorov-Smirnov) was used.*

5.4. Discussion and Conclusions

In this study, the effects of hand motions on *in vivo* optical investigation were evaluated qualitatively and quantitatively in time and frequency domains. Hand motion induced significantly random variations in acquired diffuse reflectance spectra, and its effects in the short wavelength region (i.e., below 600 nm) are more prominent. These random variations in the time domain translate to a significant increase in the power spectral energy in the frequency domain. These variations can be strong enough to overwhelm the meaningful signals generated by the *in vivo* physiological characteristics of the investigated tissue (e.g., cardiac cycle). Even more interesting is that the temporal correlation of these spectral alterations exhibit peculiar wavelength dependencies: their phases at different wavelength bands may be completely opposite under certain circumstances. The introduction of the probe holder mentioned in this paper significantly reduces these temporal variations in the acquired diffuse reflectance spectra, while preserving the native signals from *in vivo* brain.

Through the frequency domain and temporal correlation analyses of $Rd_{cal}(\lambda,t)$, it was found that oscillations in the diffuse reflectance spectra, acquired using the probe holder, coincide with the rates of the beating heart (1 to 2 Hz) and breathing (0.2 to 0.5 Hz). This indicates that heart beats and breaths alter local hemodynamic characteristics, namely blood volume and hemoglobin oxygenation. These changes, in turn, modify the absorption properties of the cortex and, hence, the measured diffused reflectance signals. Spectral alterations induced by probe movement can be classified into two categories, based upon the nature of the movement. For lateral probe movements, the spectral alterations originate from spatial variations in the optical properties of the cerebral cortex. This commonly appears as synchronized oscillations in diffuse reflectance signals at all wavelengths, and explains the high-correlation-coefficient vertical bands in the correlation coefficient maps $r(\lambda_i,\lambda_{ref},t)$. *For* axial probe movement, the spectral alterations are induced primarily by the changes in the regional hemodynamics [142]. The changes in hemoglobin oxygenation would lead to wavelength dependent increase/decrease in $Rd_{cal}(\lambda,t)$, and hence the band characteristics in its corresponding correlation coefficient maps $r(\lambda_i,\lambda_{ref},t)$. The deformation of the cortex induced by axial probe movement, however, should not change its scattering properties because the biological tissue has been treated as an incompressible material in studies of tissue mechanical properties.

The potential to utilize signal processing techniques to remove motion artifacts from recorded signals like $Rd(\lambda,t)$ have been explored by various groups, including ours. Because of the nonlinear and unpredictable nature of the motion artifacts, conventional frequency domain filtering would not provide satisfactory results. Consequently, nonlinear filters - such as adaptive filtering, wavelet filtering, and independent component analysis - must be used. Based on our experience thus far, none of the existing filtering techniques effectively removes the motion artifacts in $Rd(\lambda,t)$. This is because of the nonlinear effects of motion artifacts on diffuse reflectance signals at various wavelengths. Therefore, we believe that it is better to reduce the effects of motion artifacts during the recording stage (using a mechanical holder).

Attempts to stabilize the optical probe during *in vivo* spectral acquisition procedures have been made by several groups, where a plain mechanical structure, like a pincer, was used [142, 155, 156]. Such an approach would eliminate the lateral and axial movements of the optical probe induced by the hand, but might not address the irregular probe contact issue induced by the spontaneous movements of the *in vivo* tissue. Based on our experience, *in vivo* brain movements in a surgical environment are significant, because of cardiac cycle and ventilation under anesthesia. A plane mechanical holder would yield inconsistent probe contact pressure. Due to the softness of the brain, inconsistent probe contact pressures lead to detrimental tissue deformation and, thereby, regional alterations in hemodynamics [142]. The probe holder design proposed and tested in this paper took this concern into consideration; the springs in the probe holder reduce contact pressure significantly when the probe is placed lightly in contact with the brain surface. In addition, it reduces the amount of force (and, hence, the degree of brain deformation) required to move the probe along its primary axis. In other words, the probe will move according to brain surface movement, without drastically changing probe contact pressure. This improvement consequently reduces motion artifacts in the optical data.

Optical Spectroscopy is being applied increasingly for differentiating various healthy body tissues from unhealthy ones. Technological and theoretical advances make it easier to apply it to the study of brain tissue. However, if attention is not paid to sources of signal variations, researchers risk drawing the wrong conclusions from their data. This is especially true for time-dependent recordings. In this study the characteristics of the motion artifacts induced by an operator's hand when holding an optical probe, as well as the spontaneous movements of brain tissue were quantitatively demonstrated. Moreover, a new probe holder design that can contain motion artifacts to a great extent was introduced; hence, small time-dependent variations in diffuse reflectance spectra associated with the intrinsic characteristics of the brain can be captured.

6. Interictal Characteristics of Epileptic Cortex Measured by Dynamic Diffuse Reflectance Spectroscopy

6.1. Introduction

Epilepsy surgery is performed for the purpose of freeing children from intractable epilepsy and hence adverse effects of recurrent seizures. Detection of epileptic cortex can be achieved via studying/observing its abnormal pathophysiological characteristics. One major feature widely used in current practice is the electrophysiological characteristics of the epileptic cortex: abnormal electrical discharges during the ictal and interictal periods can be captured and localized using EEG and ECoG [157, 158]. The structural abnormality induced by epilepsy may be detected by MRI/CT noninvasively and by optical spectroscopy intraoperatively (see Chapter 3). Several imaging studies have also shown that epileptic cortex and its surrounding tissue are hypometabolic between seizures [159], and become hypermetabolic when seizure occurs [160]. The alterations in the metabolic state of the epileptic cortex may directly or indirectly affect the regional hemodynamics [75, 161]; non-invasive imaging studies [160] and intraoperative intrinsic optical signal (IOS) measurements [73] from human subjects show a transient increase in regional blood flow, cerebral blood volume, and hemoglobin oxygenation when seizure occurs. Nevertheless, the hemodynamic characteristics of epileptic cortex during the interictal period have not yet been investigated. Here, the dynamic diffuse reflectance spectroscopy developed in the previous chapter was used to measure the interictal hemodynamic characteristics of pediatric epileptic cortex *in vivo*. The results of the study reveals that the epileptic cortex possesses unique temporal hemodynamic characteristics, which may be used localize and demarcate epileptic cortex intraoperatively.

6.2. Materials & Methods

The details of the instrumentation used in this study, time dependent diffuse reflectance spectroscopy system, can be found in the previous chapter and hence not repeated here. It was used to directly acquire diffuse reflectance spectra in the visible wavelength region (i.e., 400 to 850 nm) as a function of time. For each patient studied, the optical investigation was performed prior to lesion removal and the investigated tissue sites were selected by the surgeons. At least four distinct sites were investigated in a single patient study.

Prior to the spectral acquisition, each investigated site was rinsed with saline to remove surface blood. The light source was turned on at least 30 seconds prior to the data acquisition to allow its output to stabilize. With the probe placed gently in direct contact with the cortical surface, diffuse reflection spectra Rd(λ,t) were recorded continuously for about 12 seconds at a 33 Hz rate. A biopsy was taken from each investigated site, except of those classified as normal/functional cortical surface (i.e., outside the resection zone). All biopsies acquired were processed using the conventional tissue processing/sectioning routine and then stained using hematoxylin and eosin. The stained tissue sections were then read by a neuropathologist to identify those histopathological abnormalities associated with epileptic cortex. Every stage of the study protocol was carried out under the careful supervision of the surgeons such that the patient care was not compromised.

It has been shown that the cortex outside the zone of resection, defined by intraoperative ECoG, do not necessary represent the true normal cortex. Therefore, pediatric brain tumor patients undergoing brain tumor surgery were recruited in this study for the purpose of establishing the normal baseline. The measurement procedure used in the tumor patient study was identical to that described above. The sites of investigation were selected from the cortex outside the zone of resection defined by the pre-surgical imaging studies.

Prior to the data analysis, all recorded Rd(λ,t)s were calibrated to remove the artifacts induced by instrumentation, which yielded $Rd_{cal}(\lambda,t)$. The mechanical probe holder disclosed in Chapter 5 was not used in this study because it was not readily available at the beginning of this study. Therefore, $Rd_{cal}(\lambda,t)$ shown here inevitably contained a certain level of motional artifacts originated from the movement of surgeon's hand. According to results of several *in vitro* studies regarding hand-motion artifacts (not published), it was found that motion artifacts often exhibit statistically high covariance among all optical wavelengths in $Rd_{cal}(\lambda,t)$. This unique characteristic led to the development of a new signal process routine for removal of this type of motion artifacts using principal component analysis (PCA) [162]. PCA (or truncated singular value decomposition) filtering is based on the subtraction of the eigenvector components exhibiting high covariance (i.e., motion artifacts) in the data. The principal components of the data covariance were calculated using a standard procedure for singular value decomposition (SVD). Specifically, $Rd_{cal}(\lambda,t)$ is a m×n rectangular matrix and can be rewritten in the following form:

$$Rd_{cal}(\lambda,t) = u_1 s_1 v_1^T + u_2 s_2 v_2^T + \dots + u_n s_n v_n^T \tag{6.1}$$

where $s_1 \geq s_2 \geq \dots \geq s_n \geq 0$, U is an m×n orthogonal matrix, S is a n×n diagonal matrix, V is another n×n orthogonal matrix. Since motion artifacts will typically have a highly covariant structure, they are generally captured in the first few (strongest) eigenvector components. Therefore, they may be removed by subtracting first n_a of $u_n s_n v_n^T$ from $Rd_{cal}(\lambda,t)$. That is

$$Rd_{true}(\lambda,t) = Rd_{cal}(\lambda,t) - \sum_{i=1}^{n_a} u_i s_i v_i \tag{6.2}$$

To analyze the time-varying characteristics of $Rd_{true}(\lambda,t)$, correlation coefficient (CC) analysis was used. CC analysis was performed between a reference signal, $Rd_{true}(\lambda_{ref},t)$, and a comparison signal, $Rd_{true}(\lambda_{comp},t)$. This calculation yielded $\gamma(\lambda_{ref},\lambda_{comp},t)$ representing the temporal correlation between the two diffuse reflectance signals. Here the reference signal $Rd_{true}(\lambda_{ref},t)$ was chosen at $\lambda_{ref} = 800$ nm because it is not influenced by hemodynamics (i.e., absorption) as much as those in the visible wavelength region and is more sensitive to the structural characteristics (i.e., scattering) of the investigated tissue. The window size for CC calculation was 25, which was short enough to capture the transient temporal variations in $Rd_{true}(\lambda_{comp}, t)$ and, at the same time, long enough to reduce the effects of the random spectrometer noises to the analysis. The comparisons of $\gamma(\lambda_{ref}, \lambda_{comp}, t)$ between epileptic cortex (defined by ECoG) and normal cortex were carried out using empirical methods.

To uncover the underlying mechanisms of the unique features in $\gamma(\lambda_{ref}, \lambda_{comp}, t)$, a Monte Carlo simulation for photon migration (see Chapter 4) was used to stimulate $Rd(\lambda,t)$ with varying blood volume factor (BVF) and oxygen saturation ($SatO_2$). The alterations in BVF and $SatO_2$ directly affected the absorption coefficient $\mu_a(\lambda)$ [1/cm] of the biological medium. That is

$$\mu_a(\lambda) = BVF[SatO_2 \times \mu_a^{HbO_2}(\lambda) + (1 - SatO_2) \times \mu_a^{Hb}(\lambda)] \tag{6.3}$$

where $\mu_a^{HbO_2}(\lambda)$ is the absorption coefficient of oxygenated blood [1/cm] and $\mu_a^{Hb}(\lambda)$ is the absorption coefficient of deoxygenated blood [1/cm]. The simulated $Rd(\lambda,t)$s were analyzed using the correlation analysis method described above to produce $\gamma_{sim}(\lambda_{ref}, \lambda_{comp}, t)$, which were then compared with those from the *in vivo* studies to determine the contribution of temporal variations in hemodynamics to the variations in $\gamma(\lambda_{ref}, \lambda_{comp}, t)$.

6.3. Results and Discussion

In this study 19 tumor patients and 26 epilepsy patients were enrolled. The demographic information of these patients can be found in Table 6.1. A total of 41 sets of Rd(λ,t)s were acquired from the tumor patients, which forms the *tumor normal group*. A total of 137 sets Rd(λ,t)s were obtained from the epilepsy patients: 88 sets were from the cortex within the zone of resection (*epileptic abnormal group*) and 49 sets from the cortex outside the zone of resection (*epileptic normal group*).

Figure 6.1 shows a representative result from the CC analysis of Rd(λ,t) from the tumor normal group. Obviously the hand movement of the surgeon introduced significant temporal variations in Rd(λ,t) at all wavelengths. $\gamma(\lambda_{ref} = 800$ nm, λ_{comp},t) calculated using the data without PCA filtering shows that high temporal correlation was found at all wavelengths during the entire recording duration. This suggests that the spectral artifacts induced by hand motion, in this case, are not highly wavelength dependent. When PCA filtering is applied to the Rd(λ,t), significant changes in $\gamma(\lambda_{ref} = 800$ nm, λ_{comp},t) are observed. When the first and second PCs are removed from Rd(λ,t), $\gamma(\lambda_{ref} = 800$ nm, λ_{comp},t) shows an interesting two-horizontal band characteristics: $\gamma(\lambda_{ref} = 800$ nm, λ_{comp},t) above $\lambda_{comp} = 600$ nm shows a strong positive correlation (i.e., $\gamma > 0.8$) and $\gamma(\lambda_{ref} = 800$ nm, λ_{comp},t) below $\lambda_{comp} = 600$ nm shows a strong negative correlation (i.e., $\gamma > - 0.8$). Removing more PCs from the raw data does not change the two-band characteristic in $\gamma(\lambda_{ref} = 800$ nm, λ_{comp},t) until the total number of PCs removed exceeds 50, where $\gamma(\lambda_{ref} = 800$ nm, λ_{comp},t) becomes completely random and its values vary approximately between -0.3 to +0.3. The above mentioned trend in $\gamma(\lambda_{ref} = 800$ nm, λ_{comp},t), resulting from PCA filtering, is found to be very common among the data sets from the tumor normal group (Table 6.2). However, the number of PCs that have to be removed in order to reveal the two band characteristics in $\gamma(\lambda_{ref}= 800$ nm, λ_{comp},t) is site dependent. This may be explained by the level of motion artifacts as well as their spectral and temporal characteristics in the original data.

CC analysis reveals many unique wavelength-dependent temporal variations in Rd(λ,t) from the epileptic cortex group (ECoG defined). One of the representative results from the CC analysis of Rd(λ,t) from the epileptic cortex group (ECoG defined) is shown in Figure 6.2. Again prior to PCA filter, Rd(λ,t) contains a certain level of motion artifacts and its $\gamma(\lambda_{ref}= 800$ nm, λ_{comp},t) shows several high-correlation (> 0.8) vertical bands during the recording period. When first three or four PC's are removed from Rd(λ,t), $\gamma(\lambda_{ref}= 800$ nm, λ_{comp},t), it shows an interesting four-horizontal band characteristics: a strong positive correlation (i.e., $\gamma > 0.8$) is found between 600 nm and 800 nm and a strong negative correlation (i.e., $\gamma > - 0.8$) between 400 nm and 450 nm. Filtered Rd(λ,t)s between 450 nm and 500 nm show positive temporal correlation with the reference signal, while Rd(λ,t)s between 500 nm and 600 nm show negative temporal correlation with the reference signal. Removing more than 15 PCs from the raw data makes $\gamma(\lambda_{ref}= 800$ nm, λ_{comp},t) completely random and its values vary approximately between -0.3 to +0.3. Within the data set from epileptic cortex, neither a predictable alteration trend in $\gamma(\lambda_{ref}= 800$ nm, λ_{comp},t) nor a two-band characteristic observed in the tumor normal group, resulting from PCA filtering, could be observed consistently (Figure 6.3 and Table 6.3). This suggests the two-band characteristic in $\gamma(\lambda_{ref}= 800$ nm, λ_{comp},t) may be unique to the normal cortex.

Date	Age & Sex	Number of Sites	Date	Age & Sex	Number of Sites
Tumor Normal			**Epilepsy Abnormal**		
090507	9F	2	050107	17M	5
091707	10M	2	050207	3M	3
092107	5F	2	060407	14M	2
040108	6F	2	060607	8M	2
040308	9F	2	061807a	15F	2
051408	8F	3	062607	15F	3
061308	5F	2	121207		4
082808	6F	2	012907	15F	3
112108	3F	2	021207	8M	1
120508	14F	3	022707	2M	5
121208	10F	2	022807	2M	3
022509	2F	2	031907	12M	2
022607	13F	2	091907	7M	3
051507	9F	2	100307	3F	8
060507	6M	2	100407	15F	2
061207	12F	2	101107	15F	3
061807	10M	1	102307	2M	3
062707	11F	4	102407	10F	3
080707	1M	2	110507	7F	3
110607	4M	5	073107	13F	4
062607	15F	3	081407	18M	2
062907	9M	2	081507	10M	5
072407	6M	2	082707	12F	4
072507	18F	2			

***Table 6.1**: Demographic information of the epilepsy and tumor patients recruited in the study presented.*

Case	Site	PC Removed	Variance Reduced	Single Band	Double Band	Multiple Band	No Band
090507	1	10	98.83%			Y	
	2	4	96.11%	Y			
091707	3	1	95.29%		Y		
	4	1	88%		Y		
092107	4	4~10	96~98%			Y	
	5	X	X			Y	
040108	1	4~10	96~78%		Y		
	2	3~4	90~93%		Y		
040308	1	1	93.59%		Y		
*No strong motion artifacts	2	X	X		Y		
051408	1	1,2,3,4	88.89%		Y		
	2	X	X	Y			
	3	1~10	99.90%		Y		
061308	1	12	98.90%		Y		
	2	2	99.37%		Y		
082808	1	10	99.39%	Y			
	2	1~10	99.49%		Y		
112108 * PCA Filtering is not very helpful	1	X	X		Y		
	3	10	97.76%		Y		
120508	1	4	98.35%		Y		
	2	15	99.79%		Y		
	3	15	99.79%		Y		
121208	1	10	99.32%		Y		
	4	2	94.88%		Y		
022509	1	25	99.85%		Y		
	3	2~10	99.89%		Y		
022607	1	2	93%		Y		
	2	4~10	91~97%		Y		
051507	1	10	96.50%		Y		
	2	10~15	90~94%		Y		
060507	1	15	95%		Y		
	2	15	96%		Y		
061207	1	15	93%		Y		
	2	15	98%	Y			
061807	2	X		Y			
062707	1	1,2,3	98%		Y		

	2	2,3	53~66%		Y		
	3	3,4	89~90%		Y		
	4	4~10	98-99%		Y		
080707	1	10	99.29%		Y		
	2	0	0%		Y		

Table 6.2*: PCA filtering and band characteristics for the data sets from the tumor normal group.*

Date	**Site**	**PC Removed**	**Single Band**	**Double Band**	**Multiple Band**	**No Band**	**Pathology**
050107 * Band cutoff is 500 nm	4	10~15		Y*			N/A
	5	25		Y			N/A
	7	1~2		Y			N/A
	8	10		Y			Normal
	9	10		Y			Normal
050207	2	X			Y		Normal
	3	1,2		Y			Normal
	5	25		Y			Normal
060407 * PCA Filtering is not helpful	4	X				Y	Abnormal
	5	X				Y	Abnormal
060607	5	1~4				Y	Abnormal
		10		Y			
	6	1		Y			Abnormal
061807a	1	2~10				Y	N/A
	2	2~10			Y		N/A
		15		Y			
062607	2	0~3	Y				Abnormal
		4~15				Y	
	3	1~3				Y	Normal
		4~15			Y		
121207	1	0~4			Y		Normal
		10				Y	
	2	2			Y		Normal
	5	2~3				Y	Abnormal
	7	4		Y			Abnormal
		10~15			Y		
012907	1	2~3		Y			Normal
* With 2 additional weak bands	2	10~15		Y			Normal
	4	10~15		Y			Abnormal
021207	1	0				Y	Normal
022707	1	1		Y			Abnormal
* Noisy	2	1		Y			Normal
	3	25		Y			Normal
	4	4		Y			Abnormal
	5	1~2		Y			Normal

		3			Y		
022807	1	2		Y			Normal
	2	3		Y			Abnormal
* 3rd and 4th bands are weak	3	10~15			Y		Normal
031907	3	X				Y	Normal
	4	3~10			Y		Abnormal
091907	1	2				Y	Normal
	2	1		Y			Normal
	6	1		Y			Abnormal
100307	1	1		Y			N/A
	2	4~10		Y			Abnormal
*Cutoff at 700 nm	3	1~2		Y*			N/A
		10~25			Y		
	4	0~15				Y	N/A
		25			Y		
	5	10		Y			N/A
	9	10		Y			Abnormal
	10	10~15		Y			Abnormal
	12					Y	Abnormal
100407	1	10~15				Y	N/A
	2	1~15	Y				N/A
101107	1	X				Y	Abnormal
	2	15		Y			Abnormal
	3	X				Y	Abnormal
102307	1	10			Y		Normal
	2	15		Y			Abnormal
	3	10		Y			Abnormal
		15			Y		
102407	2	2		Y			Normal
		4~25			Y		
	3	3		Y			Normal
		4~25			Y		
	5	10			Y		Abnormal
110507	1	10		Y			Normal
	3	1		Y			Normal
	4	0~4				Y	N/A
110607	1	X				Y	Abnormal
	2	15~25		Y			Abnormal
	3	10~15			Y		N/A
	4	1~15	Y				N/A

	5	1~15	Y				N/A
062607 *Weak 2-band	2	25		Y*			Normal
	3	10~15			Y		Abnormal
* Cutoff at 650 nm	6	1		Y*			Abnormal
062907	1	0~4				Y	Abnormal
		10~15		Y			
	2	0~10	Y				Normal
		15		Y			
072407	3	1~2		Y			Normal
	4	X				Y	Normal
072507	1	1~2		Y			Normal
	2	1		Y			Normal
		3~15			Y		
073107	1	1~2		Y			Normal
		3~15			Y		
	2	1~4	Y				Abnormal
		10~25			Y		
	4	15		Y			N/A
	5	4		Y			Abnormal
081407	3	X				Y	Normal
	4	10~15				Y	Normal
081507	2	10~15			Y		Abnormal
	3	15~25		Y			Normal
	4	2		Y			Normal
	6	2~4			Y		Normal
	7	0			Y		Normal
082707 * Cutoff at 700 nm	1	0		Y*			N/A
	2	2		Y			N/A
		15			Y		
	3	1		Y			N/A
	5	1		Y			Abnormal

Table 6.3*: Pathology, PCA filtering and band characteristics for the data sets from the epilepsy abnormal group.*

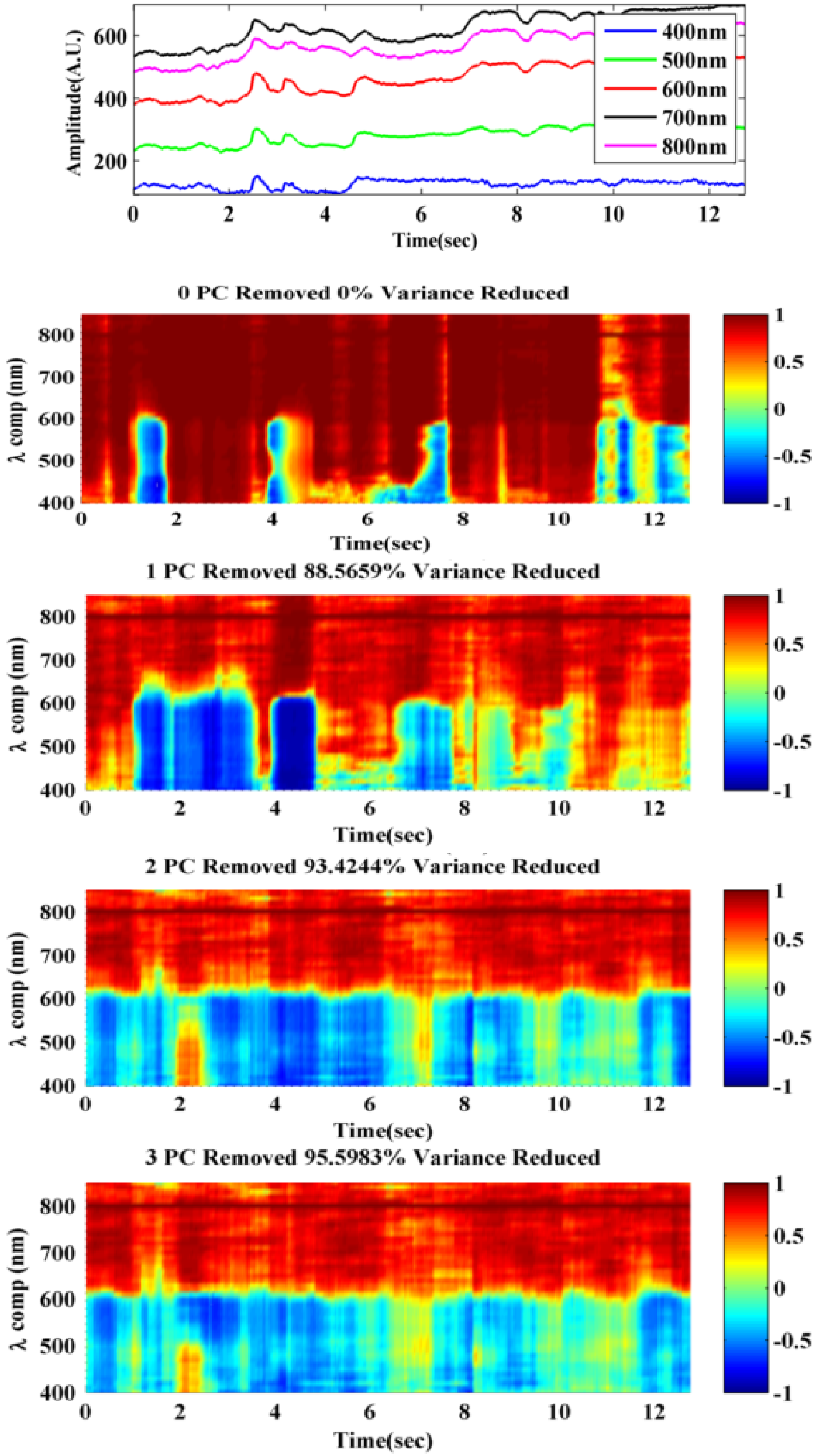

0 PC Removed 0% Variance Reduced

1 PC Removed 88.5659% Variance Reduced

2 PC Removed 93.4244% Variance Reduced

3 PC Removed 95.5983% Variance Reduced

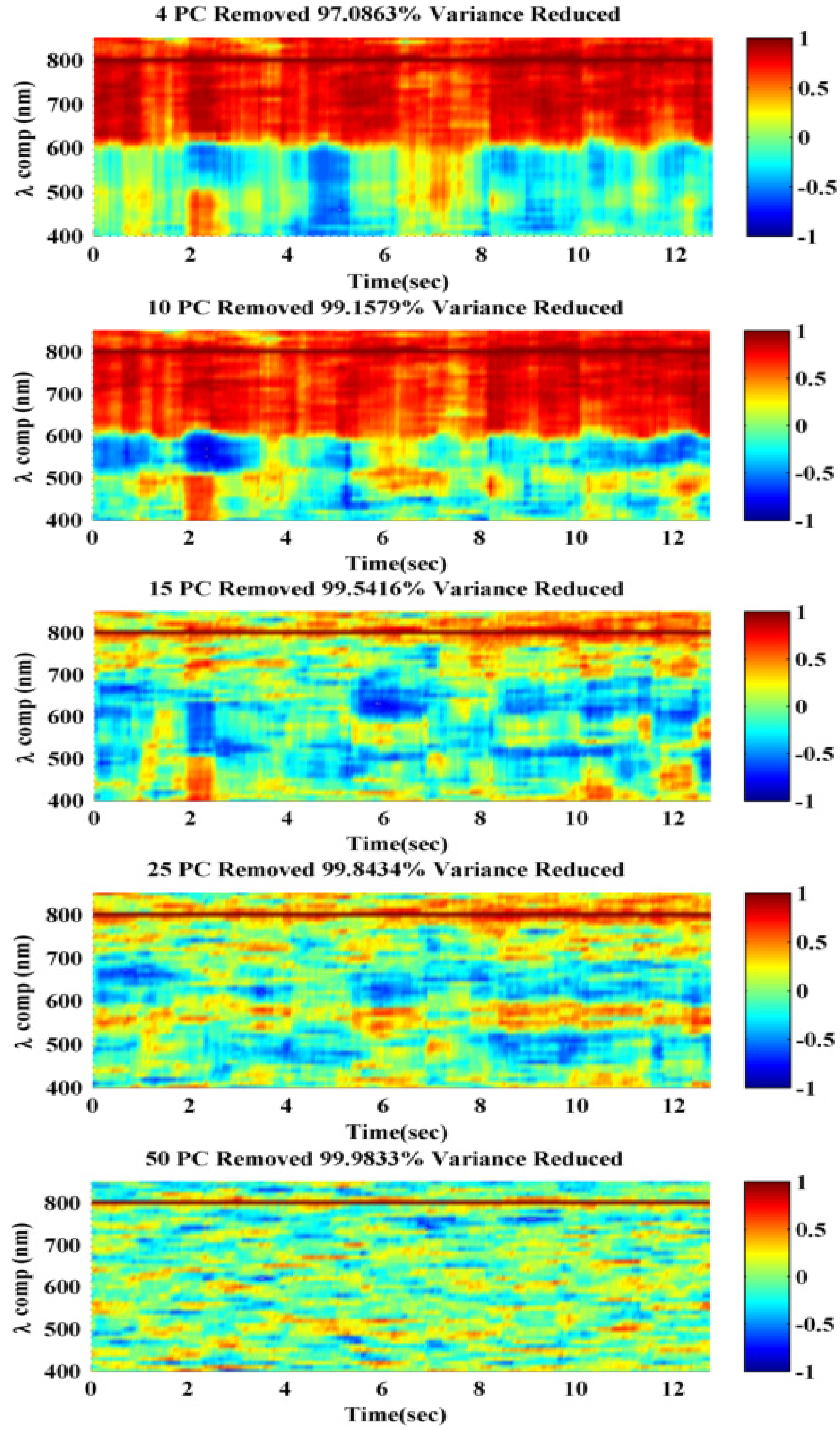

4 PC Removed 97.0863% Variance Reduced

10 PC Removed 99.1579% Variance Reduced

15 PC Removed 99.5416% Variance Reduced

25 PC Removed 99.8434% Variance Reduced

50 PC Removed 99.9833% Variance Reduced

Figure 6.1: *CC analysis of Rd(λ,t) from Site 1 of from Patient 022607 (normal cortex).*

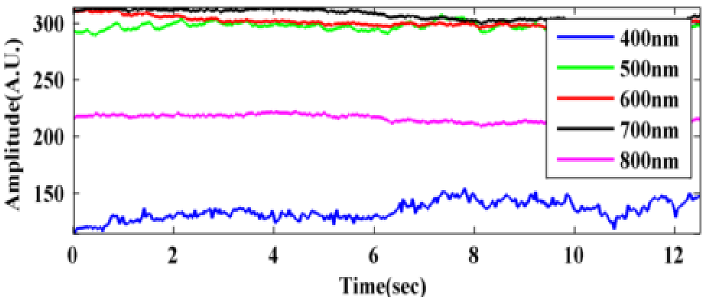

0 PC Removed 0% Variance Reduced

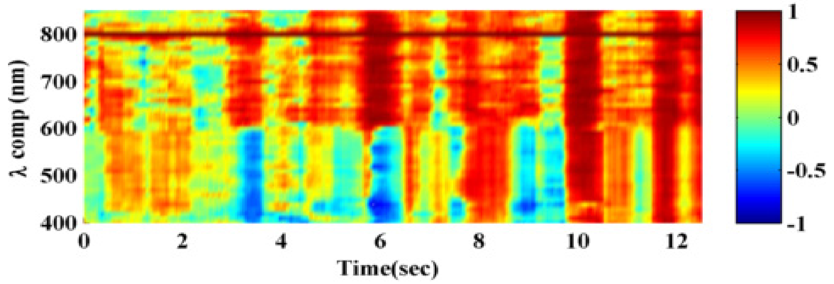

1 PC Removed 34.8684% Variance Reduced

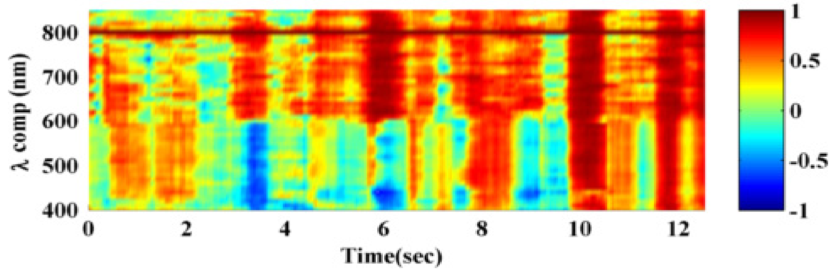

2 PC Removed 51.1913% Variance Reduced

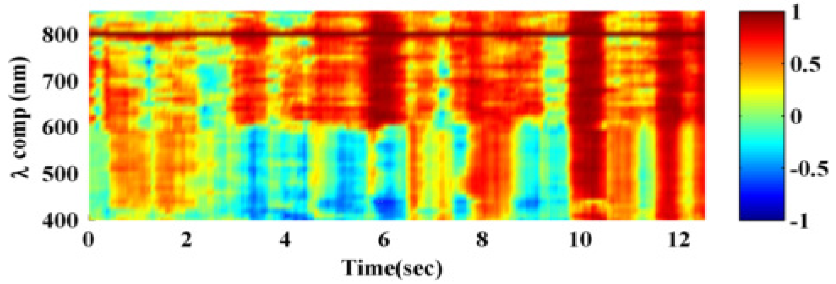

3 PC Removed 63.1193% Variance Reduced

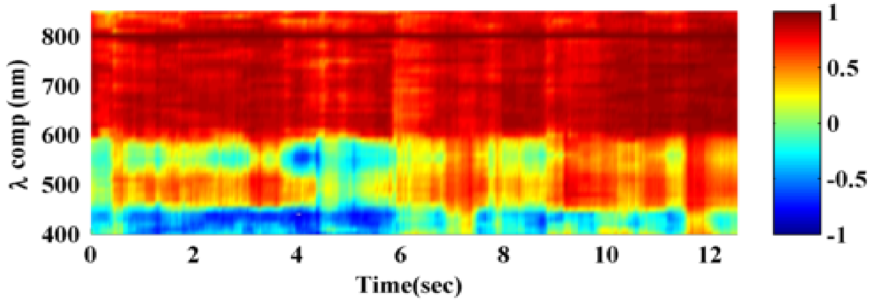

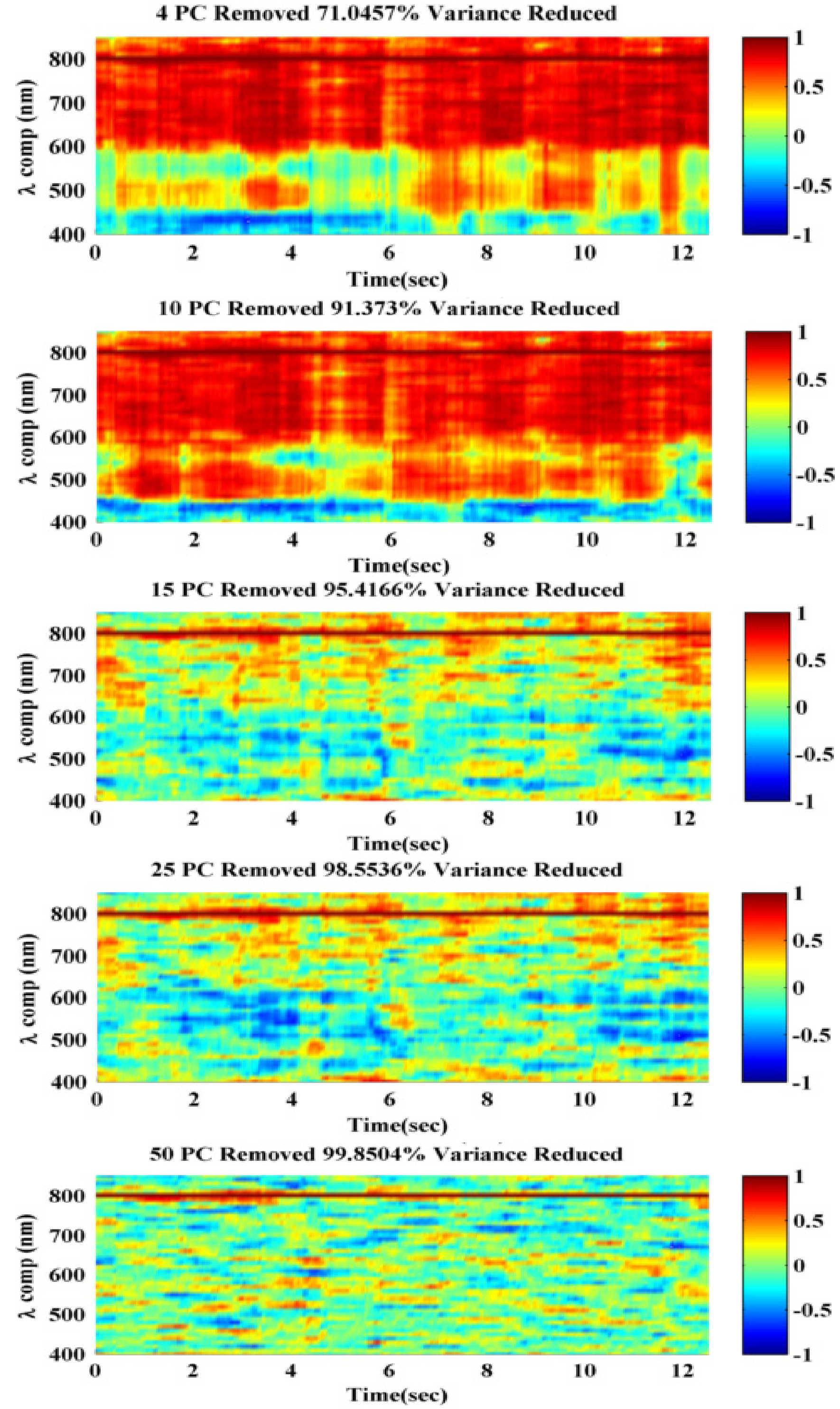
4 PC Removed 71.0457% Variance Reduced

10 PC Removed 91.373% Variance Reduced

15 PC Removed 95.4166% Variance Reduced

25 PC Removed 98.5536% Variance Reduced

50 PC Removed 99.8504% Variance Reduced

Figure 6.2*: CC analysis of Rd(λ,t) from Site 1 of Patient 121207 (epileptic cortex).*

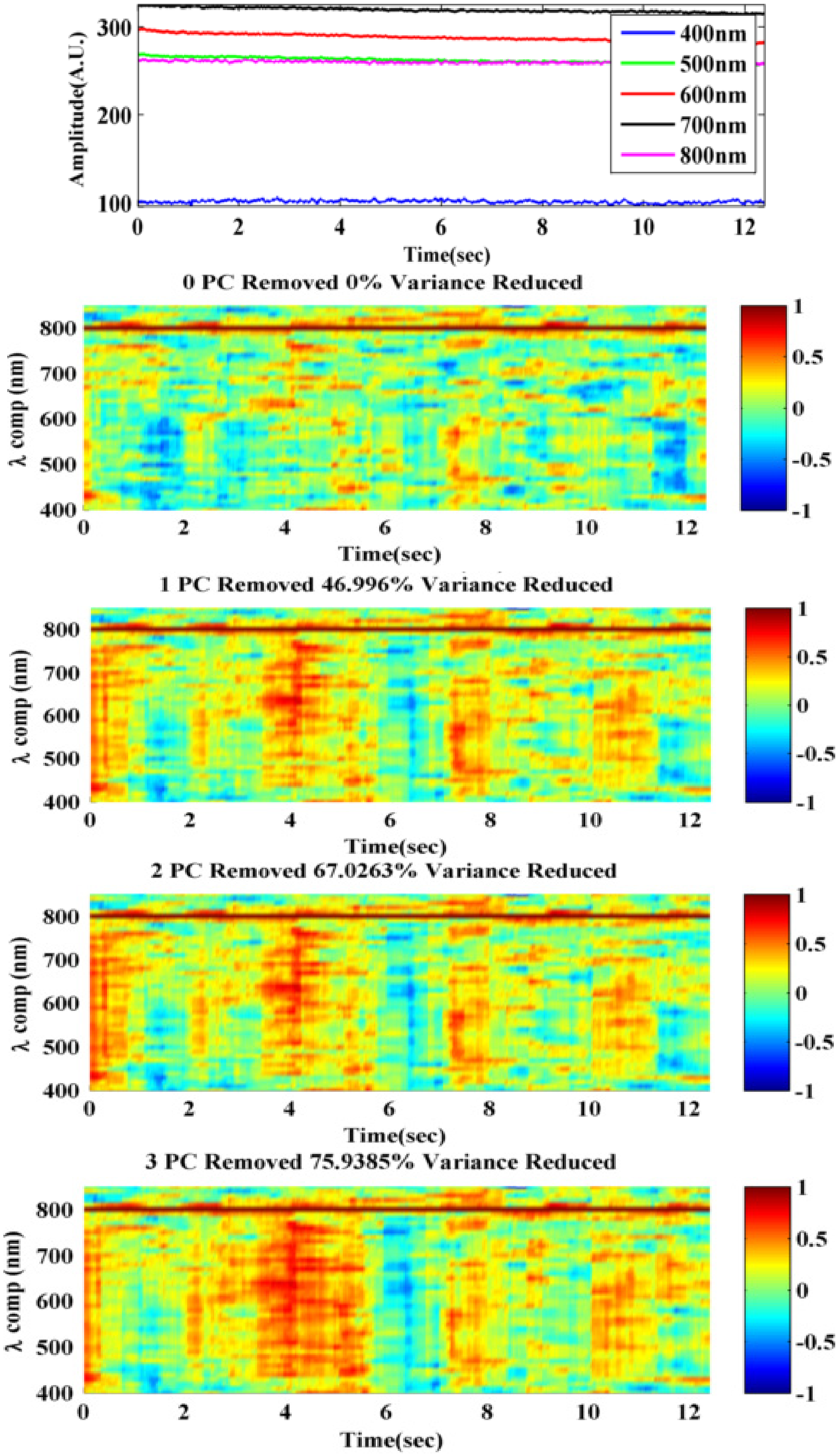
Amplitude(A.U.)
300
200
100
400nm
500nm
600nm
700nm
800nm
0
2
4
6
8
10
12
Time(sec)
0 PC Removed 0% Variance Reduced
1 PC Removed 46.996% Variance Reduced
2 PC Removed 67.0263% Variance Reduced
3 PC Removed 75.9385% Variance Reduced
λ comp (nm)
800
700
600
500
400
1
0.5
0
-0.5
-1

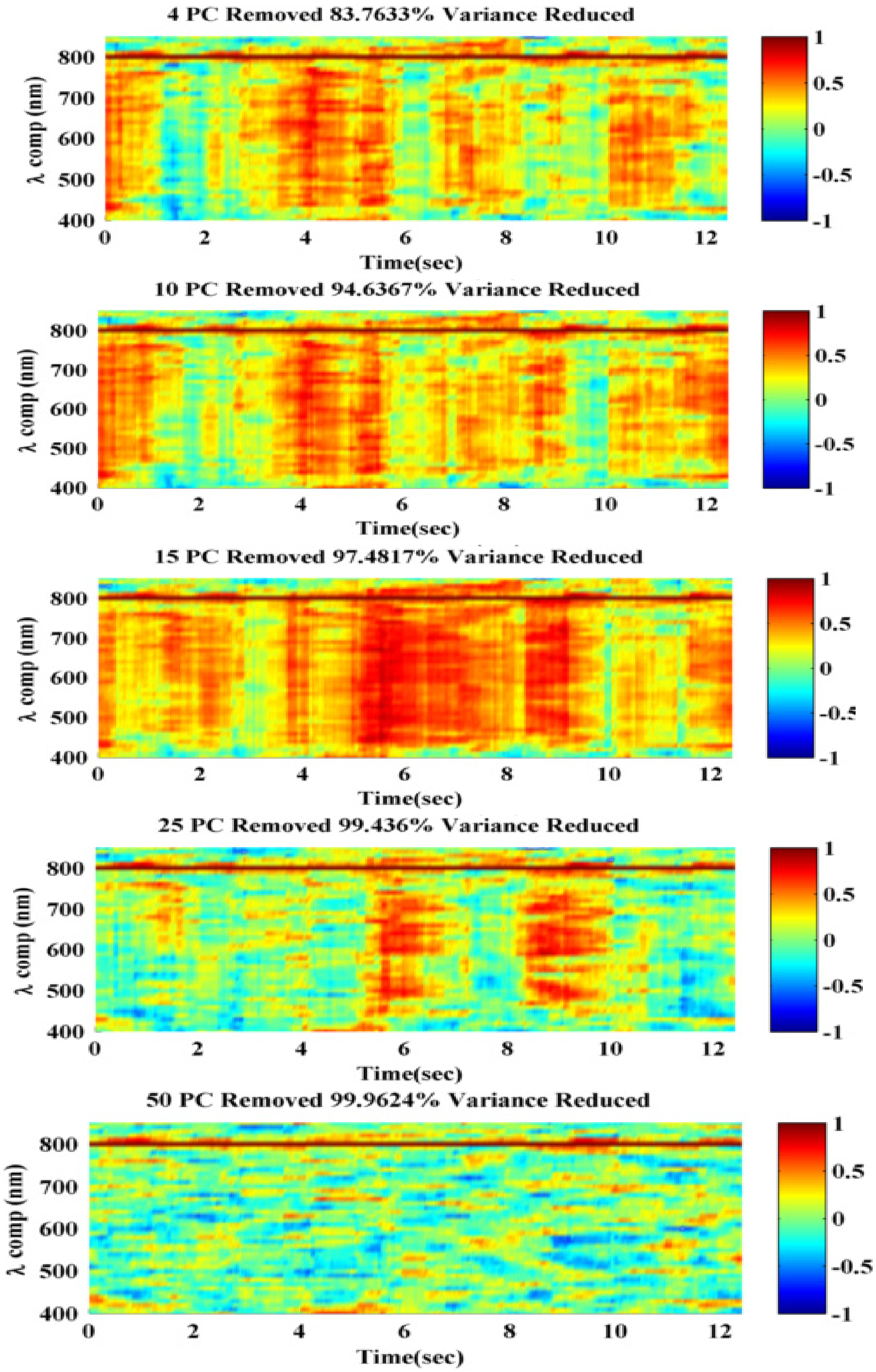

***Figure 6.3**: CC analysis of Rd(λ,t) from Site 1 of Patient 091907 (epileptic cortex). The motion artifact is minimal in this set of data; PCA filtering does not change* $\gamma(\lambda_{ref} = 800\ \text{nm}, \lambda_{comp}, t)$.

Using the simulated Rd(λ,t) generated by the Monte Carlo simulation for photon migration, insights about the underlying physiological mechanisms of the band characteristics in

$\gamma(\lambda_{ref} = 800$ nm, λ_{comp},t). When blood volume oscillates and SatO$_2$ remains constant, as shown in Figure 6.4, the entire $\gamma(\lambda_{ref} = 800$ nm, λ_{comp},t) displays high temporal correlation ($\gamma = 1$). When blood volume remains constant and SatO$_2$ oscillates, horizontal band characteristics appear in the corresponding $\gamma(\lambda_{ref} = 800$ nm, λ_{comp},t). However, these multi-band features were not observed in any of the *in vivo* data recorded. Since the increase in blood volume would also lead to an increase in the scattering property (i.e., increase in the number of red blood cells), a separate simulation was carried out using oscillating BVF and the scattering coefficient and the two-band characteristic, as shown in Figure 6.1, was recreated in the corresponding $\gamma(\lambda_{ref} = 800$ nm, λ_{comp},t). This attests to the physiological origin of the band characteristics in $\gamma(\lambda_{ref} = 800$ nm, λ_{comp},t) from the *in vivo* cortex.

The results of this study also show the effectiveness of PCA filtering in removing spectral artifacts in Rd(λ,t) induced by hand motion. When the motion spectral artifacts are synchronized temporarily at all wavelengths and much stronger than the actual biological signals, they usually occupy the first few principal components and hence can be easily removed using PCA filtering. Since the magnitude of the motion artifacts does vary from case to case, it is rather difficult to predetermine how many PCs should be removed in order to minimize the effects of motion artifacts. It is suggested here that sufficient PCs should be removed in order to eliminate most of the vertical bands while preserving the horizontal bands. When too many PCs are removed from the original signals, $\gamma(\lambda_{ref} = 800$ nm, λ_{comp},t) will represent the correlation of the noise and hence be completely random.

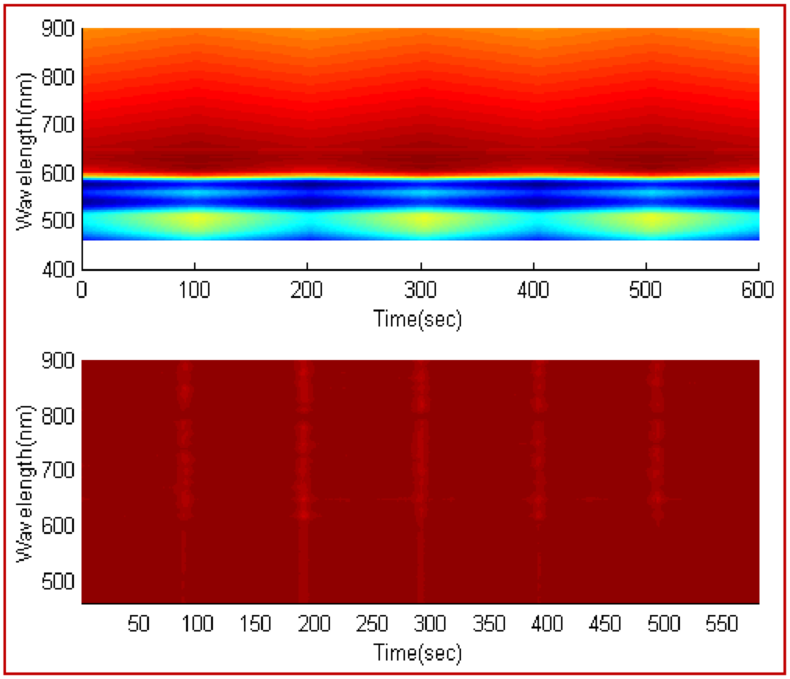

Figure 6.4: *$\gamma(\lambda_{ref} = 800$ nm, $\lambda_{comp}, t)$ (bottom) calculated from simulated $Rd(\lambda, t)$ (top). Here BVF is oscillated between 5% and 3% periodically; and $SatO_2$ is fixed at 3%.*

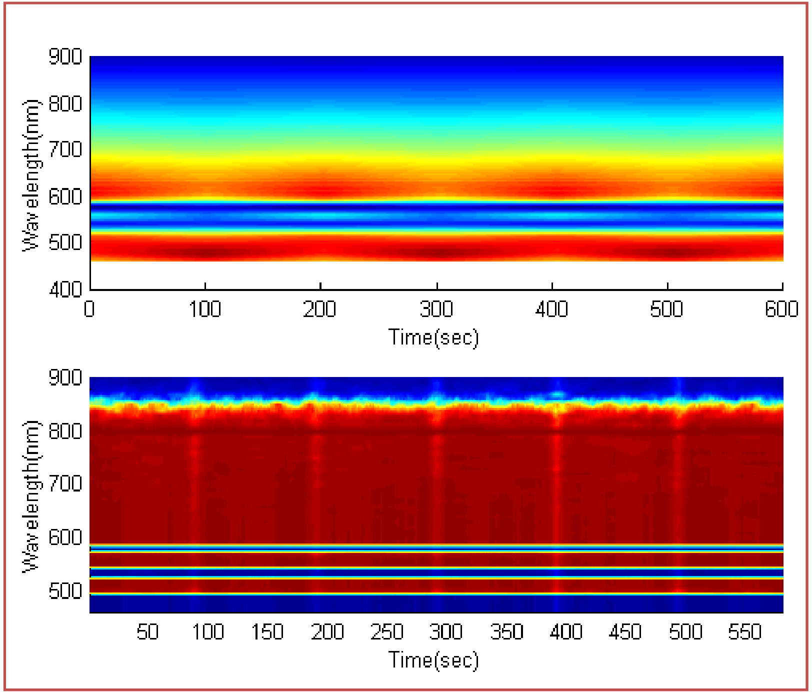

Figure 6.5: *$\gamma(\lambda_{ref} = 800$ nm, $\lambda_{comp}, t)$ (bottom) calculated from simulated $Rd(\lambda, t)$ (top). Here BVF is fixed at 3%; and $SatO_2$ is oscillated between 100% and 60% periodically.*

6.4. Conclusions

Time dependent physiological properties of pediatric epileptic cortex were characterized during the interictal period using dynamic diffuse reflectance spectroscopy. The recorded spectral data were calibrated and conditioned using the PCA filtering method; their temporal characteristics were analyzed using the correlation analysis. The results of the analysis reveal some unique wavelength dependent temporal characteristics of epileptic cortex (i.e., multiple horizontal bands in the correlation coefficient map $\gamma(\lambda_{ref} = 800 \text{ nm}, \lambda_{comp}, t)$). According to the simulation model, these characteristics are caused by the temporal alterations in the hemodynamics of cortex. The positive outcome of the study also supports the concept of using time dependent diffuse reflectance spectroscopy to detect epileptic cortex intraoperatively.

7. Summary and Future Work

The primary objective of this dissertation is to prove that *fluorescence and diffuse reflectance spectroscopy can detect interictal pathophysiological characteristics associated with pediatric epileptic cortex in an intraoperative environment.* To achieve this goal, three aims were designed and studies were carried out, and they were:

(1) To identify static fluorescence and diffuse reflectance spectral features those differentiate between normal and epileptic pediatric cortex defined by pathology.

(2) To develop a portable fiberoptic spectroscopic system with capability to capture dynamic diffuse reflectance spectra from *in vivo* brain in an intraoperative environment.

(3) To identify dynamic diffuse reflectance spectral features associated with pediatric epileptic cortex defined by ECoG and pathology.

The results of the first study show that static diffuse reflectance spectroscopy and its combination with static fluorescence spectroscopy can be used to effectively differentiate between epileptic cortex (defined by histology) and normal cortex *in vivo* with a high degree of accuracy. The success of this study is attributed to the fact that static hemodynamic characteristics of epileptic cortex, namely hemoglobin concentration and oxygenation, are very different from those of the normal cortex. These findings imply the feasibility of using diffuse reflectance spectroscopy to localize the histopathological abnormalities associated with pediatric epileptic cortex in an intraoperative environment. The same study also shows that fluorescence spectroscopy alone is insufficient in differentiating between epileptic cortex and normal cortex, which is attributed to the modulation of cortical optical properties to the fluorescence signals.

To maximize the efficiency of optical spectroscopy in detecting and localizing epileptic cortex intraoperatively, the static system was upgraded to investigate histopathological abnormalities deep within the epileptic cortex, as well as to detect unique temporal pathophysiological characteristics of epileptic cortex. Detection of deep abnormalities within the epileptic cortex required a redesign of the fiberoptic probe. A simulation model for photon migration was developed to evaluate the correlation among source-detector separation (i.e., design factor), depth of investigation, and signal strength. Based on the insights produced by the simulation model, it was concluded that the optimal source-detection separation is between 0.6 to 1 mm and the illumination wavelength should be beyond 600 nm for deep penetration. To capture time dependent characteristics of epileptic cortex, a dynamic diffuse reflectance spectroscopy system was designed and constructed. The system is capable of continuously recording diffuse reflectance spectra from the *in vivo* brain at a high rate (33 Hz) for at least 12 seconds. The performance of the system was confirmed through the analysis of the signal to noise ratio of the spectrometer and the stability of the excitation light source. A mechanical probe holder was also designed and constructed to maintain the probe contact pressure and contact point during the time dependent measurements. The improvement of the data quality introduced by the probe holder was confirmed using an *in vivo* human study.

In the third study, the dynamic diffuse reflectance spectroscopy system was used to characterize *in vivo* pediatric epileptic cortex. The results of this study shows that some unique wavelength dependent temporal characteristics (e.g., multiple horizontal bands in the correlation coefficient map $\gamma(\lambda_{ref} = 800$ nm, $\lambda_{comp}, t))$ can be found in the time dependent recordings from epileptic cortex defined by ECoG. According to the simulation model, these characteristics are caused by the temporal alterations in the hemodynamics of cortex. The positive outcome of the study also supports the concept of using time dependent diffuse reflectance spectroscopy to detect epileptic cortex intraoperatively.

While the research results disclosed in this dissertation support the central hypothesis of the research project, there are still many improvements that have to be implemented before optical spectroscopy can make a positive impact on future epilepsy surgery. First of all, the analysis of the time dependent recording needs to be enhanced to fully realize the potential of dynamic diffuse reflectance spectroscopy in intraoperative localization and demarcation of epileptic cortex. Secondly, the dynamic fluorescence spectroscopy should be developed and tested because it will assess the dynamic metabolic characteristics of epileptic cortex, which is not achievable using the existing technologies. Thirdly, the *in vivo* data acquisition should be carried using a non-contact means (i.e., remote sensing) to completely eliminate the artifacts induced by inconsistent probe contact pressure as well as brain movement. Finally, the optical recording should be performed simultaneously with the electrical recording (i.e., ECoG) to uncover the correlation between the electrical activities of epileptic cortex with their physiological characteristics.

LIST OF REFERENCES

1. Williams J, Sharp G.B., Epilepsy. In: K.O. Yeates, M.D. Ris and H.G. Taylor, Eds, “Pediatric neuropsychology: Research, theory, and practice”, The Guilford Press, New York 2000:47-73

2. Thompson PJ, Trimble MR: “Neuropsychological aspects of epilepsy in neuropsychological assessment of neuropsychiatric disorders”, in Neuropsychological Assessment of Neuropsychiatric Disorders, 2nd ed. Edited by Grant IG, Adams KM. New York, Oxford University Press, 1996:263-287

3. A.S. Winkler, M. Schaffert, and R. Schmutzhard, “Epilepsy in resource poor countries – suggestion of an adjusted classification,” Epilepsia **48**:1029-1030 (2007)

4. F. Frohlich, M. Bazhenov, V. Iragui-Madoz, and T.J. Sejnowski, “Potassium Dynamics in the Epileptic Cortex - New Insights on an Old Topic,” The Neuroscientist **14**, 422-433 (2008)

5. M. Bazhenov, I. Timofeev, F. Frohlich, and T.J. Sejnowski, “Cellular and network mechanisms of electrographic seizures,” Drug Discovery Today: Disease Models Spring **5,** 45-57 (2008)

6. D. Pare´ and E.J. Lang, “Calcium electrogenesis in neocortical pyramidal neurons in vivo,” Eur. J. Neurosci.**10**, 3164–3170 (1998)

7. N.C. de Lanerolle, T.S. Lee and D.D. Spencer, “Astrocytes and epilepsy,” Neurotherapeutics **7**, 424-38 (2010)

8. Y. Fujiwara-Tsukamoto, Y. Isomura, A. Nambu, and M. Takada, “Excitatory gaba input directly drives seizure-like rhythmic synchronization in mature hippocampal CA1 pyramidal cells,” Neuroscience **119**, 265–275 (2003)

9. William H. Theodore, “Does Serotonin Play a Role in Epilepsy?” Epilepsy Curr **3**, 173–177 (2003)

10. A. Friedman, C.J. Behrens, U. Heinemann, “Cholinergic dysfunction in temporal lobe epilepsy,” Epilepsia **48**,126-30 (2007)

11. Yukitoshi Takahashi, “Infections as causative factors of epilepsy, Future Neurology,” **1,** 291-302 (2006)

12. S.R. Chandana, S. Movva, M. Arora, T. Singh, “Primary brain tumors in adults,” Am Fam Physician **77,** 1423-1430 (2008)

13. E.G. Neal, H. Chaffe, R.H. Schwartz, M.S. Lawson, N. Edwards, G. Fitzsimmons, A. Whitney, J.H. Cross, “The ketogenic diet for the treatment of childhood epilepsy: a randomised controlled trial,” Lancet Neurol **7**, 500–506 (2008)

14. J.M. Freeman, E.H. Kossoff, and A.L. Hartman, “The ketogenic diet: one decade later,” Pediatrics, **119**, 535–43 (2007)

15. S. Thammongkol, D.F. Vears, J. Bicknell-Royle, J. Nation, K. Draffin, K.G. Stewart, I.E. Scheffer, and M.T. Mackay, “Efficacy of the ketogenic diet: which epilepsies respond?,” Epilepsia **5,** e55-9 (2012)

16. W.H. Tresche, “Pediatric Epilepsy: Diagnosis and therapy,” Edited by W. Edwin Dodson and John M. Pellock, New York, Demos, illustrated, Ann Neurol. **34**, 419-*446* (*1993*)

17. Heck, Christi, Sandra L Helmers, and Christopher M DeGiorgio, “Vagus nerve stimulation therapy, epilepsy, and device parameters: scientific basis and recommendations for use,” Neurology **59**, S31-S37(2002)

18. P. Jayakar, “Invasive EEG monitoring in children: when, where, and what?” J Clin Neurophysiol **16**, 408-18 (1999)

19. J.M. Paolicchi, P. Jayakar, P. Dean, I. Yaylali, G. Morrison, A. Prats, T. Resnik, L. Alvarez, and M. Duchowny, “Predictors of outcome in pediatric epilepsy surgery,” Neurology **54,** 642-7 (2000)

20. P. Jayakar, M. Duchowny, and T.J. Resnick, “Subdural monitoring in the evaluation of children for epilepsy surgery” J Child Neurol **9,** 61-6 (1994)

21. P. Jayakar, M. Duchowny, T.J. Resnick, and L.A. Alvarez, “Localization of seizure foci: Pitfalls and caveats,” J Clin Neurophysiol **8,** 414-31(1991)

22. H. Jones, and M. Smith, “Awake craniotomy,” Contin Educ Anaesth Crit Care Pain **14,** 189-92 (2004)

23. P.G. Matz, C. Cobbs, and M.S. Berger, “Intraoperative cortical mapping as a guide to the surgical resection of gliomas,” J Neurooncol. **42,** 233-245 (1999)

24. P.D. Adelson*,* “The surgical management of epilepsy in childhood: A review,” Neurosurg Q **6,** 1–20 (1996)

25. R. Wennberg, F. Quesney, A. Olivier, and T. Rasmussen, “Electrocorticography and outcome in frontal lobe epilepsy,” Electroencephalogr Clin Neurophysiol **106,** 357-68 (1998)

26. P. Jayakar, L.A. Alvarez, M. Duchowny, and T.J. Resnick, “Intraictal activation in the neocortex: A marker of the epileptogenic region,” Epilepsia **35,** 489-94 (1994)

27. P. Jayakar, L.A. Alvarez, M. Duchowny, and T.J. Resnick, "A safe and effective paradigm to functionally map the cortex in childhood," J Clin Neurophysiol **9,** 288-93 (1992)

28. P. Jayakar, "Invasive EEG monitoring in children: when, where, and what?," J Clin Neurophysiol **16,** 408-18 (1999)

29. Raj D. Sheth, "Intractable pediatric epilepsy: Presurgical evaluation," Seminars in pediatric neurology **7,** 158-165 (2000)

30. F.E. Jansen, A.C. van Huffelen, A. Algra, and O. van Nieuwenhuizen, "Epilepsy surgery in tuberous sclerosis: a systematic review," Epilepsia **48,** 1477-1484 (2007)

31. Hema Patel, Bhuwan P. Garg, Omkar N. Markand, "Bathing epilepsy: Video/EEG recording and literature review," Journal of Epilepsy **7,** 290-294 (1994)

32. V. Villanueva, A. Gutiérrez, M. García, A. Beltrán, J. Palau, R. Conde, P. Smeyers, P. Rubio, E. Gómez, T. Rubio, A. Sanjuán, C. Avila, J.C. Martínez, V. Belloch, R. Pérez-Velasco, A. Campo, J. Domínguez, "Usefulness of Video-EEG monitoring in patients with drug-resistant epilepsy," Neurologia **26,** 6-12 (2011)

33. A.T. Berg, F.M. Testa, S.R. Levy, and S. Shinnar, "Neuroimaging in children with newly diagnosed epilepsy: a community-based study," Pediatrics September **106,** 527-32(2000)

34. U.C. Wieshmann, "Clinical application of neuroimaging in epilepsy," J Neurol Neurosurg Psychiatry **74,** 466-70 (2003)

35. Andrea Bernasconi, Neda Bernasconi, Boris C. Bernhardt and Dewi Schrader, "Advances in MRI for 'cryptogenic' epilepsies," Nature Reviews Neurology **7,** 99-108 (2011)

36. T.M. Salmenpera, and J.S. Duncan, "Imaging in epilepsy," J Neurol Neurosurg Psychiatry **76,** iii2-iii10 (2005)

37. B. Alkonyi, H.T. Chugani, and C. Juhász, "Transient focal cortical increase of interictal glucose metabolism in Sturge-Weber syndrome: implications for epileptogenesis," Epilepsia. **52,** 1265-72 (2011)

38. K. Benedek, C. Juhasz, D.C. Chugani, O. Muzik,and H.T. Chugani, "Longitudinal changes in cortical glucose hypometabolism in children with intractable epilepsy*," J* Child Neurol **21,** 26-31 (2006)

39. Ross P. Carne, Terence J. O'Brien, Christine J. Kilpatrick, Lachlan R. MacGregor, Lucas Litewka, Rodney J. Hicks, and Mark J. Cook, "MRI-negative PET-positive temporal lobe

epilepsy (TLE) and mesial TLE differ with quantitative MRI and PET: a case control study," BMC Neurol. **7,** 16 (2007)

40. D.C. Alsop, A. Connelly, J.S. Duncan, A. Hufnagel, C. Pierpaoli, and F.J. Rugg-Gunn, "Diffusion and perfusion MRI in epilepsy," Epilepsia **43,** 69–77 (2002)

41. Baumgartner Christoph, Serles Wolfgang, Leutmezer Fritz, Pataraia Ekaterina, Gudrun Gröppel, Johanna Bacher, Susanne Aull, Wolfgang Serles, Martha Hoffmann, Fritz Leutmezer, Thomas Czech, Daniela Prayer, Uwe Pietrzyk, Susanne Asenbaum, Ivo Podreka, "Preictal SPECT in temporal lobe epilepsy: Regional cerebral blood flow is increased prior to electroencephalography-seizure onset," The Journal of Nuclear Medicine **39,** 978-982 (1998)

42. Mateo Calderon-Arnulphi, Ali Alaraj, Sepideh Amin-Hanjani, William W Mantulin, Chiara M Polzonetti, Enrico Gratton, and Fady T Charbel, "Detection of cerebral ischemia in neurovascular surgery using quantitative frequency-domain near-infrared spectroscopy," Journal of Neurosurgery **106,** 283-90(2007)

43. D. Le Bihan, J.F. Mangin, C. Poupon, C. Clark, S. Pappata, N. Molko, and H. Chabriat, "Diffusion tensor imaging: concepts and applications," J Magn Reson Imag **13,** 534–546 (2001)

44. A. Assaf Bassam, B. Mohamed Feroze, J. Abou-Khaled Karine, Williams J. Michael, S. Yazeji May, Haselgrove John, and H. Faro Scott, "Diffusion tensor imaging of the hippocampal formation in temporal lobe epilepsy," American journal of neuroradiology **24,** 1857-62 (2003)

45. D. Zumsteg, and H.G. Wieser, "Presurgical evaluation: current role of invasive EEG," Epilepsia **41,** S55-S60 (2000)

46. A. Kuruvilla, and R. Flink, "Intraoperative electrocorticography in epilepsy surgery: useful or not?," Seizure 12, 577-584 (2003)

47. S.A. Prahl, "Optical Absorption of Hemoglobin," (1999), http://omlc.ogi.edu/ spectra/hemoglobin/index.html

48. R. M. Doornbos, R. Lang, M. C. Aalders, F. W. Cross, and H. J. Sterenborg, "The determination of in vivo human tissue optical properties and absolute chromophore concentrations using spatially resolved steady-state diffuse reflectance spectroscopy," Phys Med Biol, **44,** 967-81 (1999)

49. A. M. Nilsson, C. Sturesson, D. L. Liu, and S. Andersson-Engels, "Changes in spectral shape of tissue optical properties in conjunction with laser-induced thermotherapy," Appl Opt **37,** 1256-67 (1998)

50. J. Swartling, S. Palsson, P. Platonov, S. B. Olsson, and S. Andersson-Engels, “Changes in tissue optical properties due to radio-frequency ablation of myocardium,” Med. Biol. Eng. Comput. **41,** 403 (2003)

51. W.C. Lin, S. A. Toms, M. Johnson, E. D. Jansen, and A. Mahadevan-Jansen, "In vivo brain tumor demarcation using optical spectroscopy," Photochemistry and Photobiology **73,** 396-402 (2001)

52. F. Bevilacqua, D. Piguet, P. Marquet, J. D. Gross, B. J. Tromberg, and C. Depeursinge, “In vivo local determination of tissue optical properties: applications to human brain,” Applied Optics **38,** 4939-4950 (1999)

53. G. Zonios, J. Bykowski, and N. Kollias, “Skin melanin, hemoglobin, and light scattering properties can be quantitatively assessed in vivo using diffuse reflectance spectroscopy,” J. Invest Dermatol **117,** 1452-1457 (2001)

54. M. G. Muller, T. A. Valdez, I. Georgakoudi, V. Backman, C. Fuentes, S. Kabani, N. Laver, Z. M. Wang, C. W. Boone, R. R. Dasari, S. M. Shapshay, and M. S. Feld, “Spectroscopic detection and evaluation of morphologic and biochemical changes in early human oral carcinoma,” Cancer **97,** 1681-1692 (2003)

55. D. Hidovic-Rowe and E. Claridge, “Modeling and validation of spectral reflectance for the colon,” Physics in Medicine and Biology **50,** 1071-1093 (2005)

56. G. Zonios, L. T. Perelman, V. Backman, R. Manoharan, M. Fitzmaurice, J. V. Dam, and M. S. Feld, "Diffuse reflectance spectroscopy of human adenomatous colon polyps in vivo," Applied Optics **38,** 6628-6637 (1999)

57. S. Srinivasan, B. W. Pogue, S. Jiang, H. Dehghani, C. Kogel, S. Soho, J. J. Gibson, T. D. Tosteson, S. P. Poplack, and K. D. Paulsen, “Interpreting hemoglobin and water concentration, oxygen saturation, and scattering measured in vivo by near-infrared breast tomography,” PNAS **100,** 12349-12354 (2003)

58. N. Shah, A. Cerussi, C. Eker, J. Espinoza, J. Butler, J. Fishkin, R. Hornung, and B. Tromberg, “Noninvasive functional optical spectroscopy of human breast tissue,” PNAS **98,** 4420-4425 (2001)

59. I. Georgakoudi, B. C. Jacobson, J. V. Dam, V. Backman, M. B. Wallace, M. G. Muller, Q. Zhang, K. Badizadegan, D. Sun, G. A. Thomas, L. T. Perelman, and M. S. Feld, “Fluorescence, reflectance, and light-scattering spectroscopy for evaluating dysplasia in patients with Barrett's esophagus,” Gastroenterology **120,** 1620-1629 (2001)

60. W. T. Knoefel, N. Kollias, D. W. Rattner, N. S. Nichioka, and A. L. Warshaw, “Reflectance spectroscopy of pancreatic microcirculation,” Journal of Applied Physiology **80,** 116-123 (1996)

61. R. J. Nordstrom, L. Burke, J. M. Niloff, and J. F. Myrtle, "Identification of cervical intraepithelial neoplasia (CIN) using UV-excited fluorescence and diffuse-reflectance tissue spectroscopy," Lasers in Surgery and Medicine **29,** 118-127 (2001)

62. G. Zonios, L. Perelman, V. Backman, R. Manoharan, M. Fitzmaurice, J. Van Dam, and M. Feld, "Diffuse Reflectance Spectroscopy of Human Adenomatous Colon Polyps In Vivo," Appl. Opt. **38,** 6628-6637 (1999)

63. S. Bradley Robert, and Maureen S. Thorniley, "A review of attenuation correction techniques for tissue fluorescence," Journal of the Royal Society Interface the Royal Society **3,** 1-13 (2006)

64. Avraham Mayevsky, and Gennady G. Rogatsky, "Mitochondrial function in vivo evaluated by NADH fluorescence: from animal models to human studies," American journal of physiology-Cell physiology **292,** C615-40 (2007)

65. J. Wu, Y. Wang, L. Perelman, I. Itzkan, R.R. Dasari and M.S. Feld, "Time-resolved multichannel imaging of fluorescent objects embedded in turbid media," Opt. Lett. **20** 489–91 (1995)

66. Salomatina Elena, Muzikansky Alona, Neel Victor, and N. Yaroslavsky Anna, "Multimodal optical imaging and spectroscopy for the intraoperative mapping of nonmelanoma skin cancer," Journal of Applied Physics **105,** 102010-102010-7 (2009)

67. D.J. Evers, B.H.W. Hendriks, G.W. Lucassen and T.J.M. Ruers, "Optical spectroscopy: current advances and future applications in cancer diagnostics and therapy," **8,** 307-320 (2012)

68. W.C. Lin, S.A. Toms, M. Motamedi, E.D. Jansen, A. Mahadevan-Jansen, "Brain tumor demarcation using optical spectroscopy: an in vitro study," Journal Of Biomedical Optics **5,** 214-20 (2000)

69. W.C. Lin, D.I. Sandberg, S. Bhatia, M. Johnson, S. Oh,and J. Ragheb, "Diffuse reflectance spectroscopy for in vivo pediatric brain tumor detection", Journal of Biomedical Optics **15,** 061709 (2010)

70. S. Bhatia, J.R. Ragheb, M. Johnson, Sanghoon Oh, D.I. Sandberg, and W.C. Lin, "The role of optical spectroscopy in epilepsy surgery in children," Neurosurgery Focus. **25,** E24 (2008)

71. S. Oh, T. Stewart, I. Miller, S. Bhatia, J. Ragheb, M. Duchowny, P. Jayakar P and W.C. Lin, "In vivo optical properties of cortical tubers in children with tuberous sclerosis complex (TSC): a preliminary investigation," Epilepsia. **52,** 1699-1704 (2011)

72. M.M. Haglund, and D.W. Hochman, "Optical imaging of epileptiform activity in human neocortex," Epilepsia. **45,** 43-7 (2004)

73. T.H. Schwartz, “Optical imaging of epileptiform events in visual cortex in response to patterned photic stimulation,” Cereb Cortex **13,** 1287-98 (2003)

74. Avraham Mayevsky, and Britton Chance, “Oxidation-reduction states of NADH in vivo: from animals to clinical use,” Mitochondrion **7,** 330-9 (2007)

75. T.H. Schwartz, “Neurovascular Coupling and Epilepsy: Hemodynamic Markers for Localizing and Predicting Seizure Onset,” Epilepsy Currents **7,** 91–94 (2007)

76. Markus G. Müller, Irene Georgakoudi, Qingguo Zhang, Jun Wu, and Michael S. Feld, “Intrinsic fluorescence spectroscopy in turbid media: disentangling effects of scattering and absorption,” Applied Optics **40,** 4633-4646 (2001)

77. V. Diekmann, W. Becker, R. Jurgens, B. Grozinger, B. Kleiser, H.P. Richter, and K.H. Wollinsky, “Localisation of epileptic foci with electric, magnetic and combined electromagnetic models,” Electroenceph clin Neurophysioly **106,** 297–313 (1998)

78. P. Kwan and M. J. Brodie, "Early identification of refractory epilepsy," N. Engl. J. Med. **342**(5), 314-319 (2000).

79. A. T. Berg, S. Shinnar, S. R. Levy, F. M. Testa, S. Smith-Rapaport, and B. Beckerman, "Early development of intractable epilepsy in children: a prospective study," Neurology **56**(11), 1445-52 (2001).

80. J.H. Cross, P. Jayakar, D. Nordli, O. Delalande, M. Duchowny, H. G. Wieser, R. Guerrini, and G. W. Mathern, "Proposed criteria for referral and evaluation of children for epilepsy surgery: recommendations of the Subcommission for Pediatric Epilepsy Surgery," Epilepsia **47**(6), 952-9 (2006).

81. J. Engel Jr.,"Surgery for seizures," N. Engl. J. Med.**334**(10), 647-652 (1996).

82. A. S. Harvey, J. H. Cross, S. Shinnar, G. W. Mathern, and the Pediatric Epilepsy Surgery Survey Taskforce, "Defining the spectrum of international practice in pediatric epilepsy surgery patients," Epilepsia **49**(1), 146-155 (2008).

83. K. Chapman, E. Wyllie, I. Najm, P. Ruggieri, W. Bingaman, J. Lüders, P. Kotagal, D. Lachhwani, D. Dinner, and H.O. Lüders, "Seizure outcome after epilepsy surgery in patients with normal preoperative MRI," J. Neurol. Neurosurg Psychiatry **76**(5), 710-3 (2005).

84. M. Hemb, T. R. Velasco, M. S. Parnes, J. Y. Wu, J. T. Lerner, J. H. Matsumoto, S. Yudovin, W. D. Shields, R. Sankar, N. Salamon, H. V. Vinters, and G. W. Mathern, "Improved outcomes in pediatric epilepsy surgery: the UCLA experience, 1986-2008," Neurology **74**(22),1768-75 (2010).

85. F. Sperli, L. Spinelli, M. Seeck, M. Kurian, C. M. Michel, and G. Lantz, "EEG source imaging in pediatric epilepsy surgery: a new perspective in presurgical workup," Epilepsia **47**(6) 981-990 (2006).

86. D. W. Roberts, A. Hartov, F. E. Kennedy, M. I. Miga, and K. D. Paulsen, "Intraoperative brain shift and deformation: a quantitative analysis of cortical displacement in 28 cases," Neurosurgery **43**(4), 749-758 (1998)

87. C. Nimsky, O. Ganslandt, P. Hastreiter, and F. Fahlbusch, "Intraoperative compensation for brain shift," Surg. Neurol. **56**(6), 357-364 (2001).

88. C. Nimsky, O. Ganslandt, S. Cerny, P. Hastreiter, G. Greiner, and R. Fahlbusch, "Quantification of, visualization of, and compensation for brain shift using intraoperative magnetic resonance imaging," Neurosurgery **47**(5), 1070-1079 (2000).

89. S. Ding, M. I. Miga, R. C. Thompson, P. Dumpuri, A. Cao, and B. M. Dawant, "Estimation of intra-operative brain shift using a tracked laser range scanner," Conf. Proc. IEEE Eng. Med. Biol. Soc. 848-851 (2007).

90. E. Asano, C. Juhász, A. Shah, S. Sood and H. T. Chugani, "Role of subdural electrocorticography in prediction of long-term seizure outcome in epilepsy surgery," Brain **132**(Pt 4), 1038-1047 (2009).

91. V. Jay and L. E. Becker, "Surgical pathology of epilepsy: a review," Pediatr. Pathol.**14**(4), 731-750 (1994).

92. R. Richards-Kortum and E. Sevick-Muraca, "Quantitative optical spectroscopy for tissue diagnosis," Annu. Rev. Phys. Chem.**47**, 555-606 (1996).

93. K. Sokolov, M. Follen, and R. Richards-Kortum, "Optical spectroscopy for detection of neoplasia," Curr. Opin. Chem. Biol.**6**(5), 651-658 (2002).

94. Z. Huang, A. McWilliams, H. Lui, D. I. McLean, S. Lam, and H. Zeng, "Near-infrared Raman spectroscopy for optical diagnosis of lung cancer," Int. J. Cancer, **107**(6), 1047-1052 (2003).

95. A. Gillenwater, R. Jacob, R. Ganeshappa, B. Kemp, A. K. El-Naggar, J. L. Palmer, G. Clayman, M. F. Mitchell, and R. Richards-Kortum, "Noninvasive diagnosis of oral neoplasia based on fluorescence spectroscopy and native tissue autofluorescence," Arch. Otolaryngol. Head. Neck. Surg. **124**(11), 1251-1258 (1998).

96. J. R. Mourant, I. J. Bigio, J. Boyer, R. L. Conn, T. Johnson, and T. Shimada, "Spectroscopic diagnosis of bladder cancer with elastic light scattering," Lasers Surg. Med. **17**(4), 350-357 (1995).

97. G. M. Palmer, C. F. Zhu, T. M. Breslin, F. S. Xu, K. W. Gilchrist, and N. Ramanujam, "Comparison of multiexcitation fluorescence and diffuse reflectance spectroscopy for the diagnosis of breast cancer," IEEE Trans. Biomed. Eng. **50**(11), 1233-1242 (2003).

98. I. J. Bigio and J. R. Mourant, "Ultraviolet and visible spectroscopies for tissue diagnostics: fluorescence spectroscopy and elastic-scattering spectroscopy," Phys. Med. Biol. **42**(5), 803-814 (1997).

99. G. A.Wagnieres, W. M. Star, and B. C. Wilson, "In vivo fluorescence spectroscopy and imaging for oncological applications," Photochem. Photobiol. **68**(5), 603-632 (1998).

100. D.A. Boas, T. Gaudette, G. Strangman, X. Cheng, J.J. Marota, and J.B. Mandeville, "The accuracy of near infrared spectroscopy and imaging during focal changes in cerebral hemodynamics," Neuroimage **13**(1), 76-90 (2001).

101. A. Villringer, J. Planck, C. Hock, L. Schleinkofer, and U. Dirnagl, "Near infrared spectroscopy (NIRS): a new tool to study hemodynamic changes during activation of brain function in human adults," Neurosci. Lett. **154**(1-2), 101-104 (1993).

102. M. Zhao, M. Suh, H. Ma, C. Perry, A. Geneslaw, and T. H. Schwartz, "Focal increases in perfusion and decreases in hemoglobin oxygenation precede seizure onset in spontaneous human epilepsy," Epilepsia **48**(11), 2059-2067 (2007).

103. M. M. Haglund, "Optical imaging of visual cortex epileptic foci and propagation pathways," Epilepsia **53**(Suppl 1), 87-97 (2012).

104. J. Engel Jr, D. E. Kuhl, M. E. Phelps, and J. C. Mazziotta, "Interictal cerebral glucose metabolism in partial epilepsy and its relation to EEG changes," Ann. Neurol. **12**(6), 510-7 (1982).

105. G. Franck, B. Sadzot, E. Salmon, J. C. Depresseux, T. Grisar, J. M. Peters, M. Guillaume, L. Quaglia, G. Delfiore, and D. Lamotte, "Regional cerebral blood flow and metabolic rates in human focal epilepsy and status epilepticus," Adv. Neurol. **44**, 935-48 (1986).

106. S. K. Kim, D. S. Lee, S. K. Lee, Y. K. Kim, K. W. Kang, C. K. Chung, J. K. Chung, and M.C. Lee, "Diagnostic performance of [18F]FDG-PET and ictal [99mTc] HMPAO SPECT in occipital lobe epilepsy," Epilepsia **42**(12), 1531-40 (2001).

107. D. E. Kuhl, J. Engel Jr, M. E. Phelps, and C. Selin, "Epileptic patterns of local cerebral metabolism and perfusion in humans determined by emission computed tomography of 18FDG and 13NH3," Ann. Neurol. **8**(4) 348-360 (1980).

108. B.I. Lee, O.N. Markand, A.R. Siddiqui, H.M. Park, B. Mock, H.H. Wellman, R.M. Worth, and M.K. Edwards, "Single photon emission computed tomography (SPECT)

brain imaging using N,N,N'-trimethyl-N'-(2 hydroxy-3-methyl-5-123I-iodobenzyl)-1,3-propanediamine 2 HCl (HIPDM): intractable complex partial seizures," Neurology **36**(11), 1471-1477 (1986).

109. B. Stefanovic, J. Warnking, E. Kobayashi and A. P. Bagshaw, "Hemodynamic and metabolic responses to activation, deactivation and epileptic discharges," Neuroimage **28**(1), 205-215 (2005).

110. J. S. Duncan, "Imaging and epilepsy," Brain **120**(Pt 2), 339-377 (1997).

111. W. H. Theodore, R. Brooks, R. Margolin, N. Patronas, S. Sato S, R. J. Porter, L. Mansi, D. Bairamian, and G. DiChiro, "Positron emission tomography in generalized seizures," Neurology **35**(5), 684-690 (1985).

112. L. O. Kapucu, A. Serdaroglu, C. Okuyaz, G. Kose and K. Gucuyener, "Brain single photon emission computed tomographic evaluation of patients with childhood absence epilepsy," J. Child. Neurol. **18**(8), 542-548 (2003).

113. M. C. Prevett, J. S. Duncan, T. Jones, D. R. Fish, and D. J. Brooks, "Demonstration of thalamic activation during typical absence seizures using H2(15)O and PET," Neurology **45**(7), 1396-1402 (1995).

114. G. R. Gordon, S. J. Mulligan, and B. A. MacVicar, "Astrocyte control of the cerebrovasculature," Glia.**55**(12), 1214-1221(2007).

115. G. Balazsi, A. H. Cornell-Bell, and F. Moss, "Increased phase synchronization of spontaneous calcium oscillations in epileptic human versus normal rat astrocyte cultures," Chaos.**13**(2), 515-518 (2003).

116. S. Ding, T. Fellin, Y. Zhu, S. –Y. Lee, Y. P. Auberson, D. F. Meaney, D. A. Coulter, G. Carmignoto, and P. G. Haydon, "Enhanced astrocytic Ca2+ signals contribute to neuronal excitotoxicity after status epilepticus," J. Neurosci. **27**(40), 10674-10684(2007).

117. H. Hirase, L. Qian, P. Barthó, and G. Buzsáki, "Calcium dynamics of cortical astrocytic networks in vivo," PLoS Biol. **2**(4), E96 (2004).

118. A. Tashiro, J. Goldberg, and R. Yuste, "Calcium oscillations in neocortical astrocytes under epileptiform conditions," J. Neurobiol. **50**(1), 45-55 (2002).

119. A.G. Mignani and F. Baldini, "Biomedical sensors using optical fibers," Rep. Prog. Phys., **59,** 1-28 (1996)

120. Anil Kishen, Annie Shrestha, and Adeela Rafique, “Fiber optic backscatter spectroscopic sensor to monitor enamel demineralization and remineralization in vitro,” World J Clin Oncol. **2**, 50-63 (2008)

121. L.H. Wang, S.L. Jacques, and L.Q Zheng, "MCML - Monte Carlo modeling of photon transport in multi-layered tissues," Computer Methods and Programs in Biomedicine **47,** 131-146 (1995)

122. A. Wang, J. Bender, U. Utzinger, and R. Drezek, "Depth sensitive reflectance measurements using obliquely oriented fiber probes," J. Biomed. Opt. **10,** 044017 (2005)

123. J. Pfefer, A. Agrawal, and R. Drezek, "Oblique-incidence illumination and collection for depth-selective fluorescence spectroscopy," J. Biomed. Opt. **10,** 044016 (2005)

124. Florian E. W. Schmidt, "Development of a Time-Resolved Optical Tomography System for Neonatal Brain Imaging," PhD Thesis, University College London, (1999)

125. C. Von Economo, G.N. Koskinas, Basel: Karger, "Atlas of the cytoarchitectonics of the adult human cerebral cortex (translated, revised and edited by L. C. Triarhou)," (2008)

126. S. Gebhart, W.C. Lin, A. Mahadevan-Jansen, "Normal and neoplastic brain tissue optical properties using inverse adding-doubling," Physics in Medicine and Biology 21; **51,** 2011-27 (2006)

127. P. van der Zee, M. Essenpreis, and D. T. Delpy, "Optical properties of brain tissue," Photon Migration and Imaging in Random Media and Tissues, R. R. Alfano and B. Chance, eds., Proc. SPIE 1888, 454-465 (1993)

128. A. N. Yaroslavsky, P. C. Schulze, I. V. Yaroslavsky, R. Schober, F. Ulrich and H.J. Schwarzmaier, "Optical properties of selected native and coagulated human brain tissues in vitro in the visible and near infrared spectral range," Physics In Medicine and Biology **47,** 2059-2073 (2002)

129. B. Fischl, and A.M. Dale, "Measuring the thickness of the human cerebral cortex from magnetic resonance images," Proc Natl Acad Sci USA **97,** 11050-11055 (2000)

130. Bigio, I. and S. Bown, Spectroscopic sensing of cancer and cancer therapy: current status of translational research. Cancer Biol Ther, 2004. **3**(3): p. 259-267.

131. Brown, J.Q., et al., Advances in quantitative UV-visible spectroscopy for clinical and pre-clinical application in cancer. Curr Opin Biotechnol, 2009. **20**(1): p. 119-31.

132. Perelman, L.T., Optical diagnostic technology based on light scattering spectroscopy for early cancer detection. Expert Rev Med Devices, 2006. **3**(6): p. 787-803.

133. Bakker Schut, T.C., et al., In vivo detection of dysplastic tissue by Raman spectroscopy. Anal Chem, 2000. **72**(24): p. 6010-8.

134. Wang, T.D. and J. Van Dam, Optical biopsy: a new frontier in endoscopic detection and diagnosis. Clin Gastroenterol Hepatol, 2004. **2**(9): p. 744-53.

135. Haglund, M.M., M.S. Berger, and D.W. Hochman, Enhanced optical imaging of human gliomas and tumor margins. Neurosurgery, 1996. **38**(2): p. 308-17.

136. Sun, Y., et al., Fluorescence lifetime imaging microscopy for brain tumor image-guided surgery. J Biomed Opt, 2010. **15**(5): p. 056022.

137. Mayevsky, A. and G. Rogatsky, Mitochondrial Function In Vivo Evaluated by NADH Fluorescence: From Animal Models to Human Studies. Am J Physiol Cell Physiol, 2006.

138. Benaron, D.A., et al., Continuous, noninvasive, and localized microvascular tissue oximetry using visible light spectroscopy. Anesthesiology, 2004. **100**(6): p. 1469-75.

139. Knotzer, H. and W.R. Hasibeder, Microcirculatory function monitoring at the bedside--a view from the intensive care. Physiol Meas, 2007. **28**(9): p. R65-86.

140. Mallia, R., et al., Oxygenated hemoglobin diffuse reflectance ratio for in vivo detection of oral pre-cancer. J Biomed Opt, 2008. **13**(4): p. 041306.

141. Wang, H.W., et al., Diffuse reflectance spectroscopy detects increased hemoglobin concentration and decreased oxygenation during colon carcinogenesis from normal to malignant tumors. Opt Express, 2009. **17**(4): p. 2805-17.

142. Ti, Y. and W.C. Lin, Effects of probe contact pressure on in vivo optical spectroscopy. Opt Express, 2008. **16**(6): p. 4250-62.

143. Nath A, Rivoire K, Chang S, Cox D, Atkinson EN, Follen M, Richards-Kortum R. Effect of Probe Pressure on Cervical Fluorescence Spectroscopy Measurements. J Biomed Opt 2004;9(3):523-33.

144. K Rivoire, A Nath, D Cox, EN Atkinson, R Richards-Kortum, M Follen. The Effects of Repeated Spectroscopic Pressure Measurements on Fluorescence Intensity in the Cervix. Am J Obstet Gynecol 2004;191(5):1606-17.

145. Shim MG, Song LM, Marcon NE, Wilson BC. In vivo near-infrared Raman spectroscopy: demonstration of feasibility during clinical gastrointestinal endoscopy. Photochem Photobiol 2000;72(1):146-50.

146. H Shangguan, SA Prahl, SL Jacques, LW Casperson. Pressure effects on soft tissues monitored by changes in tissue optical properties. Proc. SPIE. Laser-Tissue Interaction IX, 1998;3254:366-371.

147. Chan EK, Sorg B, Protsenko D, O'Neil M, Motamedi M, Welch AJ. Effects of compression on soft tissue optical properties. IEEE J Quantum Electron. 1996;2(4):943-950.

148. Wenliang Chen, Rong Liu, Kexin Xu, Ruikang K Wang. Influence of contact state on NIR diffuse reflectance spectroscopy in vivo. J. Phys. D: Appl. Phys. 2005;38:2691-2695.

149. Reif R, Amorosino MS, Calabro KW, A'Amar O, Singh SK, and Bigio IJ. Analysis of changes in reflectance measurements on biological tissues subjected to different probe pressures. J Biomed Opt 2008;13(1):010502.

150. L Lim, N Rajaram, B Nichols, JW Tunnell. Time Resolved Study of Probe Pressure Effects on Skin Fluorescence and Reflectance Spectroscopy Measurements. Biomedical Optics OSA Technical Digest (CD). 2010;BTuD102.

151. Sarah Ruderman, Andrew J Gomes, Valentina Stoyneva, Jeremy D Rogers, Angela J Fought, Borko D Jovanovic, Vadim Backman. Analysis of pressure, angle and temporal effects on tissue optical properties from polarization-gated spectroscopic probe measurements. Biomed Opt Express. 2010;1(2):489-499.

152. I. M. Greenberg. Self-retaining retractor and handrest system for neurosurgery.Neurosurgery 1981;8(2):205-208.

153. J. W. Harding, I. N. Sneddon. Proc. Cambridge Philos. Soc. 1945;41:16.

154. Michael A. Green, Lynne E. Bilston, Ralph Sinkus. In vivo brain viscoelastic properties measured by magnetic resonance elastography. NMR in Biomedicine. 2008;21(7):755–764.

155. S. Coyle, C. Markham, W. Lanigan, T. Ward. A Mechanical Mounting System for Functional Near-Infrared Spectroscopy. Brain Imaging Studies Opto-Ireland 2005: Optical Sensing and Spectroscopy.

156. V. Chang, D. Merisier, B. Yu, D. Walmer, N. Ramanujam. Towards a field-compatible optical spectroscopic device for cervical cancer screening in resource-limited settings: effects of calibration and pressure. Optics Express 2011;19:17908-17924.

157. H. Stefan, L.F. Quesney, B. Abou-Khalil, and A. Olivier, "Electrocorticography in temporal lobe epilepsy surgery," Acta Neurol Scand **83,** 65–72 (1991)

158. D.P. Sarco, J.F. Burke, and J.R. Madsen, "Electroencephalography in epilepsy surgery planning," Childs Nerv Syst. **22,** 760-5 (2006)

159. C. Juhász, D.C. Chugani, O. Muzik, C. Watson, J. Shah, A. Shah, and H.T. Chugani, "Is epileptogenic cortex truly hypometabolic on interictal positron emission tomography?," Ann Neurol. **48,** 88–96 (2000)

160. H.T. Chugani, P.J. Rintahaka, and D.A. Shewmon, "Ictal patterns of cerebral glucose utilization in children with epilepsy," Epilepsia. **35**, 813-22 (1994)

161. Astrid Nehlig, "Cerebral metabolic and hemodynamic responses to epilepsy: insights

from animal models," Future Neurology **1,** 787-797 (2006)

162. T. Huppert, S. Diamond, M. Franceschini, and D. Boas, "HomER: a review of time-series analysis methods for near-infrared spectroscopy of the brain," Appl. Opt. **48,** D280-D298 (2009)

VITA

NITIN YADAV

	Born, Alwar, India
2002	Bachelor of Engineering in Instrumentation Engineering Sant Longowal Institute of Engineering & Technology India
2004	Master of Technology in Biomedical Engineering Indian Institute of Technology, Bombay India
2006-2011	Graduate Assistant, Research Assistant Department of Biomedical Engineering Florida International University Miami, Florida
2011-2012	Dissertation Year Fellow University Graduate School Florida International University Miami, Florida

PUBLICATIONS

Nitin Yadav, Adrian Romero, Yinchen Song, Sanghoon Oh, John Ragheb, Sanjiv Bhatia, Wei-Chiang Lin, “Improving the quality of time-dependent, diffuse reflectance spectroscopic signals measured from in vivo brain during craniotomy”, Revision Medical Engineering and Physics, Apr. 2012

Nitin Yadav, Sanjiv Bhatia, John Ragheb, Rupal Mehta, Prasanna Jayakar, William Yong, Wei-Chiang Lin, “In Vivo Detection of Epileptic Brain Tissue Using Static Fluorescence and Diffuse Reflectance Spectroscopy*”,* Revision Journal of Biomedical Optics, Aug. 2012

B. Zhu, N. Yadav, N. Patel, G. Rey, A. Godavarty, “Diffuse optical imaging of brain activation to joint attention experience,” Neuroscience, Apr 2009

Nitin Yadav, Sanghoon Oh, Sanjiv Bhatia, Prasanna Jayakar, John Ragheb, Michael Duchowny, Wei-Chiang Lin, "In vivo characterization of epileptic tissue with time-dependent, diffuse reflectance spectroscopy", The 26th Southern Biomedical Conference, April 30-May 2 2010, College Park, MD

Romani Patel, Nitin Yadav, Dwayne McDaniel, David Roelant, "Gas Retention and Release Test for Low Yield Stress Non-Newtonian Fluids "Waste Management Symposia, February 26-March 3, 2011, Phoenix, Arizona

R. Patel, N. Yadav, G. Tachiev, D. McDaniel, D. Roelant, "Gas Retention and Release Tests for Low Yield Stress Non-Newtonian Fluids", Environmental Management Waste Processing Technical Exchange, November 16 - 18, 2010 Atlanta, Georgia

Romani Patel, Georgio Tachiev, Vishwani Sharma, Nitin Yadav, Dwayne McDaniel, David Roelant, "Gas Retention and Release Experiments with Low Yield Stress Fluids" Waste Management Symposia, March 7-11, 2010 , Phoenix, Arizona

Nitin Yadav, Banghe Zhu, Anuradha Godavarty, Gustavo Rey, "Joint-Attention Related Imaging Studies using Optical Techniques", Marino Autism Research Institute Scientific Symposium, April 22, 2008, Vanderbuilt University, Nashville, Tennessee

Nitin Yadav, Banghe Zhu, Nirav Patel, Gustavo Rey, Anuradha Godavarty, "Joint attention studies using Near Infrared Optical Imaging", Biomedical Optics, March 16-19, 2008, OSA, St. Petersburg, Florida

Banghe Zhu, Nitin Yadav, Nirav Patel, and A. Godavarty, "Functional brain mapping of joint attention skills using diffuse optical imaging", Biomedical Engineering Recent Development, Eds: H. Nazeran, M. Goldman, R. Schoephoerster, 2008 Medical and Engineering Publishers, Inc. 2008

Mita Bhowmick, Nitin Yadav, M.P. Thaddeus, Gargi Vishnoi, "Near-Infrared Light Propagation in Scattering Tissue", CIEE-2005- National Conference on Computational Intelligence in Electrical Engineering, 18-19 Nov, 2005, Sant Longowal Institute of Engg. & Tech. (SLIET), Sangrur, Punjab, India

Mita Bhowmick, Nitin Yadav, M.P. Thaddeus, Gargi Vishnoi, "Numerical Modeling of Near-Infrared Light Propagation in Neonatal Head", NCBME-2004- National conference on biomedical Engineering, 23-24 Dec, 2004, GITAM, Visakhapatnam, Andhra Pradesh, India

Mita Bhowmick, Nitin Yadav, Gargi Vishnoi, "Numerical Modeling of Near-Infrared Light Propagation in Tissue", Photonics-2004- Seventh International Conference on Optoelectronics, Fiber Optics and Photonics, 9-11 Dec, 2004, Cochin, Kerela, India